# MANY-BODY AND SPIN-ORBIT ASPECTS OF THE ALTERNATING CURRENT PHENOMENA

by

Rachel M. Glenn

A dissertation submitted to the faculty of
The University of Utah
in partial fulfillment of the requirements for the degree of

Doctor of Philosophy

in

Physics

Department of Physics and Astronomy

The University of Utah

August 2012

The University of Utah Graduate School

# STATEMENT OF THESIS APPROVAL

The dissertation of Rachel M. Glenn
has been approved by the following supervisory committee members:

| | |
|---|---|
| Mikhail Raikh , Chair | May 4, 2012 |
| | Date Approved |
| Oleg Starykh , Member | May 4, 2012 |
| | Date Approved |
| Christoph Boehme , Member | May 4, 2012 |
| | Date Approved |
| Kyle Dawson , Member | May 4, 2012 |
| | Date Approved |
| Elena Cherkaev , Member | May 4, 2012 |
| | Date Approved |

and by David Kieda , Chair of
the Department of Physics and Astromony

and by Charles A. Wight, Dean of The Graduate School.

# ABSTRACT

The thesis reports on research in the general field of light interaction with matter. According to the topics addressed, it can be naturally divided into two parts: Part I, many-body aspects of the Rabi oscillations which a two-level systems undergoes under a strong resonant drive; and Part II, absorption of the ac field between the spectrum branches of two-dimensional fermions that are split by the combined action of Zeeman and spin-orbit (SO) fields.

The focus of Part I is the following many-body effects that modify the conventional Rabi oscillations: Chapter 1, coupling of a two-level system to a single vibrational mode of the environment. Chapter 2, correlated Rabi oscillations in two electron-hole systems coupled by tunneling with strong electron-hole attraction. In Chapter 1, a new effect of Rabi-vibronic resonance is uncovered. If the frequency of the Rabi oscillations, $\Omega_R$, is close to the frequency, $\omega_0$, of the vibrational mode, the oscillations acquire a collective character. It is demonstrated that the actual frequency of the collective oscillations exhibits a bistable behavior as a function of $\Omega_R - \omega_0$. The main finding in Chapter 2 is, that the Fourier spectrum of the Rabi oscillations in two coupled electron-hole systems undergoes a strong transformation with increasing $\Omega_R$. For $\Omega_R$ smaller than the tunneling frequency, the spectrum is dominated by a low-frequency ($<< \Omega_R$ ) component and contains two additional weaker lines; conventional Rabi oscillations are restored only as $\Omega_R$ exceeds the electron-hole attraction strength.

The highlight of Part II is a finding that, while the spectrum of absorption between either Zeeman-split branches or SO-split branches is close to a $\delta$-peak, in the presence of both, it transforms into a broad line with singular behavior at the edges. In particular, when the magnitudes of Zeeman and SO are equal, absorption of very low (much smaller than the splitting) frequencies become possible. The shape of the absorption spectrum is highly anisotropic with respect to the exciting field. This peculiar behavior of the absorption is also studied in wire geometry, where the interplay between two couplings (Zeeman and spin-orbit splitting) affects the shape of numerous absorption peaks.

I would like to dedicate this thesis to my husband, Ronald Glenn. Through his professorial demeanor I was able to achieve my goals. It is also dedicated to my mother, who taught me good study habits at an early age.

# CONTENTS

# LIST OF FIGURES

# ACKNOWLEDGMENTS

I would like to express my deepest gratitude to my advisor, Dr. Raikh, for providing a welcoming atmosphere for studying physics. Dr. Raikh, with patience, gave me guidance and insight into theoretical physics. In the future, I hope to make Dr. Raikh proud of his invested time.

I thank the members of my graduate committee for their guidance, Dr. Starykh especially, for introducing me to spin liquids and providing financial assistance. I also thank Dr. Boehme for discussions which initiated part of the study in this thesis. I thank Dr. Dawson for his inquisitive nature that drove me to study harder and more in depth. I am very proud to have Dr. Cherkaev on my committee because the thesis involves challenging mathematical integrals.

I would also like to thank a good friend, Jade, who taught me to believe in myself and helped me to believe that I deserve victory.

Finally, I would like to thank my husband, Ronnie, and his son Jordyn. It was through Ronnie's professorial demeanor that I was able to achieve my Phd and Jordyn is light and cheerful personality helped to keep me motivated.

# PART I

# MANY-BODY ASPECTS OF RABI OSCILLATIONS

## 1.1 Preface

In a seminal paper, Ref. [1], in 1937 I. Rabi pointed out that the level population of an ac-driven two-level system oscillates with frequency, $\Omega_R$, proportional to the amplitude of the driving field. As a two-level system, Rabi chose Zeeman split levels and an ac magnetic field as the ac driving force. In notations more common in optics, his finding can be recapped as follows. Suppose the system of two levels with spatial wave functions $\psi_1$ and $\psi_2$ is illuminated by light with amplitude of electric field, $F$, and frequency $\omega_L$ close to the energy difference between the levels. Neglecting all other levels and spontaneous emission, we can describe the evolution of the system within the time-dependent Schrödinger equation,

$$i\frac{\partial \Psi}{\partial t} = \hat{H}\Psi + \frac{eFx}{2}\left(e^{i\omega_L t} + e^{-i\omega_L t}\right)\Psi. \tag{1.1}$$

The essence of the Rabi paper is that for weak-enough driving, the evolution of the level occupations proceeds with frequency much smaller than the frequency of the light. Formally, under this condition, the solution of the Schrödinger equation can be simplified as follows. The wavefunction, $\Psi(t)$ can be presented as a sum of a product of slow and fast oscillating functions, which reads

$$\Psi = a_1(t)\exp\left[-iE_1 t\right]\psi_1(x) + a_2(t)\exp\left[-iE_2 t\right]\psi_2(x). \tag{1.2}$$

Upon substituting this form into the Schrödinger equation, we neglect the fast terms coming either from $e^{i\omega_L t}$ or $e^{-i\omega_L t}$ and get two coupled equations

$$i\frac{\partial a_1}{\partial t} = \Omega_R a_2 e^{-i\Delta t}, \tag{1.3}$$

$$i\frac{\partial a_2}{\partial t} = \Omega_R a_1 e^{i\Delta t}, \tag{1.4}$$

where $\Delta = E_2 - E_1 - \omega_L$. The two coupled Eqs. (1.3) and (1.4) can be reduced to a single equation describing the slow amplitude, say $a_1$, by first differentiating Eq. (1.3) and substituting $\partial a_2/\partial t$ and $a_2$, which gives

$$\frac{\partial^2 a_1}{\partial t^2} + i\Delta\frac{\partial a_1}{\partial t} + \Omega_R^2 a_1 = 0. \tag{1.5}$$

Solution to the second order linear differential equation for $a_1$, Eq. (1.5), can easily be found. We present the solution in the form of the population, which reads

$$|a_1(t)|^2 = 1 - \frac{4\Omega_R^2}{4\Omega_R^2 + \Delta^2}\sin^2\left(\frac{1}{2}\sqrt{4\Omega_R^2 + \Delta^2}t\right). \tag{1.6}$$

The characteristic time scale in this system is the inverse dipole energy. In other words, the inverse Rabi frequency. Then the justification of the approximation made, which is

separation into the slow and fast parts or, in other words, the rotating wave approximation (RWA), is that the Rabi frequency is much smaller than the frequency of light. If this condition is met, we easily find that if the level was occupied at time $t = 0$, then, under perfect resonance, its population oscillates as $\cos^2 \Omega_R t$. Away from resonance, the frequency of oscillations is higher, but the amplitude is smaller.

Now we have to include the spontaneous emission, resulting from interaction of electron with zero-point motion of a vacuum. The way to do it was paved by Felix Bloch, 9 years after Rabi. Using the optical language, to account for spontaneous emission we rewrite the system for amplitudes $a_1$ and $a_2$ as a system for $|a_1|^2$, $|a_2|^2$, $a_1 a_2^*$ and $a_1^* a_2$. In the density matrix language they are called $\rho_{11}$, $\rho_{22}$, $\rho_{12}$, $\rho_{21}$, respectively. Then the density matrix equations read

$$\frac{\partial \rho_{11}}{\partial t} = -i\frac{\Omega_R}{2}(\rho_{21} - \rho_{12}) + \Gamma \rho_{22}, \tag{1.7}$$

$$\frac{\partial \rho_{22}}{\partial t} = -i\frac{\Omega_R}{2}(\rho_{12} - \rho_{21}) - \Gamma \rho_{22}, \tag{1.8}$$

$$\frac{\partial \rho_{12}}{\partial t} = i\Delta \rho_{12} + i\frac{\Omega_R}{2}(\rho_{11} - \rho_{22}) - \frac{\Gamma}{2}\rho_{12}, \tag{1.9}$$

$$\frac{\partial \rho_{21}}{\partial t} = -i\Delta \rho_{21} - i\frac{\Omega_R}{2}(\rho_{11} - \rho_{22}) - \frac{\Gamma}{2}\rho_{21}. \tag{1.10}$$

Note that the spontaneous emission is incorporated via the last terms in the four equations. We see that the population of the upper state is decreased due to spontaneous emission, while the population of the lower state is increased. Adding the two, we confirm that the sum of the populations is zero, meaning the total probability is constant. Less trivial is to comment why the nondiagonal elements of the density matrix decay with the rate $\Gamma/2$, rather than $\Gamma$. In some way, spontaneous emission is similar to friction. Solving Eqs. (1.7)-(1.10), in small parameter $\Gamma$ for $\rho_{11}$, we find

$$\rho_{11}(t) = \frac{\Omega_R^2 + \Gamma^2}{2\Omega_R^2 + \Gamma^2} + \frac{\Omega_R^2 \exp\left(-\frac{3\Gamma}{4}t\right)\cos(\Omega_R t)}{2\Omega_R^2 + \Gamma^2}, \tag{1.11}$$

that the Rabi oscillations always decay with spontaneous emission, despite the fact that the two-level system is constantly driven; whereas, a harmonic oscillator with friction will maintain oscillations, if it is under stationary driving. To observe Rabi oscillations, the driving should be strong enough so that $\Omega_R$ exceeds $\Gamma$.

From Eqs. (1.7)-(1.10), we also see that the energy levels of the two-level system enter only into the equations for nondiagonal matrix elements. This fact explains how the environment affects the Rabi oscillations via the mechanism additional to the spontaneous

emission. Namely, the environment can be viewed as objects which switch at random moments from "up" to "down" states in the course of their *thermal* motion, resulting in time-dependent shifts of the energy levels of the two-level system. These time-dependent shifts cause the damping of the Rabi oscillations after the characteristic time usually denoted with $T_2$.

By now Rabi oscillations were observed experimentally for a very wide variety of systems and in frequency ranges from optics $\omega_L \sim 1.0$ eV to nuclear $\omega_L \sim 0.1$meV. Obviously, in optical experiments, the RWA approximation is perfectly applicable, since the ratio $\Omega_R/\omega_L$ is very small $\sim 10^{-5}$. However, in magnetic-resonance experiments, this ratio equals $B_1/B_0$, where $B_0$ is the dc and $B_1$ is the ac magnetic field, and can be much larger. For this reason, in the remainder of this Preface, we analyze quantitatively the accuracy of the RWA, i.e., the effect of finite ratio $\Omega_R/\omega_L$ on the Rabi oscillations.

We start from the Schrödinger equation, Eq. (1.1), and substitute $\Psi(\mathbf{r},t) = a_1(t)\psi_1(\mathbf{r}) + a_2(t)\psi_2(\mathbf{r})$, then multiplying by $\psi_1^*$ ($\psi_2^*$) and integrating over the spatial coordinates, we get two coupled equations for $a_1$ and $a_2$, which read

$$i\frac{\partial a_1}{\partial t} = E_1 a_1 + \Omega_R a_2\Big(e^{i\omega_L t} + e^{-i\omega_L t}\Big), \tag{1.12}$$

$$i\frac{\partial a_2}{\partial t} = E_2 a_2 + \Omega_R a_1\Big(e^{i\omega_L t} + e^{-i\omega_L t}\Big). \tag{1.13}$$

The Bloch theorem dictates the following general form of the solution of the above system

$$\begin{aligned} a_1 &= e^{-is_1 t}\sum_p C_p \exp(-2ip\omega_L t), \\ a_2 &= e^{-is_2 t}\sum_n D_n \exp(-2in\omega_L t), \end{aligned} \tag{1.14}$$

where the parameters $s_1$ and $s_2$ are related as

$$s_2 - s_1 = \omega_L. \tag{1.15}$$

Substituting Eqs. (1.14) into the system Eqs. (1.12) and (1.13) and equating the like terms yields the following infinite system of linear equations

$$\begin{aligned} (s_1 + 2p\omega_L - E_1)C_p &= \Omega_R\big(D_n + D_{n+1}\big), \\ \big(s_2 + 2n\omega_L - E_2\big)D_n &= \Omega_R\big(C_p + C_{p-1}\big). \end{aligned} \tag{1.16}$$

Consider the terms with $p = n = 0$ in Eq. (1.16), which read

$$(s_1 - E_1)C_0 = \Omega_R(D_0 + D_1),$$

$$(s_2 - E_2)D_0 = \Omega_R(C_0 + C_{-1}). \tag{1.17}$$

Keeping only the terms $D_0$ and $C_0$ immediately leads to the characteristic equation

$$(s_1 - E_1)(s_2 - E_2) = \Omega_R^2, \tag{1.18}$$

which is the standard Rabi result. Neglecting $D_1$ and $C_{-1}$ corresponds to RWA. To study the consequences of going beyond the RWA, we keep these terms, but neglect all other $C_p$ and $D_n$. This results in the system which consists of Eqs. (1.17) plus two more equations

$$\big(s_1 - 2\omega_L - E_1\big)C_{-1} = \Omega_R D_0, \tag{1.19}$$

$$\big(s_2 + 2\omega_L - E_2\big)D_1 = \Omega_R C_0. \tag{1.20}$$

Expressing $C_{-1}$ and $D_1$ from these two equations and substituting into Eqs. (1.17), we arrive at the modified characteristic equation

$$\left[s_1 - E_1 - \frac{\Omega_R^2}{s_2 + 2\omega_L - E_2}\right]\left[s_2 - E_2 - \frac{\Omega_R^2}{s_1 - 2\omega_L - E_1}\right] = \Omega_R^2. \tag{1.21}$$

The basic condition $\Omega_R \ll \omega_L$ allows one to replace $s_2$ in the denominator of the first bracket in Eq. (1.21) by $E_1$ and $s_1$ in the denominator of the second bracket in Eq. (1.21) by $E_2$. After that, the second terms in the brackets coming from corrections to RWA can be simply viewed as shifts of the bare energy-level positions: $E_2 \to E_2 - \frac{\Omega_R^2}{2\omega_L}$, $E_1 \to E_1 + \frac{\Omega_R^2}{2\omega_L}$. Overall, going beyond the RWA leads to the driving induced renormalization of the bare level separation $E_2 - E_1$ by a small amount $\frac{\Omega_R^2}{\omega_L}$ without changing the Rabi frequency. This result was obtained by a different method in a seminal paper [3] by F. Bloch and Siegert.

Another important consequence of a finite ratio $\Omega_R/\omega_L$ is the existence of the *multiphoton* resonances. Their existence was uncovered much later than the conventional Rabi oscillations [4]. It turns out that when the two-level system is illuminated by light with frequency $\omega_L \approx (E_2 - E_1)/(2p+1)$, where $p$ is an integer, the populations of levels also undergo periodic oscillations with much smaller frequency $\sim \Omega_R^p/\omega_L^{(p-1)}$. Below we illustrate this phenomenon for the example of 3-photon oscillations corresponding to $p = 1$.

It is convenient to rescale the energy levels from midway of the difference $E_2 - E_1 = E$. Then $E_1 \to -\frac{E}{2}$ and $E_2 \to \frac{E}{2}$. Adding and subtracting Eqs. (1.12) and (1.13) we get

$$i\frac{\partial}{\partial t}(a_1 + a_2) = \frac{E}{2}(a_1 - a_2) + \Omega_R(a_1 + a_2)f(t), \tag{1.22}$$

$$i\frac{\partial}{\partial t}(a_1 - a_2) = \frac{E}{2}(a_1 + a_2) - \Omega_R(a_1 - a_2)f(t), \tag{1.23}$$

where $f(t) = e^{i\omega_L t} + e^{-i\omega_L t}$. The coupled equations, Eqs. (1.22) and (1.23), and be cast in the form of a single second-order equation by first solving for $(a_1 - a_2)$ from Eq. (1.23) and then substituting it into Eq. (1.22). We get

$$\frac{\partial^2\Psi}{\partial t^2} + \left[i\Omega_R\frac{\partial f(t)}{\partial t} + \frac{E^2}{4} + \Omega_R^2 f^2(t)\right]\Psi = 0, \tag{1.24}$$

where $\Psi = a_1 + a_2$. Again, the Bloch theorem dictates a solution of the form Eq. (1.14). For the 3-photon resonance, $s$ is close to $\frac{1}{2}E$, while $E$ is close to $3\omega_L$. This suggests that, instead of the terms $\propto \exp(ist)$ and $\propto \exp[i(s-\omega_L)t]$ for conventional Rabi oscillations, the "resonating" terms for 3-photon Rabi oscillations are $\propto \exp(ist)$ and $\propto \exp[i(s-3\omega_L)t]$. To provide the "minimal" (in terms of powers of $\Omega_R$) coupling of these terms one has to keep two nonresonant terms, namely $\propto \exp[i(s-\omega_L)t]$ and $\propto \exp[i(s-2\omega_L)t]$. Thus we search for $\Psi(t)$ in the form

$$\Psi(t) = ae^{ist} + be^{i(s-\omega_L)t} + ce^{i(s-2\omega_L)t} + de^{i(s-3\omega_L)t}. \tag{1.25}$$

Inserting Eq. (1.25) into Eq. (1.24) and equating like-terms gives

$$\left[\frac{E^2}{4} + 2\Omega_R^2 - s^2\right]a - \omega_L\Omega_R b + \Omega_R^2 c = 0, \tag{1.26}$$

$$\left[\frac{E^2}{4} + 2\Omega_R^2 - (s-3\omega_L)^2\right]d + \omega_l\Omega_R c + \Omega_R^2 b = 0, \tag{1.27}$$

$$\left[\frac{E^2}{4} + 2\Omega_R^2 - (s-2\omega_L)^2\right]c + \omega_L\Omega_R(b-d) + \Omega_R^2 a = 0, \tag{1.28}$$

$$\left[\frac{E^2}{4} + 2\Omega_R^2 - (s-\omega_L)^2\right]b + \omega_L\Omega_R(a-c) + \Omega_R^2 d = 0. \tag{1.29}$$

Expressing $b$ and $c$ from Eqs. (1.28), (1.29), and substituting them into Eqs. (1.26) and (1.27), we get the following two coupled equations relating $a$ and $d$

$$\left[\frac{E^2}{4} + \frac{5}{2}\Omega_R^2 - \frac{9}{4}\omega_L^2 - 3\omega_L s_1\right]a = -\frac{3}{4}\frac{\Omega_R^3}{\omega_L}d, \tag{1.30}$$

$$\left[\frac{E^2}{4} + \frac{5}{2}\Omega_R^2 - \frac{9}{4}\omega_L^2 + 3\omega_L s_1\right]d = \frac{3}{4}\frac{\Omega_R^3}{\omega_L}a, \tag{1.31}$$

where we introduced $s_1 = \frac{3}{2}\omega_L - s$ and used the fact that $s_1 \ll \omega_L$. The system Eqs. (1.30), (1.31) readily yields

$$s_1^2 = \frac{1}{16}\frac{\Omega_R^6}{\omega_L^4} + \frac{1}{\omega_L^2}\left(\frac{E^2}{4} - \frac{9\omega_L^2}{4} + \frac{5}{2}\Omega_R^2\right)^2. \tag{1.32}$$

Note that this expression has the conventional Rabi form with effective Rabi frequency equal to $\Omega_R^3/4\omega_L^2$ and Bloch-Siegert shift to equal to $5\Omega_R^2/6\omega_L$ instead of $\Omega_R^2\omega_L$ for conventional Rabi oscillations.

Another interesting aspect of the Rabi oscillations pertains to their experimental observation in the situation when they are induced in a *macroscopic* sample, which can be viewed as an ensemble of two-level systems. Each two-level system has its own individual environment. For example, each Zeeman-split spin of a localized carrier in the organic material has its individual nuclear environment. This environment produces a random hyperfine field which adds to the external field. As a result, each two-level system possesses its individual detuning, $\Delta$, from the resonance. Modification of the Rabi oscillations due to the detuning is given by Eq. (1.6). The observed Rabi oscillations are, therefore, proportional to the oscillating part of Eq. (1.6) averaged over the distribution of $\Delta$. In this situation, valuable information about the effect of the environment on the Rabi oscillations can be derived not from the time domain, but rather from the frequency domain, as it was suggested, e.g., in Ref. [24]. If one performs a Fourier transform of the measured Rabi oscillations, Eq. (1.6), then the integral averaging over $\Delta$ reads

$$\begin{aligned} I(s) &= \int d\Delta \left(\frac{4\Omega_R^2}{4\Omega_R^2+\Delta^2}\right) \delta\left[s-\sqrt{4\Omega_R^2+\Delta^2}\right] f(\Delta) \\ &= \frac{4\Omega_R^2}{|s|\sqrt{s^2-4\Omega_R^2}} f\left(\sqrt{s^2-4\Omega_R^2}\right), \end{aligned} \tag{1.33}$$

where $f$ is the distribution function of the $z$-projection of a hyperfine field. The remarkable property of $I(s)$ is that it diverges as $s$ approaches to $\Omega_R$ from above. This divergence suggests that the major contribution to $I(s)$ comes from the two-level systems for which detuning is anomalously small, and is similar to the divergence of the density of states in a superconductor in the vicinity of the band-edges. It indicates that no matter how strong the disorder is, the Rabi oscillations can, in principle, be observed from analysis of $I(s)$. This analysis should be performed by fitting the measured $I(s)$ by the function

$$I(s) \propto \frac{\Theta(s-2\Omega_R)}{\sqrt{s-2\Omega_R}} \exp\left[-\frac{2\Omega_R}{\Delta_0^2}(s-2\Omega_R)\right]. \tag{1.34}$$

From the exponential fall-off in Eq. (1.34), one can infer the magnitude of the disorder, $\Delta_0$, which is the width of the distribution function $f(\Delta)$.

Certainly, the realistic spectra of the Fourier transform of the Rabi oscillations do not have a sharp boundary at $s = \Omega_R$, see Ref. [24]. The reason for this is the decay, $\exp(-\gamma t)$, of the Rabi oscillations with time due to inelastic processes. Due to this decay, the sharp boundary in $I(s)$ will get smeared in the interval $|s-2\Omega_R| \sim \gamma$. It is important, however, that if the decoherence time, $\gamma^{-1}$ is long enough, $\gamma \ll \Delta_0^2/\Omega_R$, the tail of $I(s)$

in the domain $s < 2\Omega_R$ remains much narrower than the tail towards large $s$. Then the behavior of $I(s)$ in the domain $|s - 2\Omega_R| \sim \gamma$ can be simply established, since the distribution function of $\Delta$ can be replaced by $f(0)$ in this domain. Then we have

$$I(s) = \gamma f(0) \int_{-\infty}^{\infty} \frac{d\Delta}{\left(s - \sqrt{4\Omega_R^2 + \Delta^2}\right)^2 + \gamma^2}. \tag{1.35}$$

Substituting $\Delta = 2\Omega_R \sinh u$, we get

$$I(s) = \frac{1}{2i} \int du \left[ \frac{s + i\gamma}{\Omega_R \cosh u - (s + i\gamma)} - \frac{s - i\gamma}{\Omega_R \cosh u - (s - i\gamma)} \right]. \tag{1.36}$$

From Eq. (1.36), it can be seen that the main contribution of the integral comes from small $u$, i.e., from *small* detuning. Using this fact, we evaluate the integral, yielding

$$I(x) = \pi \left( \frac{\gamma}{2\Omega_R} \right)^{1/2} \left[ \frac{\sqrt{x^2 + 1} + x}{x^2 + 1} \right]^{1/2}, \tag{1.37}$$

where

$$x = \frac{s - 2\Omega_R}{\gamma}. \tag{1.38}$$

From Eq. (1.37), we see that the broadening remains asymmetric. In other words, the smearing of the right-edge, $x > 0$, is wider than the left-edge, $x < 0$. Graphical representation of Eq. (1.37) is shown in Fig. 1.1. When comparing our findings, Fig. 1.1, to the experimentally observed Rabi oscillations, Fig. 1.2, we see the same characteristics: a narrower tail for small frequencies below the Rabi frequency than for frequencies above.

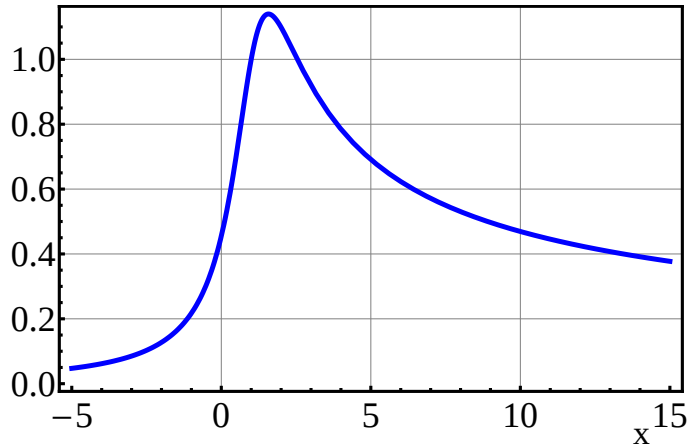


**Figure 1.1**: The broadening of the Rabi frequency-peak in the frequency domain is illustrated from Eq. (1.37). We see that the smearing of the left-edge is narrower than for the right-edge.

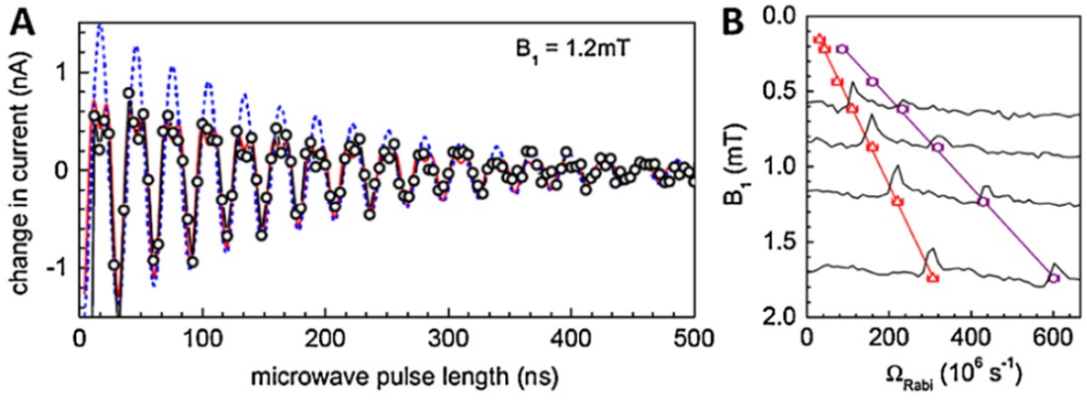


**Figure 1.2**: Plot of the measured Rabi oscillations on pairs of electrostatically bound charge carriers, for weak spin-exchange coupling is shown in (a); while in (b), the Fourier transform spectra of Rabi oscillations obtained at different $B_1$ field strengths is shown, from Ref. [30]. The red line corresponds to the frequency $\Omega_R$ where both spins precess independently, while the purple line corresponds to $2\Omega_R$ where the spin pair precesses jointly.

## 1.2 References

[1] I. I. Rabi, Phys. Rev. **51**, 652 (1937).

[2] F. Bloch and A. Siegert, Phys. Rev. **57**, 522 (1940).

[3] D. R. McCamey, K. J. van Schooten, W. J. Baker, S.-Y. Lee, S.-Y. Paik, J. M. Lupton, and C. Boehme, Phys. Rev. Lett. **104**, 017601 (2010).

[4] D. R. McCamey, K. J. van Schooten, W. J. Baker, S.-Y. Lee, S.-Y. Paik, J. M. Lupton, and C. Boehme, Phys. Rev. Lett. **104**, 017601 (2010).

# CHAPTER 2

# RABI-VIBRONIC RESONANCE WITH LARGE NUMBER OF VIBRATIONAL QUANTA

## 2.1 Introduction

As mentioned in the Preface, coupling to the *dynamic* environment tends to damp the Rabi oscillations [1] of a resonantly driven two-level system via the random shifts of the levels $E_1$ and $E_2$. This mechanism is at work only at finite temperature. It is also assumed that the dynamics of the environment are completely independent of the dynamics of the two-level system. Such a common perception misses the following mechanism of "communication" between the two-level system and the environment, which persists even at zero temperature. Namely, the two-level system, undergoing Rabi oscillations, sets the environment into motion. Then the driven environment exercises *feedback* on the two-level system. This mechanism is schematically illustrated in Fig. 2.1 and is uncovered in the present thesis for the first time. Clearly, it does not cause the decay of the Rabi oscillations. Rather, due to this mechanism, the Rabi oscillations acquire the *collective* character. To illuminate this mechanism, in the present chapter, we consider a particular form of environment for which this mechanism is most efficient. Usually, the environment is viewed as a medium with a continuous spectrum of modes. Less common is the situation when the environment possesses a single or several well-defined frequencies. For concreteness, we will consider the situation depicted in Fig. 2.2 when the lower level of the two-level system is coupled to an oscillator (a mass $M$ and a spring), which represents a single vibrational mode. Obviously, coupling to the oscillator has a strong effect on the Rabi oscillations in the regime of the vacuum Rabi splitting [5] when the oscillator frequency $\omega_0$ is close to the transition frequency $\omega_{12}$. It is less obvious what effect the coupling to the oscillator will have on the Rabi oscillations when $\omega_0$ is much smaller than $\omega_{12}$ and is comparable to the Rabi frequency $\Omega_R$. One can argue on physical

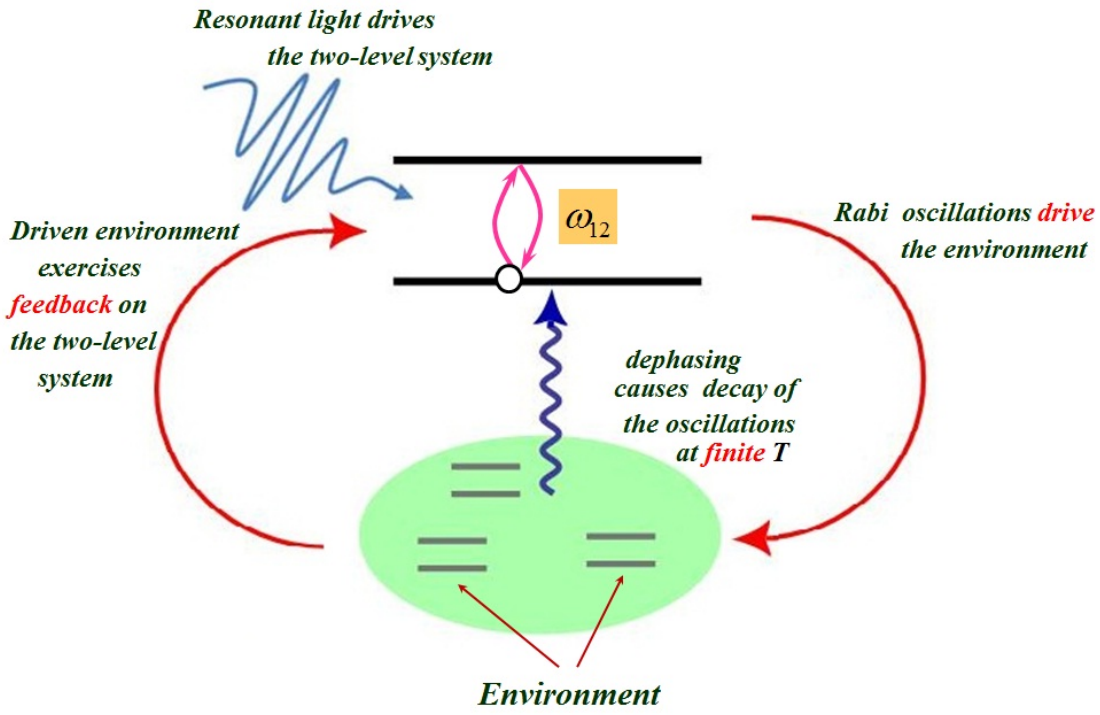


**Figure 2.1**: Illustration describing the main idea. The environment is modeled as an ensemble of harmonic oscillators that are coupled to the two-level system. Namely, through coupling, the two-level system drives the environment and in turn, the environment drives the two-level system.

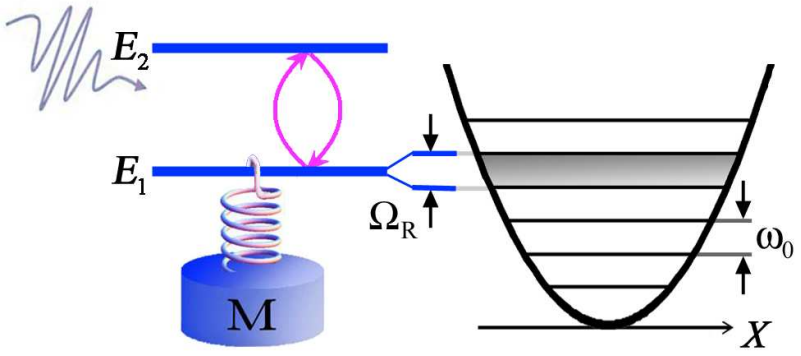


**Figure 2.2**: A schematic illustration of the system under consideration. The two-level system is driven by near-resonant light, $\omega_{12} \approx E_2 - E_1$. The level $E_1$ is linearly coupled to a classical oscillator with frequency $\omega_0$. The Rabi oscillations are strongly modified when $\omega_0$ is close to $\Omega_R$, where $\Omega_R$ is the Rabi frequency.

grounds that the effect of coupling on the Rabi oscillations will be strong in the vicinity of the condition $\omega_0 \approx \Omega_R$, which we dub *Rabi-vibronic resonance*. Indeed, consider the Hamiltonian

$$H = \mu \hat{X} \hat{n}_1, \tag{2.1}$$

describing the linear coupling. Here $\hat{X} = \frac{1}{\sqrt{2M\omega_0}}(b^\dagger + b)$ is the operator of the oscillator displacement, $b^\dagger$ is a creation operator of the vibrational quantum, $\hat{n}_1$ is the occupation of the level $E_1$, and $\mu = \left(2M\omega_0^3\right)^{1/2}\lambda$, where $\lambda$ is a dimensionless coupling constant. In definition of $\hat{X}$, $\mu$, and thereafter we, set $\hbar = 1$. In the course of the Rabi oscillations, the average $\hat{n}_1$ changes with time as

$$n_1(t) = \frac{1}{2}\left(1 + \cos \Omega_R t\right). \tag{2.2}$$

Then at $\Omega_R \approx \omega_0$, the second term in Eq. (2.2) gives rise to a resonant driving force acting on the oscillator. In turn, the strongly driven oscillator provides a resonant feedback [6, 7] on the two-level system. Thus, as $\Omega_R$, which is proportional to the ac field driving the two-level system, increases, we expect the Rabi oscillations to be strongly modified near the resonant condition. Among possible experimental realizations of the situation, Fig. 2.2 is a suspended carbon nanotube in an inhomogeneous electric field, which creates a confinement for an exciton [8, 9, 10, 11], illustrated in Fig. 2.3. The localized exciton can be viewed as a two-level system. Bending modes have discrete frequencies due to finite nanotube length and can be viewed as oscillators with very low friction. While a typical transition frequency in such a system is [13, 12] $\omega_{12} \sim 10^{15}$ Hz, the oscillator

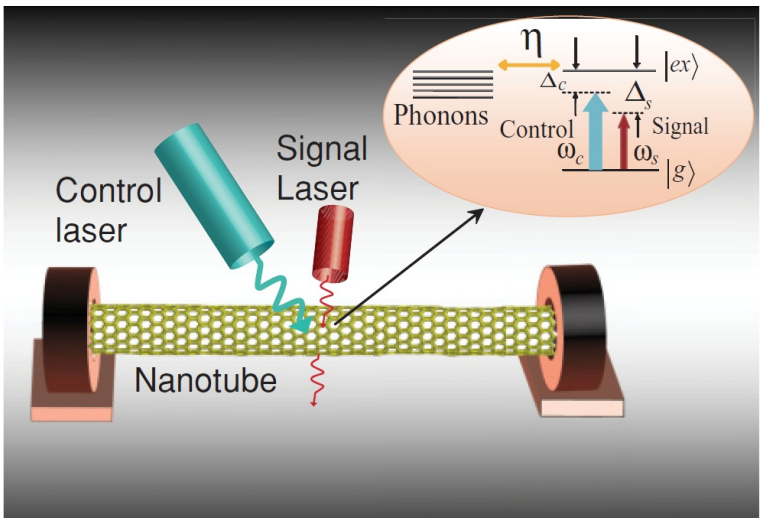


**Figure 2.3**: Illustration of the experimental realization of the system considered from Ref. [11]. It is well known that nanotubes have inhomogeneities which play the role of the confining potential for the electron and hole, frequency $\omega_{12} \sim 10^{15} Hz$. Then the nanotube itself acts as a harmonic oscillator with frequency $\omega_0 \sim 10^9 Hz$.

frequency [10] is much smaller, $\omega_0 \sim 10^9$ Hz. The resonant condition can be achieved by adjusting the illumination intensity.

Another area in which the situation Fig. 2.2 is relevant, is the cavity QED, [14] where a two-level system is realized in the form of a superconducting qubit, while the oscillator is a $LC$ circuit. The majority of experimental and theoretical studies in this field are focused on the strong coupling in the domain $\omega_0 \approx \omega_{12}$. However, in experiments from Refs. [15, 16], an ac driven superconducting qubit was coupled to a "slow" $LC$ oscillator tuned to $\Omega_R$. It was observed that the noise spectrum of the oscillator exhibits a Lorentzian peak [17] as a function of $\Omega_R - \omega_0$. In theoretical papers [18, 19, 20] initiated by the experiment in Ref. [15], collective motion of the oscillator coupled to a qubit was studied within the density-matrix formalism, and both subsystems were treated quantum mechanically. In view of the complexity of this description, final results were obtained numerically for particular values of a coupling parameter $\lambda$. A notable finding of Refs. [18, 19, 20] is that, in the vicinity of the condition $\omega_0 \approx \Omega_R$, collective Rabi-vibronic motion becomes *bistable*.

There are still several basic questions to be answered, among which are the following:

(i) How does the frequency, $s$, of the collective oscillations depend on $\lambda$?

(ii) What is the width of the resonance, i.e., the domain $\delta_0 = \Omega_R - \omega_0$ of the Rabi frequencies where Rabi oscillations are modified due to coupling?

(iii) How does the decay of the Rabi oscillations depends on the oscillator friction?

The above questions are studied in the present paper. Our main finding is that the width of the Rabi-vibronic resonance is small for weak coupling, namely,

$$\delta_0 = \lambda^{4/3}\omega_0 = \omega_p^{2/3}\omega_0^{1/3} \ll \omega_0, \tag{2.3}$$

where $\omega_p = \lambda^2\omega_0$ is the polaronic shift. Equation (2.3) suggests that, while $\delta_0$ is much smaller than $\omega_0$, it is much bigger than $\omega_p$. Most importantly, Eq. (2.3) guarantees that, in the resonant domain $(\Omega_R - \omega_0) \sim \delta_0$, the oscillator is highly excited and can be treated as *classical*. This allows the analytical description of the resonance. In this regard, the situation we consider, a two-level system coupled to a classical oscillator, is similar to the *Rabi resonance* considered in Refs. [21, 22], where the two-level system was driven by *two classical fields*: one with frequency close to $\omega_{12}$ and one with frequency close to $\Omega_R$.

We will see that in the domain $(\Omega_R - \omega_0) \sim \delta_0$, the frequency $s$ of collective oscillations differs from $\Omega_R$ also by $\sim \delta_0$. Bistable behavior of the dependence $s(\Omega_R)$ emerges naturally within our approach; the frequency jump rate between two stable regimes is also $\sim \delta_0$.

In addition, in the present paper, we study how the Rabi-vibronic resonance depends on detuning $\Delta$ of the driving frequency from $\omega_{12}$, on intrinsic anharmonicity of the oscillator, and how the modified Rabi oscillations decay with time due to relaxation of the two-level system and due to friction in the oscillator.

## 2.2 Basic equations

We first assume that the displacement $X(t)$ is a classical variable and will later check this assumption. The equation of motion for $X(t)$ reads

$$\ddot{X} + \gamma\dot{X} + \omega_0^2 X = \frac{\mu}{2M}\big(1 - w\big), \tag{2.4}$$

where $w = 1 - 2n_1$ is the population inversion, and $\gamma$ is the friction in the oscillator. The evolution of $w$ with time is described by the system of optical Bloch equations. We write them for variables $w(t)$, $u(t)$, and $v(t)$, where $u(t)$ and $v(t)$ are the real and imaginary parts of the nondiagonal elements of the density matrix, respectively, [23]

$$\dot{w}(t) = -\Omega_R v - \Gamma\big(1 + w\big), \tag{2.5}$$

$$\dot{u}(t) = -\Big(\Delta - \mu X(t)\Big)v - \frac{\Gamma}{2}u, \tag{2.6}$$

$$\dot{v}(t) = \Big(\Delta - \mu X(t)\Big)u + \Omega_R w - \frac{\Gamma}{2}v, \tag{2.7}$$

where $\Gamma$ is the relaxation rate of the excited state. Note that, while the oscillator is driven by $w(t)$, it exercises a feedback on the two-level system via $u(t)$ and $v(t)$.

We require that the level $E_1$ at $t = 0$ be occupied while the level $E_2$ is empty, i.e., $w(0) = -1$. We also assume that the dipole moment and dipole current are initially zero, leading to $v(0) = 0$ and $u(0) = 0$, respectively. From Eq. (2.5), we see that the initial conditions for $v$ and $w$ require that $\dot{w}(0) = 0$.

## 2.3 Modified Rabi oscillations

### 2.3.1 Oscillation frequency

The system Eqs. (2.5)-(2.7) can be reduced to two coupled equations by excluding $v(t)$ and expressing $u(t)$ in terms of $w(t)$. Then one gets

$$\ddot{w} + \frac{3}{2}\Gamma\dot{w} + \Big(\Omega_R^2 + \frac{\Gamma^2}{2}\Big)w + \frac{\Gamma^2}{2} = -\Omega_R\Big(\Delta - \mu X(t)\Big)u(t), \tag{2.8}$$

$$u(t) = -\int_0^t \frac{dt'}{\Omega_R} e^{\Gamma(t'-t)/2}\big(\mu X(t') - \Delta\big)\Big[\dot{w}(t') + \Gamma\big(1 + w\big)\Big]. \tag{2.9}$$

We start from the simplest case, $\Gamma \to 0$, $\Delta \to 0$, $\gamma \to 0$, and search for a solution of the system Eqs. (2.4), (2.8), and (2.9), in the form $w(t) = -\cos st$. Substituting this form into Eq. (2.4), we find the displacement

$$X(t) = \frac{\mu \cos st}{2M\left(\omega_0^2 - s^2\right)} = X_0 \cos st. \tag{2.10}$$

Static displacement, $\mu/2M\omega_0^2$, can be neglected compared to the oscillating part. Substituting $X(t)$ into Eq. (2.9), we find $u(t)$

$$u(t) = -\frac{\mu^2 \left(1 - \cos 2st\right)}{8M\Omega_R\left(\omega_0^2 - s^2\right)}. \tag{2.11}$$

Substituting Eqs. (2.10) and (2.11) into the right-hand side of Eq. (2.8), and equating the terms $\propto \cos st$ in both sides, we find a closed equation for $s$,

$$\Omega_R^2 - s^2 = \frac{\omega_p^2 \omega_0^4}{8\left(\omega_0^2 - s^2\right)^2}. \tag{2.12}$$

Thus coupling to the oscillator causes the shift of the oscillation frequency from $\Omega_R$, as stated in the Introduction. Note that the term $\propto \cos 2st$ in $u(t)$ will also give rise to the nonresonant contribution $\propto \cos 3st$ in $w(t)$, causing a weak anharmonicity of the oscillations. Away from resonance, we can substitute $s = \Omega_R$ into the right-hand side of Eq. (2.12). Then Eq. (2.12) yields a correction to the Rabi frequency due to coupling to the oscillator

$$s = \Omega_R - \frac{\omega_p^2 \omega_0}{64\left(\omega_0 - \Omega_R\right)^2}. \tag{2.13}$$

This expression is valid only if the correction on the right-hand side is much smaller than $\left(\omega_0 - \Omega_R\right)$. Equating the correction to $\left(\omega_0 - \Omega_R\right)$, we find that the width of the resonance, $\left(\omega_0 - \Omega_R\right) \sim \delta_0$, is given by Eq. (2.3).

Recall now our basic assumption that the oscillator is classical. We are now in position to verify this assumption. In the resonant domain, the amplitude $X(t)$ can be estimated from Eq. (2.10) as $X \sim \mu/M\omega_0\delta_0$. Then for the ratio of the energy of oscillations to the vibrational quantum $\omega_0$, we get the following estimate:

$$\frac{MX_0^2\omega_0^2}{\omega_0} \sim \left(\frac{\omega_0}{\omega_p}\right)^{1/3} = \lambda^{-2/3} \gg 1. \tag{2.14}$$

Thus, for weak coupling, the classical treatment of the oscillator is justified.

### 2.3.2 Vicinity of the resonance

To incorporate finite detuning $\Delta$ into Eq. (2.12), it is convenient to rewrite Eq. (2.8) keeping all $\Delta$-dependent terms in the right-hand side,

$$\ddot{w} + \Omega_R^2 w + \mu^2 X(t) \int_0^t dt' X(t') \dot{w}(t') = \Delta\big(\mu X(t) - \Delta\big)\big[w(t) + 1\big] + \Delta\mu \int_0^t dt' X(t') \dot{w}(t'). \tag{2.15}$$

The term $\propto \Delta^2$ in the right-hand side leads to a standard modification of the Rabi frequency to $\left(\Omega_R^2 + \Delta^2\right)^{1/2}$. The last term is proportional to $\sin^2 st$, and does not contain the first harmonics. The term $\propto \cos st$ comes from the combination $\Delta\mu X(t)$ in the right-hand side. Emergence of this term, which is odd in detuning, is the result of the coupling of the vibronic mode only to the level $E_1$. This term results in the following modification of Eq. (2.12):

$$\Omega_R^2 + \Delta^2 - s^2 = \frac{\omega_p^2 \omega_0^4}{8\left(\omega_0^2 - s^2\right)^2} - \frac{\omega_p \omega_0^2 \Delta}{\omega_0^2 - s^2}. \tag{2.16}$$

Near the resonance $\left(\Omega_R - \omega_0\right) \ll \omega_0$, this equation can be simplified. Upon introducing dimensionless variables,

$$z = \frac{s - \omega_0}{\omega_p^{2/3} \omega_0^{1/3}}, \tag{2.17}$$

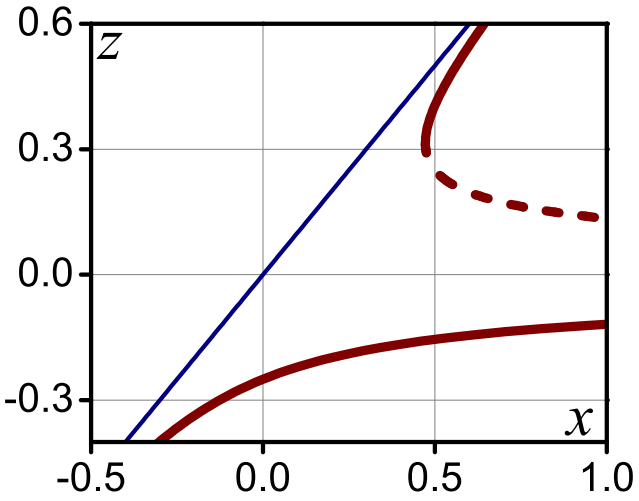


**Figure 2.4**: Red line: Dimensionless frequency $z$ defined by Eq. (2.17), versus the dimensionless deviation $x$ from the $\Omega_R = \omega_0$ is plotted from Eq. (2.19). The unstable solution is shown with the dashed line. The blue line $z(x) = x$, corresponds to the absence of coupling to the oscillator.

$$x = x' + 8\Delta'^2, \quad x' = \frac{\Omega_R - \omega_0}{\omega_p^{2/3}\omega_0^{1/3}}, \tag{2.18}$$

Eq. (2.16) assumes the form

$$(z - x)z^2 + \Delta' z = -\frac{1}{64}, \tag{2.19}$$

where dimensionless detuning $\Delta'$ is defined as

$$\Delta' = \frac{\Delta}{4\omega_p^{1/3}\omega_0^{2/3}}. \tag{2.20}$$

Note that characteristic detuning $\Delta \sim \omega_p^{1/3}\omega_0^{2/3}$ is much bigger than the width of the resonance $\delta_0$, but much smaller than $\Omega_R$. Figure 2.4 shows the solution of Eq. (2.19) for zero detuning. The blue line $z = x$ corresponds to the Rabi oscillations without coupling. We see that bistability develops for $x > 3 \times 2^{-8/3}$. At $x = 3 \times 2^{-8/3}$, the frequency $s$ experiences a jump by $2^{-8/3}\delta_0$. Two values of $z$ corresponding to stable solutions define, via Eq. (2.17), two frequencies of the modified Rabi oscillations. They also define two corresponding amplitudes of the oscillator,

$$X = \left(\frac{1}{2\lambda^{1/3}z}\right)(2M\omega_0)^{-1/2} \tag{2.21}$$

The last factor in Eq. (2.21) is the amplitude of a zero-point motion of the oscillator. As the dimensionless deviation $x$ from resonance increases, the upper branch approaches $z = x$. For this branch, the frequency of the Rabi oscillations is close to $\Omega_R$ and the amplitude of the oscillator is small. For the lower branch, $z$ is small, i.e., the frequency of the oscillations approaches $\omega_0$ with increasing $x$. For this branch, the oscillator is highly excited.

Figures 2.5 and 2.6 illustrate the effect of detuning on the frequency of oscillations $s$. Note that there is a qualitative difference between Fig. 2.4 for zero detuning, and Figs. 2.5, 2.6 for positive and negative detunings, respectively. For zero detuning, the domain of bistability exists only when $\Omega_R > \omega_0$, whereas for finite detuning, bistable regions emerge both to the left and the right from the resonance. As one changes the dimensionless deviation $x'$ from the resonance, from negative to positive, for $\Delta' = 0$, bistability corresponds to $x' > 3 \times 2^{-8/3}$. For finite positive detuning, $\Delta' > 0$, the first domain of bistability occurs at $x' < 0$, then disappears, and re-emerges at positive $x'$ greater than $3 \times 2^{-8/3}$. Conversely, finite negative detuning simply broadens the domain of bistability as compared to $\Delta = 0$. The bistable region starts for $x' < 0$. A peculiar dependence of $s$ on the deviation from resonance is also reflected in the amplitude of the oscillator. This effect is discussed in Sec. 2.4.

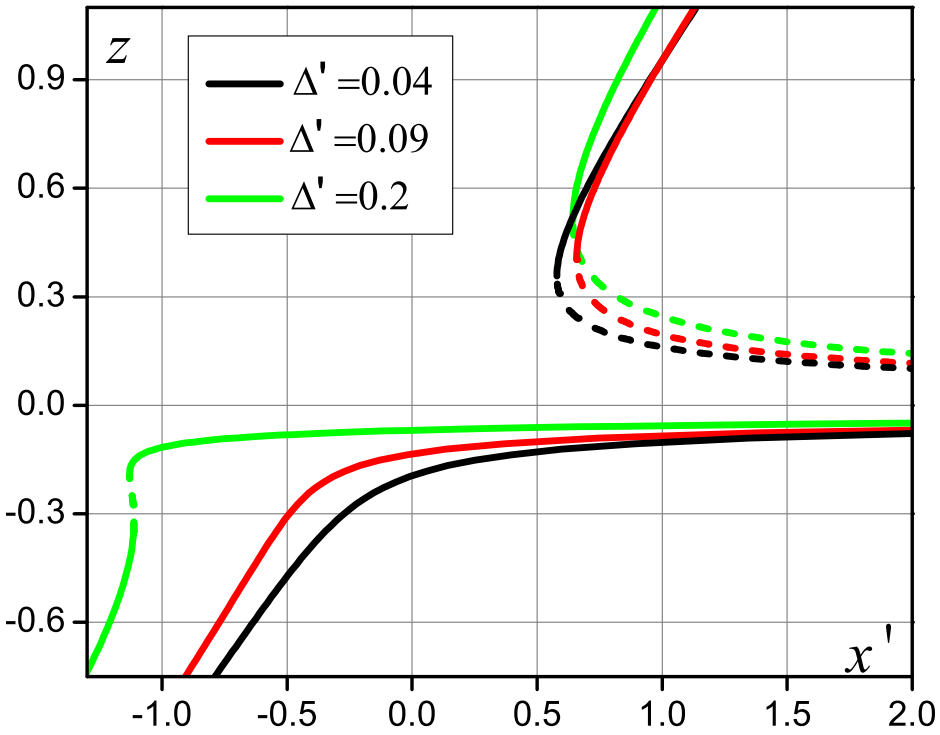


**Figure 2.5**: Dimensionless frequency $z$ of oscillations of adriven two-level system is plotted from Eq. (2.19) versus the dimensionless deviation $x'$ from the resonance for three positive dimensionless detunings $\Delta'$, defined by Eq. (2.20). As detuning increases, the unstable branch shifts from positive $z$ to negative $z$, and both stable values of $z$ become positive (for positive $x'$) or negative (for negative $x'$).

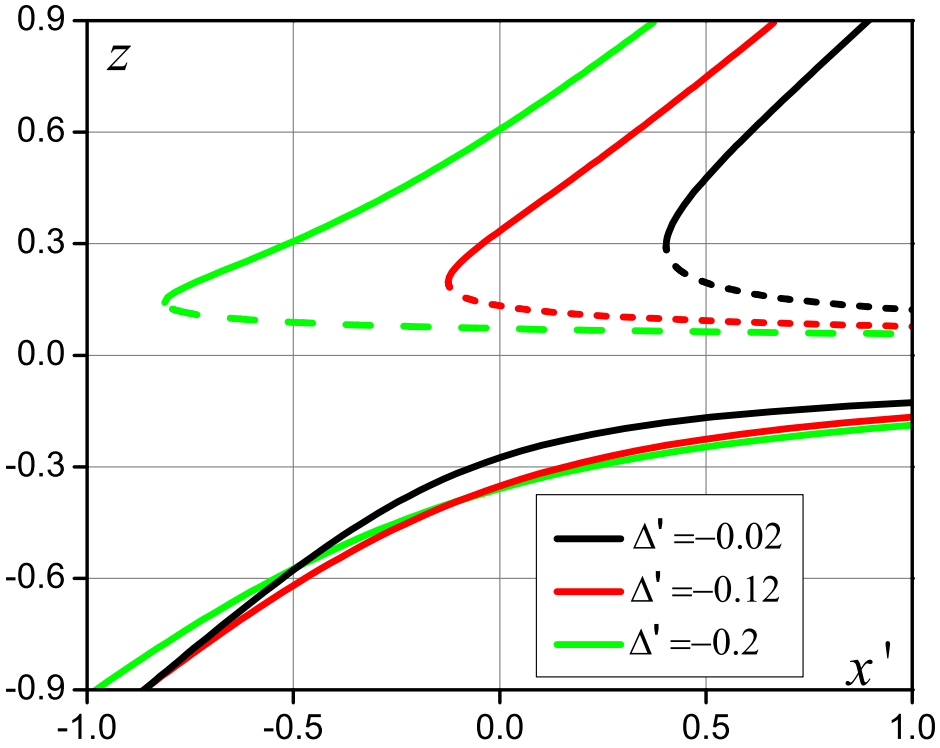


**Figure 2.6**: The same as in Fig. 2.5 for three negative detunings. Note that negative $\Delta'$ broadens the range of bistability.

### 2.3.3 Effect of intrinsic anharmonicity of the oscillator

Suppose that in addition to the harmonic part of the oscillator energy, $M\omega_0^2 X^2/2$, a weak intrinsic anharmonicity, $\kappa X^4/4$, is present. Then Eq. (2.10) will assume the form

$$\frac{3}{4}\kappa X_a^3 + \big(\omega_0^2 - s^2\big)X_a = \frac{\mu}{2M}. \tag{2.22}$$

The second relation, $s^2 = \Omega_R^2 - \mu^2 X_a^2/8$, between the amplitude $X_a$ and the frequency $s$, which follows from Eq. (2.8), remains unchanged. It is now more convenient to express $s$ from this relation and substitute it into Eq. (2.22). This yields a cubic equation for $X_a$,

$$2\omega_0\big(\omega_0 - \Omega_R\big)X_a + \frac{6\kappa + \mu^2}{8}X_a^3 = \frac{\mu}{2M}. \tag{2.23}$$

If we now set $\kappa = 0$, then Eq. (2.23) will have multiple real solutions for $X_a$ in the domain $\big(\Omega_R - \omega_0\big) < -3 \times 2^{-8/3}\delta_0$, i.e., the same as determined from Eq. (2.19) with $\Delta' = 0$. We see from Eq. (2.23) that, depending on the sign of $\kappa$, intrinsic anharmonicity can either shift the threshold of bistability to the left (for positive $\kappa$) or to the right (for negative $\kappa$). Anharmonicity will also affect the magnitude of the jump of the frequency $s$ of the oscillations. This magnitude will get modified from $2^{-8/3}\delta_0$ to $2^{-8/3}\delta_0\big(1 + 6\kappa/\mu^2\big)^{-2/3}$, i.e., the jump will become smaller for $\kappa < 0$.

## 2.4 Decay of the oscillations

Up to now we disregarded both mechanisms of dissipation: finite relaxation $\Gamma$ and the friction in the oscillator, $\gamma$. Rabi oscillations will decay with the rate $\Upsilon$, which is determined by $\Gamma$, in the regime $\Gamma \gg \gamma$, or by friction in the regime $\Gamma \ll \gamma$. We will consider both cases separately. We emphasize that, as the oscillations decay, so does the coupling between the oscillator and the two-level system. Thus, the decay will be accompanied by the change of frequency back to $\Omega_R$. We cannot capture this evolution of frequency with time analytically. To find the decay rate $\Upsilon$ only, we will adopt the approach based on the energy conservation.

### 2.4.1 Friction-dominated regime, $\gamma \gg \Gamma$

Upon neglecting $\Gamma$ in Eq. (2.8) and setting $\Delta = 0$ we have

$$\ddot{w} + \Omega_R^2 w = -\mu^2 X(t)\int_0^t dt' X(t')\dot{w}(t'). \tag{2.24}$$

Multiplying both sides by $\dot{w}$ and integrating from 0 to $t$, we arrive to the following conservation law:

$$\frac{\dot{w}^2}{2} + \frac{\Omega_R^2}{2}(w^2 - 1) = -\frac{\mu^2}{2}\left(\int_0^t dt' X(t')\dot{w}(t')\right)^2. \tag{2.25}$$

The right-hand side describes the energy exchange between the two-level system and the oscillator.

As a next step, we multiply the equation of motion of the oscillator Eq. (2.4) by $\dot{X}$ and integrate from 0 to $t$. Then we arrive at the second conservation law,

$$\frac{\dot{X}^2}{2} + \frac{\omega_0^2 X^2}{2} + \gamma \int_0^t dt' \dot{X}^2(t') = -\frac{\mu}{2M} \int_0^t dt' w(t') \dot{X}(t'). \tag{2.26}$$

At long time $t \gg \Upsilon^{-1}$ we have $\dot{w}$, $w \to 0$ and also $\dot{X}$, $X \to 0$. Then the left-hand side of Eq. (2.25) for $w$ turns to $-\Omega_R^2/2$. Combining Eqs. (2.25) and (2.26), we arrive at the relation

$$\Omega_R = 2M\gamma \int_0^\infty dt' \dot{X}^2(t'). \tag{2.27}$$

This relation is convenient to find the decay rate $\Upsilon$ because it contains only $\dot{X}^2$, which is insensitive to the change of frequency in the course of decay. Substituting $\dot{X}^2 \propto \exp[-2\Upsilon t]$, we find the following relation between $\Upsilon$ and the amplitude of the oscillations at time $\lesssim 1/\Upsilon$:

$$\Upsilon = \gamma(MX_0^2 \Omega_R). \tag{2.28}$$

In fact, Eq. (2.28) does not prove that decay is exponential. In the next subsection, we will see that it becomes exponential only for long times, $\Upsilon t \gg 1$. Note that the second factor in the right-hand side can be rewritten as $(MX_0^2\Omega_R^2)/\Omega_R$. The oscillator is classical when this ratio is big. Thus, we conclude that $\Upsilon \gg \gamma$, i.e., the Rabi oscillations in the region of resonance decay faster than the undriven oscillator. As a next step, we distinguish two cases of weak and strong friction. In the first case, to find $X$ that should be substituted into Eq. (2.28) one can use Eq. (2.10), obtained without friction. Then one gets

$$\Upsilon = \frac{\gamma \omega_p \Omega_R}{(\omega_0 - s)^2}, \tag{2.29}$$

where $s$ is determined from the cubic equation, Eq. (2.13). In the region of resonance, the difference $\omega_0 - s$ is $\sim \delta_0$, which yields

$$\Upsilon \sim \gamma \left(\frac{\omega_0}{\omega_p}\right)^{1/3} = \frac{\gamma}{\lambda^{2/3}}. \tag{2.30}$$

Weak friction requires that $|\omega_0 - s| \sim \delta_0 \gg \Upsilon$, i.e., $\gamma \ll \omega_p$.

In the region of strong friction, the difference $\omega_0 - s$ should be replaced by $\Upsilon$. Then Eq. (2.29) contains $\Upsilon$ in both sides. Upon solving this equation, we get

$$\Upsilon \sim \left(\frac{\gamma}{\omega_p}\right)^{1/3} \delta_0, \tag{2.31}$$

for $\gamma \gg \omega_p$. Equations (2.30) and (2.31) match when $\gamma \sim \omega_p$. The validity of this expression is limited from above by the condition that the oscillator is classical. As we replace $\omega_0 - s$ by $\Upsilon$, the estimate for $X$ is $X \sim \mu/(M\omega_0\Upsilon)$. Then the kinetic energy can be estimated as

$$M\omega_0^2\Big[\frac{\mu}{M\omega_0\Upsilon}\Big]^2 \sim \frac{\omega_p^{1/3}\omega_0^{4/3}}{\gamma^{2/3}}. \tag{2.32}$$

The condition that it is bigger than $\omega_0$ limits $\gamma$ in Eq. (2.31) to $\gamma \ll (\omega_0\omega_p)^{1/2} = \lambda\omega_0$, and correspondingly limits $\Upsilon$ to $\Upsilon \ll \delta_0(\omega_0/\omega_p)^{1/6} = \delta_0/\lambda^{1/3}$.

From Eqs. (2.30) and (2.31), we see that, upon increasing friction, the decay rate $\Upsilon$ first grows linearly with $\gamma$, and then sublinearly as $\gamma^{1/3}$. At the boundary of applicability of the classical description, we have $\Upsilon = \gamma$. For even bigger $\gamma$, classical treatment of the oscillator is not justified, but we expect that the oscillator will eventually decouple from the two-level system, and Rabi oscillations will proceed as they do in the absence of the oscillator.

It is convenient to reformulate the above results in terms of number, $m = \omega_0/\Upsilon$, of the oscillation cycles, after which the collective motion effectively stops. See Fig. 2.8. From Eqs. (2.30) and (2.31), we have

$$m = \begin{cases} \lambda^{2/3}\left(\frac{\omega_0}{\gamma}\right), & \gamma < \lambda^2\omega_0, \\ \frac{1}{\lambda^{2/3}}\left(\frac{\omega_0}{\gamma}\right)^{1/3}, & \lambda\omega_0 > \gamma > \lambda^2\omega_0. \end{cases} \tag{2.33}$$

In the crossover between weak and strong friction regimes, we have $m \sim \lambda^{-4/3}$. Equation (2.33) is illustrated in Fig. 2.7. For $\gamma > \lambda\omega_0$, the assumption of classical motion of the oscillator is violated. The boundary value of $m$ at $\gamma \sim \lambda\omega_0$ is still large, $m \sim \lambda^{-1}$.

### 2.4.2 The form of the decay

For more quantitative analysis of the decay of oscillations, it is convenient to rewrite the energy conservation law Eq. (2.25) in terms of the displacement $X(t)$. Expressing $w(t)$ from Eq. (2.4) and substituting it into Eq. (2.25), we get

$$\Big[\frac{d}{dt}\big(\ddot{X}+\gamma\dot{X}+\omega_0^2X\big)\Big]^2+\Omega_R^2\big(\ddot{X}+\gamma\dot{X}+\omega_0^2X\big)^2 = \frac{\mu^2\Omega_R^2}{4M^2}-\mu^2\left(\int_0^t dt'\Big[X\dddot{X}+\omega_0^2X\dot{X}+\gamma X\ddot{X}\Big]\right)^2. \tag{2.34}$$

The first two terms in the integrand can be presented in the form

$$X\dddot{X} + \omega_0^2 X\dot{X} = \frac{d}{dt}\Big[X\ddot{X} - \frac{\ddot{X}^2}{2} + \frac{\omega_0^2 X^2}{2}\Big], \tag{2.35}$$

so that the integral from these terms is equal to $\frac{1}{2}(\omega_0^2 - s^2)X^2(t)$. At the same time, the integral from the third term can be rewritten as $\frac{1}{2}\gamma s^2 \int_0^t dt' X^2(t')$, and estimated at $\gamma s^2 X_0^2/\Upsilon$. One can check using Eqs. (2.30) and (2.31) that both in the strong-friction and weak-friction regimes, the integral from the last term is bigger than the contribution from the first two terms. Neglecting this contribution, we can cast Eq. (2.34) in the form of an integral equation for the slow decaying amplitude $\tilde{X}$ of the oscillations.

Since $\gamma \ll |\omega_0 - s|$ in both regimes, the nonoscillating part of the left-hand side of Eq. (2.34) can be presented as

$$\frac{1}{2}(\omega_0^2 - s^2)^2(s^2 + \Omega_R^2)\tilde{X}^2 \approx \frac{\mu^2\omega_0^2\tilde{X}^2}{4M^2X_0^2}, \tag{2.36}$$

where we used the definition Eq. (2.10) of the initial amplitude $X_0$. Upon substituting Eq. (2.36) into Eq. (2.34) and introducing a dimensionless function $F(t) = \tilde{X}(t)/X_0$, we arrive at the integral equation

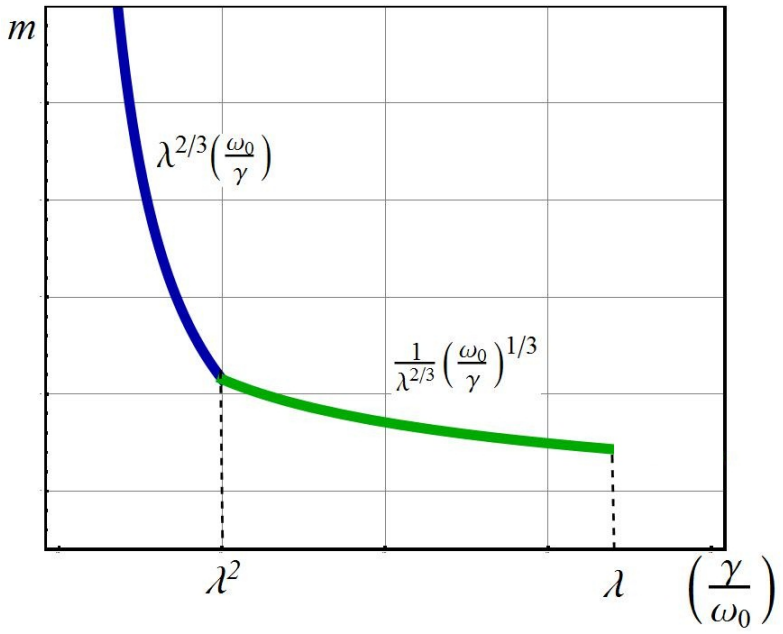


**Figure 2.7**: The number of oscillation cycles, $m$, before collective motion stops is plotted vs. the dimensionless friction of the oscillator, $\gamma/\omega_0$. For $\gamma > \omega_0$, the assumption that the oscillator motion is classical is violated.

$$F^2(t) = 1 - \Upsilon^2 \Big[ \int_0^t dt' F^2(t') \Big]^2, \tag{2.37}$$

where $\Upsilon = \gamma M X_0^2 \omega_0$ is introduced according to Eq. (2.29). It is easy to check that this equation has a simple solution,

$$F(t) = \frac{1}{\cosh \Upsilon t}. \tag{2.38}$$

We see that the decay of amplitude $\tilde{X}(t)$ becomes exponential in the limit $\Upsilon t \gtrsim 1$, as mentioned in the previous subsection.

### 2.4.3 Initial stage of the oscillations

After the ac driving field is switched on, the population inversion starts to oscillate with frequency $\Omega_R$. After some number $m'$ of the oscillation cycles the frequency crosses over to $s$. See Fig. 2.8. The question of interest is how $m'$ depends on the coupling strength $\lambda$. We will estimate $m'$ using the fact that at the initial stage, the system Eqs. (2.4) and (2.24) can be solved perturbatively in a small parameter $\omega_p/\omega_0$. To find the perturbative solution, we substitute the "bare" Rabi oscillations $w^{(0)} = -\cos(\Omega_R t)$ into Eq. (2.4) and find $X(t)$ with initial conditions $X(0) = 0$, $\dot{X}(0) = 0$. The obtained $X(t)$ together with $w^{(0)}(t)$ is then substituted into the right-hand side of Eq. (2.24). Solving this second-order differential equation with a given right-hand side, we find that the amplitude of oscillations becomes $1 - w^{(1)}(t)$, i.e., it acquires a time-dependent correction with $w^{(1)}(t)$ given by the following expression

$$w^{(1)}(t) = \frac{2\omega_p^2 \omega_0^2}{(\gamma^2 + 4\delta^2)^2} \left[ \frac{\gamma t}{2} - \frac{4\gamma\delta}{(\gamma^2 + \delta^2)} e^{-\gamma t/2} \sin \delta t - \frac{\gamma^2 - 4\delta^2}{\gamma^2 + 4\delta^2} \left( 1 - e^{-\gamma t/2} \cos \delta t \right) \right]^2, \tag{2.39}$$

where $\delta = \omega_0 - \Omega_R$. The derivation of Eq. (2.39) can be found in the Appendix. We can now estimate $m'$ as $\Omega_R t_c \approx \omega_0 t_c$, where $t_c$ is the time after which $w^{(1)}(t)$ becomes $\sim 1$. Consider first the limit $\delta \to 0$. We see that for $\gamma t \ll 1$, $w^{(1)}(t)$ grows with time as $\omega_p^2 \omega_0^2 t^4$, while for larger times, $\gamma t \gg 1$, $w^{(1)}(t)$ grows as $\left(\omega_p \omega_0 t/\gamma\right)^2$. If we determine $t_c$ from the small-$t$ asymptote, we will get

$$t_c = \frac{1}{\lambda \omega_0}, \tag{2.40}$$

and correspondingly $m' = \frac{1}{\lambda}$. For this answer to be correct, this $t_c$ should belong to the small-$t$ domain, i.e., $\gamma t_c$ should be smaller than 1. The latter condition, $\frac{\gamma}{\omega_0} \ll \lambda$, is met since it coincides with the condition that the oscillator is classical. Consider now the limit $\gamma \to 0$. For $\delta t \ll 1$, Eq. (2.39) yields $w^{(1)}(t) \sim \left(\omega_p \omega_0 t^2\right)^2$. This leads to the estimate

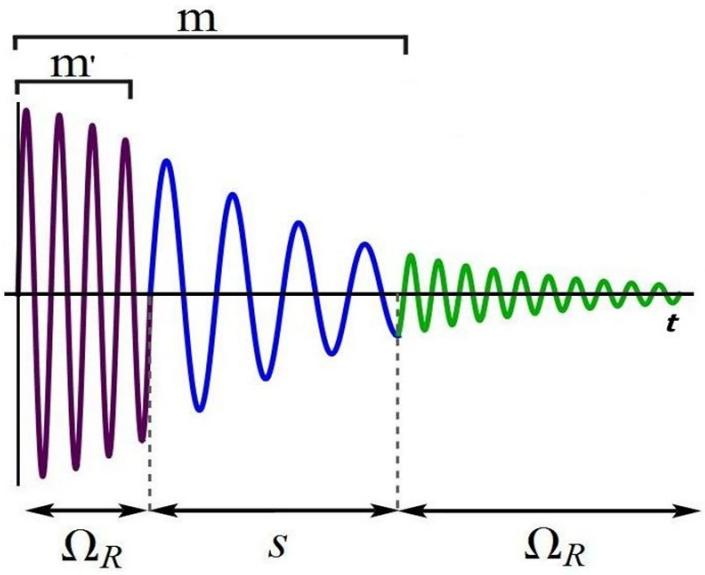


**Figure 2.8**: Illustration depicting how population inversion evolves with time. Initially, the ac driving light is switched on and the system oscillates with frequency $\Omega_R$. After some number of oscillations $m'$, the frequency crosses over to $s$, Eq. (2.13), and the system exercises collective motion. Some time later, as the oscillations decay, so does the coupling between the two-level system and the oscillator. Effectively, the two-level system and oscillator decouple and frequency changes back to $\Omega_R$. The number of oscillations cycles before collective motion stops is described by the parameter $m$.

$t_c \sim \left(\omega_p \omega_0\right)^{-1/2}$ and $m' \sim \lambda^{-1}$. Small-$t$ expansion of Eq. (2.39) is valid if the product $\delta t_c$ is small. With $t_c$ found above, this product can be rewritten in the form

$$\delta t_c \sim \left(\frac{\delta^2}{\omega_p \omega_0}\right)^{1/2}. \tag{2.41}$$

On the other hand, the oscillator can be treated as classical when the ratio in the right-hand side of Eq. (2.41) is small. Thus, taking the limit $\delta t \ll 1$ in Eq. (2.39) is justified, and the frequency of the Rabi oscillations crosses over from $\Omega_R$ to $s$ after $m' \sim \lambda^{-1}$ cycles. Correspondingly, after $\sim \lambda^{-1}$ cycles, the oscillator will "forget" about the initial phase, imposed by the initial conditions, and will execute a forced harmonic motion with frequency $s$.

In conclusion of this subsection, we note that for the entire scenario of the collective oscillations to be consistent, the time during which the collective motion is established must be shorter than the time during which these oscillations decay. The corresponding condition is $m' < m$. It follows from Eq. (2.33) and $m' = \frac{1}{\lambda}$ that this condition is satisfied

in the the entire interval $\gamma < \lambda\omega_0$, namely, $m$ is always bigger than $\lambda^{-1}$, while $m'$ is always smaller than $\lambda^{-1}$.

### 2.4.4 Relaxation-dominated regime, $\Gamma \gg \gamma$

At finite relaxation rate of the two-level system Eq. (2.26) assumes the form

$$\frac{\dot{w}^2}{2} + \frac{1}{2}\left(\Omega_R^2 + \frac{\Gamma^2}{2}\right)\left(w^2 - 1\right) + \frac{\Gamma^2}{2}\left(w + 1\right) + \frac{3}{2}\Gamma\int_0^t dt'\dot{w}^2 = \\ -\mu^2\int_0^t dt' X(t')\dot{w}(t')\int_0^{t'} dt'' e^{\Gamma(t''-t')/2} X(t'')\left[\dot{w}(t'') + \Gamma(1+w)\right]. \qquad (2.42)$$

Without coupling to the oscillator, the right-hand side is zero, and Eq. (2.42) describes the decay of the Rabi oscillations due to relaxation. Indeed, upon substituting $\dot{w} = \Omega_R \sin\left(\Omega_R t'\right)\exp(-\Upsilon t')$ and taking the limit $t \to \infty$, the last term in the left-hand side takes the value $3\Gamma\Omega_R^2/8\Upsilon$, which leads to $\Upsilon = 3\Gamma/4$. Naturally, this value of $\Upsilon$ follows directly from Eqs. (2.5) and (2.7). Finite coupling to the oscillator would increase the decay rate only if at $t \to \infty$, the integral in the right-hand side exceeds $\Omega_R^2$. Contribution of the second term in the square brackets to the integral can be estimated upon noticing that the product $X(t'')w(t'')$ is a slow function. Assuming that $X$ and $w$ both decay as $\exp(-\Upsilon t'')$ and that $\Upsilon \gg \Gamma$, the integral over $t'$ reduces to $\int_0^\infty dt' t' \sin(2st')\exp(-2\Upsilon t') = \Upsilon/s^3 \approx \Upsilon/\omega_0^3$. Then one gets the estimate $\omega_p^2\Upsilon\Gamma/\left(\omega_0 - s\right)^2$ for this contribution. Since $\omega_0 - s$ cannot be smaller than $\Upsilon$, this contribution cannot exceed $\omega_p^2$, which is much smaller than $\Omega_R^2$. The contribution from the first term in the square brackets also cannot exceed $\Omega_R^2$. This becomes apparent upon performing integration by parts, after which the contribution from the first term assumes the form

$$-\Gamma\mu^2\int_0^\infty dt' e^{-\Gamma t'}\left(\int_0^{t'} dt'' e^{\Gamma t''/2} X(t'')\dot{w}(t'')\right)^2. \qquad (2.43)$$

If $X$ and $\dot{w}$ decay much faster than $\exp(-\Gamma t''/4)$, the inner integral saturates at times $t' \ll \Gamma$. Then the contribution Eq. (2.43) can be estimated as $\Omega_R^2\omega_p^2/\left(\omega_0 - s\right)^2$, which is again much smaller than $\Omega_R^2$. We thus conclude that, while coupling to the oscillator modifies the frequency, the decay of the Rabi oscillations in the relaxation-dominated regime is always dominated by the relaxation rate.

## 2.5 Number of vibrational quanta

We studied the behavior of the frequency of the Rabi oscillations near the the resonance $\Omega_R = \omega_0$. The number of vibrational quanta $N$ is also sensitive to the deviation,

$\Omega_R - \omega_0$, from the resonance and to the detuning $\Delta$. Since $N = M\omega_0^2 X^2/\omega_0$ (we set $\hbar = 1$), it can be expressed using Eq. (2.21), as the following:

$$N = \left(\frac{1}{\lambda^2}\right)^{1/3} \frac{1}{16z^2} = \left(\frac{\omega_0}{\omega_p}\right)^{1/3} \frac{1}{16z^2}, \tag{2.44}$$

where $z$ is the solution of Eq. (2.19). The dependence of $N$ on dimensionless deviation $x'$ and dimensionless detuning $\Delta'$ is plotted in Fig. 2.9. The values of $N$ shown correspond only to stable regimes of oscillations. The line of bifurcation points separates the $(x', \Delta')$ domains with and without bistability in Fig. 2.9. In the domain of bistability, the higher and lower values of $N$ coincide along the red line. Away from the red line, the high-$N$ and the low-$N$ values differ very strongly. High-$N$ values correspond to the regime of oscillations with frequency close to $\omega_0$, see Fig. 2.5, whereas low $N$ values correspond to the frequency of oscillations close to $\Omega_R$.

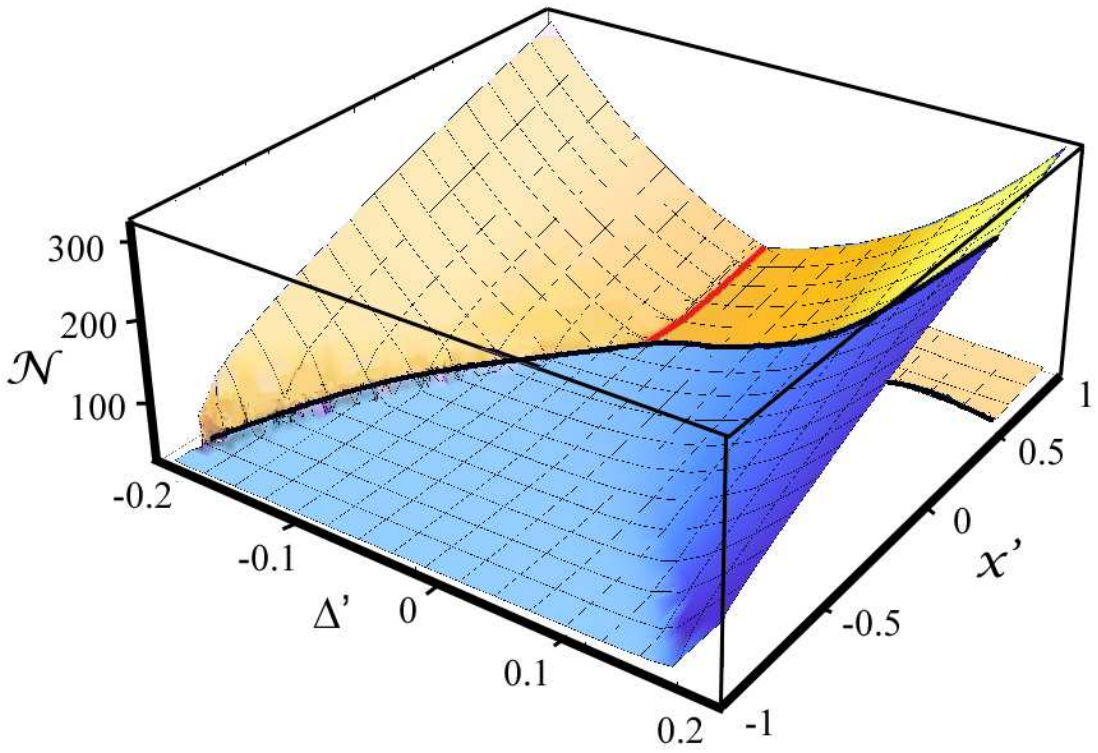


**Figure 2.9**: Excitation level of the oscillator, $\mathcal{N} = 16N\lambda^{2/3}$, where $N$ is the number of vibrational quanta, is plotted from Eq. (2.19) vs dimensionless detuning and dimensionless deviation from the resonance, $x' = \left(\Omega_R - \omega_0\right)/\left(\omega_0\omega_p^2\right)^{1/3}$. The thick black line of bifurcations separates the "inner" domain of parameters (blue domain where bistability is absent) and outer domain (yellow domain where bistability is present). In the outer domain, the ratio of $\mathcal{N}$ values corresponding to the two stable solutions grows rapidly away from the boundary.

At $x' < 0.5$ and to the right from the bifurcation line, there is no bistability. The value of $N$ is low in this domain around $\Delta' = 0$. As $\Delta'$ increases, $N$ grows for both signs of detuning, $\Delta'$. However, for $\Delta' > 0$ (blue detuning), the growth of $N$ is monotonical. At the same time, for $\Delta' < 0$ (red detuning), the bistability sets in at a certain critical $\Delta'$. Upon further increase of $|\Delta'|$, the low-$N$ value does not grow, while the high-$N$ value grows rapidly.

It is instructive to compare the results shown in Fig. 2.9 to the results of Refs. [18, 19], shown if Fig. 2.10. The curves $N(\Delta', \Omega_R)$ were obtained in Refs. [18, 19] by numerical solution of the system of master equations for the density matrix describing both the two-level system and the oscillator. First, there is a qualitative agreement in the shape of the boundary of bistability. In Refs. [18, 19], only the low-$N$ values are plotted. The prime observation made in Refs. [18, 19] was that there is a strong difference between these low-$N$ values for blue and red detunings, namely, for the blue detuning, $N$ is much higher. Our analytical results in Fig. 2.9 agree qualitatively with this observation.

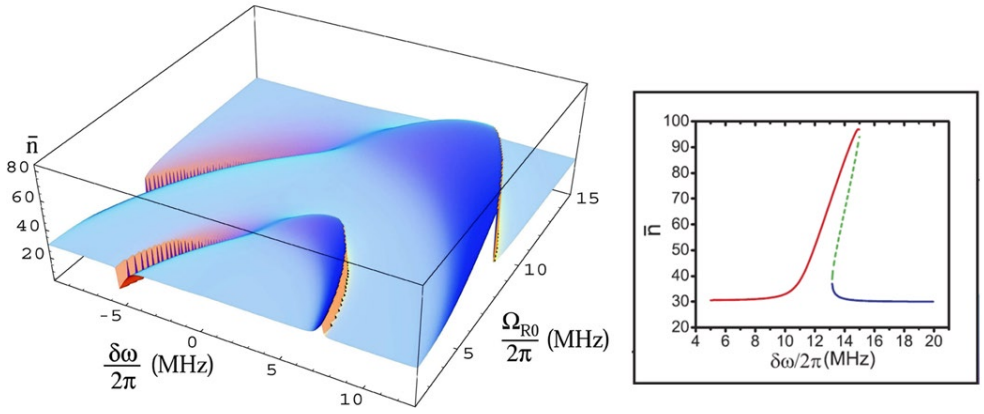


**Figure 2.10**: Results of numerical study of a *quantum* system consisting of a qubit coupled to a harmonic oscillator from [18]. The data are presented for a particular set of parameters of the system, such as coupling strength, spontaneous emission rate, level spacing of the qubit, and the friction in the oscillator. Only the inner curve, corresponding to a one-photon resonance, should be compared to Fig. 2.9. In the domain of bistability, the number of the oscillator quanta shown corresponds to the lower stable state. Compared to results in Fig. 2.9, we can see a similar shape in the bifurcation line. Note also that, similarly to Fig. 2.9, the $N$-values for positive detuning are much higher than for negative detuning.

## 2.6 Concluding remarks

The frequency $\Omega_R$ of the Rabi oscillations is proportional to the square root of the excitation power. This linearity has been demonstrated in many experiments. Even when Rabi oscillations are damped, the dependence $s(\Omega_R)$ can be extracted from the position of maximum in the Fourier transform [24] of the signal $w(t)$. We predict that, for a two-level system coupled to a vibrational mode, the position of maximum of the Fourier transform will deviate from the linear behavior near the resonance $\Omega_R = \omega_0$. Both to the left and to the right from the resonance the position of maxim corresponds to $s < \Omega_R$. The relative width of the resonant regions depends on the coupling $\lambda$ to the vibrational mode as $\lambda^{4/3}$. We also predict that, in the vicinity of the resonance, the dependence $s(\Omega_R)$ exhibits a hysteretic behavior with two stable values of $s$ corresponding to two stable regimes of the Rabi oscillations.

The underlying physics of the Rabi-vibronic resonance is the following. Without coupling, population inversion $w$ and displacement $X$ satisfy the harmonic oscillator equations with frequencies $\Omega_R$ and $\omega_0$, respectively. With coupling, the two-level system acts as a driving force $\propto w$ on the oscillator, while the back action of the oscillator on $w$ is peculiar. The structure of back-action force is $wX^2$, as can be seen from Eqs. (2.8) and (2.9). This structure implies that back action is of a parametrical type, i.e., $X^2$ adds to $\Omega_R^2$. Thus, at $\Omega_R \approx \omega_0$, it appears that $\Omega_R$ is modulated with frequency $\approx 2\Omega_R$. This, however, does not lead to a parametric instability. Instead, the oscillator motion gets synchronized with the Rabi oscillations. In this regard, there is a certain analogy to the synchronization of the Rabi oscillations to a sequence of pulses [25] applied to the detector with a repetition period chosen to be $2\pi/\Omega_R$.

As it was pointed out in the Introduction, the situation when a two-level system undergoing the Rabi oscillations is coupled to the oscillator is actively studied in connection to the circuit QED [14]. The most common situation in circuit QED is when the oscillator frequency $\omega_0$ is tuned to the transition frequency $\omega_{12}$ of the two-level system. Among physical effects predicted for this domain is that two or multiple qubits can get strongly coupled to each other via coupling to a common oscillator, [26, 27]. Rabi-vibronic resonance corresponds to the domain $\omega_0 \ll \omega_{12}$. Still, the effects similar to those discussed in Refs. [26, 27] (see also recent experiments Refs. [28, 29]) will take place under the conditions of the Rabi-vibronic resonance. In particular, we anticipate that Rabi oscillations in two driven two-level systems with $\Omega_R = \omega_0$ coupled to the same oscillator will get synchronized.

As a final remark, classical treatment of the vibrational mode adopted in the present paper does not allow one to capture the quantum jumps [20] between the stable regimes of collective motion of the two-level system coupled to the oscillator. We also did not consider the effect of thermal noise, which leads to the activated switching [30] between the steady regimes even within a classical description of the oscillator.

## 2.7 Appendix

### 2.7.1 Introduction

In the above chapter, we realized that Rabi-vibronic resonance develops when the coupling of electronic level to the vibrational mode is weak. Weakness of the coupling suggests tring to treat it perturbatively, namely, to assume that in zeroth order the oscillations have their "bare" form, $w^{(0)}(t)$, then to search for the correction, $w^{(1)}(t)$, to this form proportional to the coupling strength. The hope is that near the resonance $\Omega_R = \omega_0$, the correction "blows up". It is clear a priori that this program will not work for nondecaying Rabi oscillations, since we demonstrated in the previous chapter that, under the conditions of Rabi-vibronic resonance, the frequency, $s$, of collective motion differs from $\Omega_R$, so that $w^{(0)}(t)$ is not a good zero-order approximation. However, one might hope that, in the presence of friction or spontaneous emission, when $w^{(0)}(t)$ decays with time, so that the frequency $\Omega_R$ is "smeared", the correction $w^{(1)}(t)$ will blow up at the resonance but remain finite and smaller than $w^{(0)}(t)$, so that perturbative treatment remains justified. This is the motivation for why in the following Appendix we calculate $w^{(1)}(t)$ at finite friction in the oscillator and finite spontaneous emission of the two-level system and examine this solution in different limits. The prime outcome is that, while $w^{(1)}(t)$ remains finite at the resonance, the perturbative treatment does not apply within the *entire* time domain. The reason is that condition $w^{(1)}(t) \ll w^{(0)}(t)$ is incompatible with the requirement that the oscillator is classical. Still it offers an accurate description of collective motion during the initial stage of oscillations when $\Omega_R$ gradually evolves into $s$.

### 2.7.2 Perturbative treatment

We search for a solution of optical Bloch Eqs. (2.5)-(2.7), within the lowest order in $X(t)$ in the form $v = v^{(0)} + v^{(1)}$ and $w = w^{(0)} + w^{(1)}$. The zero-order solution, can easily be found using the initial conditions: $X(0)$, $v(0) = 0$ and $u(0) = 0$. From Eq. (2.5), we see that the initial conditions for $v(t)$ and $w(t)$ require that $\dot{w}(0) = 0$. In the limit

$\Omega_R \gg \Gamma$, the function $u(t)$ is zero, while the expressions for $w^{(0)}$ and $v^{(0)}$ read

$$w^{(0)}(t) = -\frac{\Gamma^2}{\Gamma^2 + 2{\Omega_R}^2} - \left(\frac{2\Omega_R^2}{\Gamma^2 + 2\Omega_R^2}\right) e^{-3\Gamma t/4} \cos\Omega_R t \approx -e^{-3\Gamma t/4} \cos\Omega_R t, \tag{2.45}$$

$$v^{(0)}(t) = -\frac{1}{\Omega_R}\left(\dot{w}^{(0)} + \Gamma\big(1 + w^{(0)}\big)\right) \approx \frac{-\dot{w}^{(0)}(t)}{\Omega_R}, \tag{2.46}$$

In the first order, the prime effect of coupling to the oscillator is that $u(t) = u^{(1)}(t)$ becomes nonzero. It can be found from Eq. (2.6), which reads

$$\dot{u}^{(1)} + \frac{\Gamma}{2} u^{(1)} = \mu X(t)\, v^{(0)}(t). \tag{2.47}$$

Using the initial condition $u^{(1)}(0) = 0$, we find

$$u^{(1)}(t) = \mu e^{-\Gamma t/2} \int_0^t dt' e^{\Gamma t'/2} X(t')\, v^{(0)}(t'), \tag{2.48}$$

where $v^{(0)}(t)$ is determined from Eq. (2.46). From Eq. (2.5), we see that $v^{(1)}(t)$ and $w^{(1)}(t)$ are related as

$$v^{(1)}(t) = -\frac{1}{\Omega_R}\left(\dot{w}^{(1)} + \Gamma w^{(1)}\right). \tag{2.49}$$

Substituting this relation into Eq. (2.7), we get the following equation for $w^{(1)}(t)$

$$\ddot{w}^{(1)} + \frac{3\Gamma}{2}\dot{w}^{(1)} + \left({\Omega_R}^2 + \frac{\Gamma^2}{2}\right) w^{(1)} = \mu\Omega_R X(t) u^{(1)}(t). \tag{2.50}$$

We see that the product $X(t)u^{(1)}(t)$ plays the role of a driving force in the damped-harmonic-oscillator equation for $w^{(1)}(t)$. Note that this driving force is *quadratic* in $X(t)$. With initial conditions $w^{(1)}(0) = \dot{w}^{(1)}(0) = 0$, the solution for $w^{(1)}(t)$ reads

$$w^{(1)} = e^{-3\Gamma t/4}\Big[w_c(t)\cos\Omega_R t + w_s(t)\sin\Omega_R t\Big], \tag{2.51}$$

where the functions $w_c(t)$ and $w_s(t)$ are defined as

$$w_c(t) = \mu^2 \int_0^t dt' e^{\Gamma t'/4}\Big[X(t')\sin\Omega_R t'\Big] \int_0^{t'} dt'' e^{-\Gamma t''/4}\Big[X(t'')\sin\Omega_R t''\Big], \tag{2.52}$$

$$w_s(t) = -\mu^2 \int_0^t dt' e^{\Gamma t'/4}\Big[X(t')\cos\Omega_R t'\Big] \int_0^{t'} dt'' e^{-\Gamma t''/4}\Big[X(t'')\sin\Omega_R t''\Big]. \tag{2.53}$$

In Eqs. (2.52) and (2.53), we have substituted the explicit form Eq. (2.48) of $u^{(1)}(t)$. The first term in Eq. (2.51), proportional to the cosine, describes the correction to the amplitude of the Rabi oscillations due to coupling to the oscillator, while the second term, proportional to sine, describes the change of the phase.

The remaining task is to solve the equation, Eq. (2.4), for the oscillator and substitute the found $X(t)$ into Eqs. (2.52) and (2.53). In doing so, one should keep in mind that, in addition to forced oscillations, caused by the r.h.s. of Eq. (2.4), the oscillator also undergoes the free oscillations with frequency $\omega_0$. The relation between the amplitudes of the free and forced oscillations is governed by the initial conditions. As a result, the products $X(t)\cos\Omega_R t$ and $X(t)\sin\Omega_R t$ in the integrands of Eqs. (2.52), (2.53) will contain a slow *nonoscillating* term and a slow term oscillating with frequency $\delta = \Omega_R - \omega_0$.

The integrands of $w_c(t)$ and $w_s(t)$ contain two combinations of the type $X(t)\cos\Omega_R t$. As a result, $w^{(1)}(t)$ will contain a nonoscillating term, terms oscillating with frequency $\delta$, and terms oscillating with frequency $2\delta$. Concerning the magnitude of $w^{(1)}(t)$, note that, away from resonance, $X(t)$ is proportional to $\frac{1}{\delta}$. This leads to $\frac{1}{\delta^2}$ factor in $w^{(1)}(t)$. Less trivial is that two additional integrations over $t'$ and $t''$ in Eqs. (2.52), (2.53) give rise to another factor $\frac{1}{\delta^2}$. So overall, we have $w^{(1)} \propto \frac{1}{\delta^4}$. The physics underlying the additional $\frac{1}{\delta^2}$ factor is the nonlinear feedback exercised by the driven oscillator on the two-level system.

### 2.7.3 Friction-dominated regime, $\Gamma \ll \gamma$

In the limit $\Gamma \ll \gamma$, the r.h.s. of Eq. (2.4) is proportional to $\cos\Omega_R t$. Then the solution is straightforward. It contains an inessential constant term $\mu/(2M\omega_0^2)$ and the oscillating part

$$X(t) = \frac{\mu}{2M\Omega_R(\gamma^2+4\delta^2)}\left[\Big(\gamma\sin\Omega_R t - 2\delta\cos\Omega_R t\Big) - e^{-\gamma t/2}\Big(\gamma\sin\omega_0 t - 2\delta\cos\omega_0 t\Big)\right]. \tag{2.54}$$

In deriving Eq. (2.54), we used the fact that $\gamma$, $\delta \ll \Omega_R$ and $\omega_0 \approx \Omega_R$. We also neglected the friction-induced correction, $\gamma^2/(8\omega_0)$, to $\omega_0$. In the limit $\Gamma \ll \gamma$, the relaxation exponents in the integrand of Eq. (2.52) can be neglected. After that, the double integral simply reduces to $1/2[\int_0^t dt' X(t')\sin\Omega_R t']^2$. Performing integration and keeping only resonant terms we obtain,

$$w_c(t) = \frac{\omega_p^2\Omega_R^2}{2(\gamma^2+4\delta^2)^2}\left[\frac{\gamma t}{2} - \left(\frac{4\gamma\delta}{\gamma^2+4\delta^2}\right)e^{-\gamma t/2}\sin\delta t - \left(\frac{\gamma^2-4\delta^2}{\gamma^2+4\delta^2}\right)\left(1-e^{-\gamma t/2}\cos\delta t\right)\right]^2. \tag{2.55}$$

Equation (2.55) coincides with Eq. (2.39) of the main text. In the main text, it was used to determine the number of oscillation periods, $m'$, before collective motion sets in. As we expected, $w_c(t)$, carries the "knowledge" about the Rabi-vibronic resonance, via the resonant prefactor proportional to $(\gamma^2+4\delta^2)^{-2}$, where $\delta$ is the deviation from

resonance. However, the main message sent by Eq. (2.55) is that its growth with time is not contained by friction or detuning, as one could hope. For times exceeding the time, $\frac{1}{\gamma}$, of oscillator damping, the correction $w_c(t)$ *grows* with time quadratically. Note also that this growth is preceded by several oscillations, as illustrated in Fig. 2.11. More specifically, for $\gamma t \ll 1$, the magnitude of $w_c(t)$ increases as $\omega_p^2 \Omega_R^2 t^4$, for $\delta = 0$, while for longer times, $\gamma t \gg 1$, the term $\gamma t/2$ dominates and the growth of $w_c(t)$ is $\propto \frac{1}{\gamma}(\omega_p \Omega_R t)^2$. However, perturbation theory no longer applies, after time $\frac{1}{\gamma}$, as was discussed in Section 1.4.3.

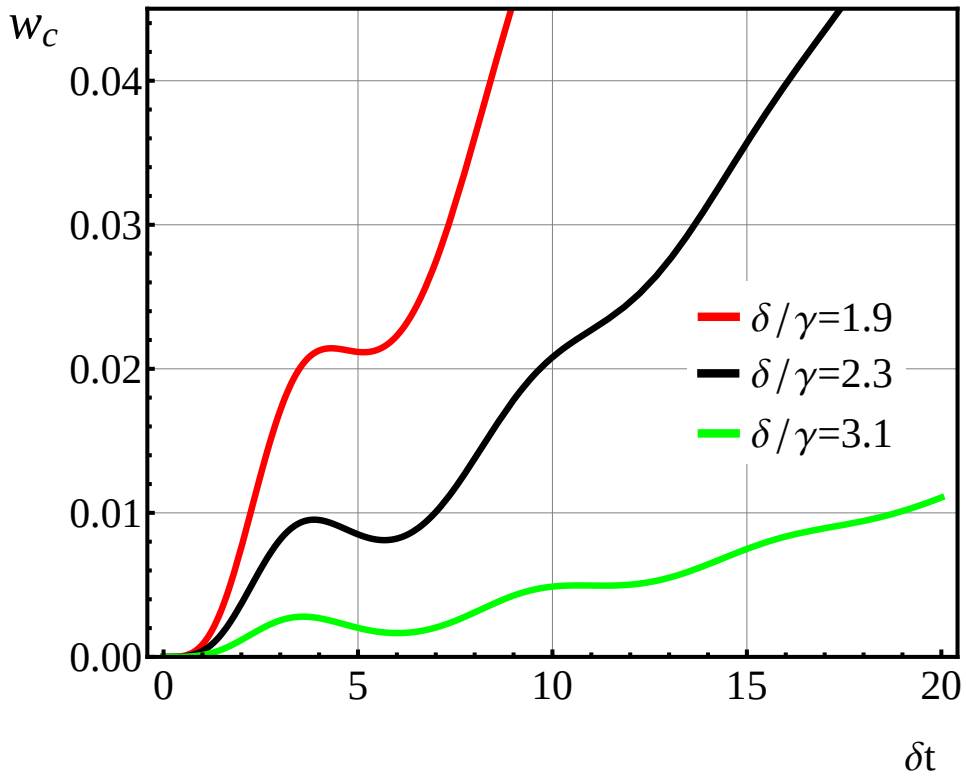


**Figure 2.11**: Coupling-induced modification of the amplitude of the Rabi oscillations in the friction-dominated regime versus the dimensionless time, $\delta t$, is plotted from Eq. (2.55), in the units of $\omega_p^2 \Omega_R^2/(2\gamma^4)$, for three dimensionless detunings from resonance; $\frac{\delta}{\gamma} = 1.9$ (red); $\frac{\delta}{\gamma} = 2.3$ (black); $\frac{\delta}{\gamma} = 3.1$ (green). We see that for small detuning, $\delta/\gamma = 1.9$, $w_c(t)$ *grows* rapidly, meaning that for small, detuning perturbation theory only applies for very short times. For large detuning, $\delta/\gamma = 3.1$, when the growth is much slower, $w_c(t)$ exhibits several oscillations, while it is still small.

### 2.7.4 Relaxation-dominated regime, $\gamma \ll \Gamma$

In this section, we consider decoherence of the excited state, assuming no detuning. In this regime, the damped oscillator, Eq. (2.4), is a driven harmonic oscillator, where driving force, $w^{(0)}$, is described by Eq. (2.45). The solution of $X(t)$ can easily be found as

$$X(t) = \frac{4\mu}{M\omega_0\big(16\delta^2+9\Gamma^2\big)}\left[\left(\frac{3\Gamma}{4}\sin\omega_0 t+\delta\cos\omega_0 t\right)-e^{-3\Gamma t/4}\left(\frac{3\Gamma}{4}\sin\Omega_R t+\delta\cos\Omega_R t\right)\right], \tag{2.56}$$

where the static displacement causes a small correction $\mu/(2M\Omega_R^2)$ to $X(t)$ and it is neglected. Comparing Eqs. (2.56) and (2.54), it can be seen that $X(t)$ assumes the same form as in the previous section with the substitution $\Gamma = 2\gamma/3$. Recall that the solution of $w^{(1)}(t)$ is found by Eqs. (2.52), (2.53). Returning, we see that both equations contain the integrand $e^{-\Gamma t''/4}X(t'')\sin\Omega_R t''$. Employing the RWA when expanding the product $X(t''), \sin\Omega_R t''$, gives

$$X(t'')\sin\Omega_R t'' = \frac{2\mu}{M\omega_0\big(16\delta^2+9\Gamma^2\big)}\left[\delta\sin\delta t'+\frac{3\Gamma}{4}\left(\cos\delta t'-e^{-3\Gamma t'/4}\right)\right]. \tag{2.57}$$

Concentrating on the first integral over $t''$ in $w_c(t)$, we multiply Eq. (2.57) by $e^{-\Gamma t''/4}$ and integrate, noting that, $Y(t') = \int_0^{t'} dt'' e^{-\Gamma t''/4}X(t'')\sin\Omega_R t''$,

$$\begin{aligned} Y(t') &= \frac{2\mu}{M\omega_0\big(9\Gamma^2+16\delta^2\big)}\left[\left(\frac{8\delta\Gamma}{\Gamma^2+16\delta^2}\right)e^{\Gamma t'/4}\sin\delta t'\right. \\ &+ \left.\left(\frac{3\Gamma^2+16\delta^2}{\Gamma^2+16\delta^2}\right)\left(1-e^{-\Gamma t'/4}\cos\delta t'\right)+\frac{3}{4}\Big(e^{-\Gamma t'}-1\Big)\right]. \end{aligned} \tag{2.58}$$

Although the cosine and sine-terms in $Y(t')$ grow exponentially, $w^{(1)}(t)$ will decay exponentially due to damping factor, $e^{-3\Gamma t/4}$, multiplying $w_c(t)$ and $w_s(t)$. The second integral over $t'$, in $w_c(t)$, Eq.(2.52), contains the integrand $X(t')e^{\Gamma t'/4}\sin\Omega_R t' Y(t')$. Introducing dimensionless variables, $z = \delta/\Gamma$ and $\tau = \delta t$, we covert the product of trigonometrical functions in the integrand into a sum, and then evaluate $w_c(t)$

$$\begin{aligned} w_c(t) &= -\frac{16\omega_p^2\Omega_R^2}{\Gamma^4(16z^2+1)(16z^2+9)}\left[\frac{\tau}{8z}-\left(\frac{4z}{16z^2+1}\right)e^{\tau/4z}\sin\tau+\frac{1}{4}\left(\frac{16z^2-3}{16z^2+1}\right)e^{\tau/4z}\cos\tau\right. \\ &- \left(\frac{12z}{16z^2+9}\right)e^{-3\tau/4z}\sin\tau+\frac{3}{4}\left(\frac{16z^2+5}{16z^2+9}\right)e^{-3\tau/4z}\cos\tau+\frac{1}{2}\left(\frac{16z^2-3}{16z^2+9}\right)\sin^2\tau \\ &+ \left.\frac{1}{16z}\left(\frac{80z^2+9}{16z^2+9}\right)\sin 2\tau - h(\tau,z)\right], \end{aligned}$$

(2.59)

where

$$h(\tau,z)=\frac{1}{4}\left[\frac{(16z^2-3)(16z^2+9)}{16z^2+1}\right]+\frac{3}{8}\left(\frac{16z^2+9}{16z^2+1}\right)e^{-\tau/2z}+\frac{3}{8}e^{-3\tau/2z}. \tag{2.60}$$

Obviously, the first three terms in the square brackets of Eq. (2.59) dominate for all times. For small times, $t \ll \frac{\Gamma}{4}$, $w_c(\tau)$ grows linearly, as described by the term $\tau/8z$, while for times, $t > \frac{\Gamma}{4}$, the second and third terms dominate, and $w_c(t)$ becomes exponential. On the other hand, the correction $w^{(1)}(t)$ is proportional to $e^{-3\tau/4z}w_c(\tau)$ and does not grow exponentially. For this reason, we plot $e^{-3\tau/4z}w_c(\tau)$ in Fig. 2.12. We see that for small $z = 0.03$, the amplitude of $e^{-3\tau/4z}w_c(\tau)$ has a maximum height. With increasing detuning further $z = 0.1$, the initial amplitude of $e^{-3\tau/4z}w_c(\tau)$ decreases. Upon further increasing $z$, the function $e^{-3\tau/4z}w_c(\tau)$ simply approaches zero.

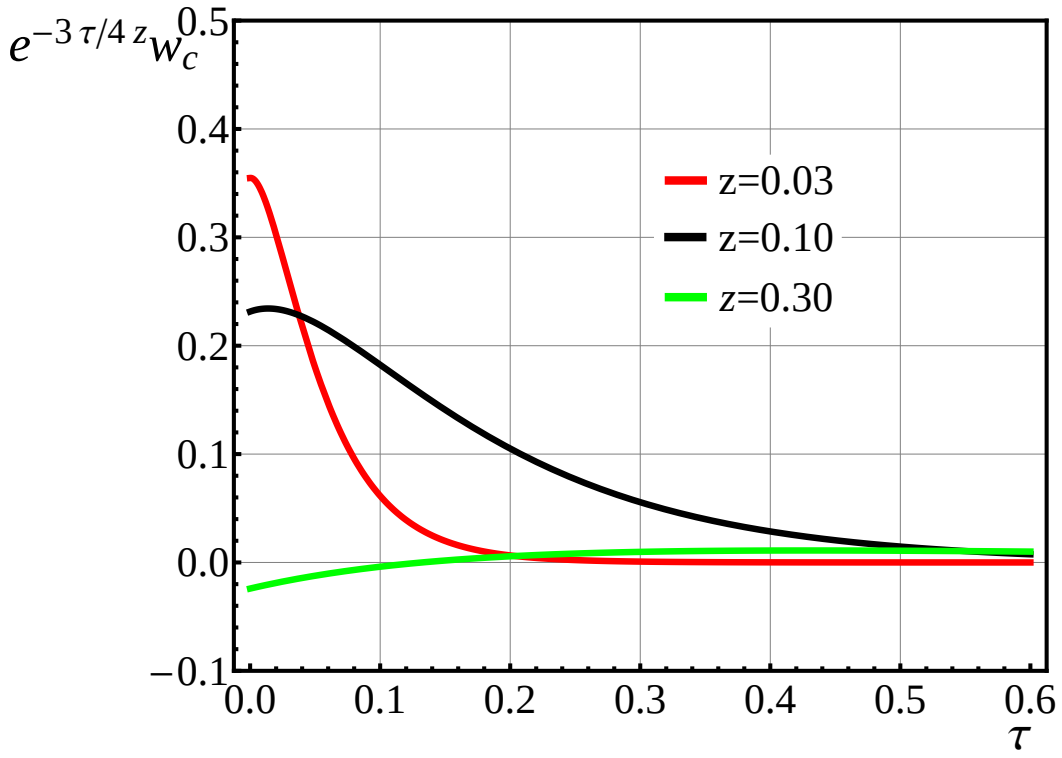


**Figure 2.12**: Coupling-induced modification of the amplitude of the Rabi oscillations in the relaxation-dominated regime is plotted from the function $e^{-3\tau/4z}w_c(\tau)$, Eq. (2.59), in the units of $16\omega_p^2\Omega_R^2/\Gamma^4$ for different dimensionless detunings $z = 0.03$ (red), $z = 0.1$ (black), $z = 0.3$ (green). With increasing the detuning, the correction, $e^{-3\tau/4z}w_c(\tau)$, approaches zero.

Overall, as in the friction-dominated regime, the prefactor in Eq. (2.59) exhibits resonant behavior as a function of dimensionless deviation $z = \delta/\Gamma$ from the Rabi-vibronic resonance. Unlike the friction-dominated regime, the correction $e^{-3\tau/4z}w_c(\tau)$ remains finite at all times. However, it falls off with time slower than the zero-order result $w^{(0)}(t)$, and, thus, the perturbation treatment fails at large times.

### 2.7.5 Analysis

As was stated in the Introduction, perturbation theory does not apply for the *entire* domain. The time domain where perturbation theory applies is where both the assumptions made coincide. First consider the assumption that the oscillator is classical. This requires that the kinetic energy be greater than $\hbar\omega_0$,

$$\frac{1}{2}M\dot{X}^2 \approx \frac{\omega_0^2 M}{2}X^2(t) \gg \hbar\omega_0. \tag{2.61}$$

In the friction-dominated regime, this condition can be written as

$$\omega_p\left(\frac{\omega_0^2}{\gamma^2+4\delta^2}\right) \gg \omega_0, \tag{2.62}$$

Condition, Eq. (2.62), has the same form in the relaxation-dominated regime, where one should replace $\gamma$ by $\Gamma$. On the other hand, as it follows from Eq. (2.55), the condition that $w^{(1)}(t) \ll 1$ at all times smaller than $1/\gamma$ reads

$$\frac{\omega_p^2\Omega_R^2}{(\gamma^2+4\delta^2)^2} \ll 1. \tag{2.63}$$

We see that these two conditions are incompatible at all $\delta$-values and $\gamma$-values in both regimes.

## 2.8 References


[1] I. I. Rabi, Phys. Rev. **51**, 652 (1937).

[2] F. Bloch, Phys. Rev. **70**, 460 (1946).

[3] F. Bloch and A. Siegert, Phys. Rev. **57**, 522 (1940).

[4] J. H. Shirley, Phys. Rev. 138, **979**, (1965).

[5] E. T. Jaynes and F. W. Cummings, Proc. IEEE **51**, 89 (1963).

[6] L. Y. Gorelik, A. Isacsson, M. V. Voinova, B. Kasemo, R. I. Shekhter, and M. Jonson, Phys. Rev. Lett. **80**, 4526 (1998).

[7] Ya. M. Blanter, O. Usmani, and Yu. V. Nazarov, Phys. Rev. Lett. **93**, 136802 (2004).

[8] C. Galland and A. Imamoglu, Phys. Rev. Lett. **101**, 157404 (2008).

[9] C. Galland, A. Högele, H. E. Türeci, and A. Imamoglu, Phys. Rev. Lett. **101**, 067402 (2008).

[10] A. K. Hüttel, G. A. Steele, B. Witkamp, M. Poot, L. P. Kouwenhoven, and H. S. J. van der Zant, Nano Lett. **9**, 2547 (2009).

[11] J.-J. Li, W. He, and K.-D. Zhu, Phys. Rev. B **83**, 115445 (2011).

[12] R. B. Capaz, C. D. Spataru, S. Ismail-Beigi, and S. G. Louie, Phys. Rev. B **74**, 121401 (2006).

[13] P. Avouris, M. Freitag, and V. Perebeinos, Nat. Photon. **2**, 341 (2008).

[14] See J. Schoelkopf and S. M. Girvin, Nature (London) **451**, 664 (2008), and references therein.

[15] E. Il'ichev, N. Oukhanski, A. Izmalkov, T. Wagner, M. Grajcar, H. G. Meyer, A. Y. Smirnov, A. Maassen van den Brink, M. H. S. Amin, and A. M. Zagoskin, Phys. Rev. Lett. **91**, 097906 (2003).

[16] V. I. Shnyrkov, D. Born, A. A. Soroka, and W. Krech, Phys. Rev. B **79**, 184522 (2009).

[17] A. Yu. Smirnov, Phys. Rev. B **68**, 134514 (2003).

[18] J. Hauss, A. Fedorov, C. Hutter, A. Shnirman, and G. Schön, Phys. Rev. Lett. **100**, 37003 (2008).

[19] S. André, V. Brosco, M. Marthaler, A. Shnirman, and G. Schön, New J. Phys. **10**, 095018 (2008).

[20] O. V. Zhirov and D. L. Shepelyansky, Phys. Rev. Lett. **100**, 014101 (2008).

[21] Ya. S. Greenberg, E. Il'ichev, and A. Izmalkov, Europhys. Lett. **72**, 880 (2005).

[22] Ya. S. Greenberg, Phys. Rev. B **76**, 104520 (2007), Ya. S. Greenberg, E. Il'ichev, and F. Nori, *ibid* **80**, 214423 (2009).

[23] H. C. Torrey, Phys. Rev. **76**, 1059 (1949).

[24] D. R. McCamey, K. J. van Schooten, W. J. Baker, S.-Y. Lee, S.-Y. Paik, J. M. Lupton, and C. Boehme, Phys. Rev. Lett. **104**, 017601 (2010).

[25] A. N. Korotkov, Phys. Rev. B **83**, 041406 (2011).

[26] J. Majer, J. M. Chow, J. M. Gambetta, J. Koch, B. R. Johnson, J. A. Schreier, L. Frunzio, D. I. Schuster, A. A. Houck, A. Wallraff, A. Blais, M. H. Devoret, S. M. Girvin, R. J. Schoelkopf, Nature (London) **449**, 443 (2007).

[27] M. Dukalski and Ya. M. Blanter, Phys. Rev. A **82**, 052330 (2010).

[28] E. Abe, H. Wu, A. Ardavan, J. J. L. Morton, Appl. Phys. Lett. **98**, 251108 (2011).

[29] Y. Kubo, F. R. Ong, P. Bertet, D. Vion, V. Jacques, D. Zheng, A. Dréau, J.-F. Roch, A. Auffeves, F. Jelezko, J. Wrachtrup, M. F. Barthe, P. Bergonzo, and D. Esteve, Phys. Rev. Lett. **105**, 140502 (2010).

[30] M. I. Dykman and M. A. Krivoglaz, Zh. Eksp. Teor. Fiz. **77**, 60 (1979) [Sov. Phys. -JETP **50**, 30 (1979)].

# CHAPTER 3

# MANY-BODY ASPECTS OF RABI OSCILLATIONS IN A QUANTUM DOT MOLECULE

## 3.1 Introduction

An obvious reason why optical properties of semiconductor quantum dots are intensively studied both theoretically and experimentally is that quantum dots are considered to be promising candidates for the basic device unit of quantum information processing. In plain words, a dot with one electron and hole level can be viewed as a qubit, in the sense that the presence of an exciton in a dot can be viewed as an "on" state of the qubit, while absence of an exciton can be viewed as an "off" state. Compared to other candidates for the qubits, such as nuclear spins [1] or electron spins [2], a qubit based on an exciton in a semiconductor quantum dot can operate at a much higher (terahertz) rate. This is because the resonant frequency of the exciton lies within the optical range. First, the principal requirement for exciton(s) contained within a quantum dot to serve as an efficient quantum bit is that they have to possess a long coherence time. Second, they should allow coherent optical manipulation, the simplest example being coupling and entangling of quantum states in a pair of dots. In simple terms, coherent optical manipulation in a pair of two quantum dots relies on the fact that creation of an exciton in one dot affects the resonant energy of the other. As a result, the quantum state of one dot controls the outcome of measurements on another dot. This correlation, plus the fact that exciton(s) in both dots are coherent and are characterized by a single many-body function, was argued [3] to be sufficient for two dots to operate as a quantum gate.

A natural characteristic of the degree of coherence of an optical excitation in a dot is its ability to exhibit Rabi oscillations. In fact, Rabi oscillations of an exciton in a single dot is what is meant by coherent control. In this regard, experimental demonstrations of

Rabi oscillations in a single dot reported in Refs. [4, 5] was vital. In the language of the quantum computation community, observation of Rabi oscillations in a single quantum dot constitutes proof of the exciton qubit rotation.

Equally important was a decade-old experimental demonstration [6] that excited excitons in two close-spaced quantum dots can be efficiently coupled to each other. The evidence of coupling was inferred from measuring the evolution of the photoluminescence emission lines as a function of the interdot separation, shown if Fig. 3.1. In a later paper, Ref. [7], it was demonstrated that this coupling can be facilitated by applying an external electric field which aligns the single particle levels in the neighboring dots.

In early experiments [4, 5] on coherent control, Rabi oscillations were registered either by means of transient nonlinear optical spectroscopy [4] performed on a single dot, or by excitation of a dot by a sequence of pulses and recording photoluminescence as a function of temporal pulse delay between two pulses [5]. A remarkable progress in registration of coherence of excitations in a single quantum dot was reported in Ref. [8]. Instead of optical registration of the Rabi oscillations in Refs. [4, 5], the authors had put forward

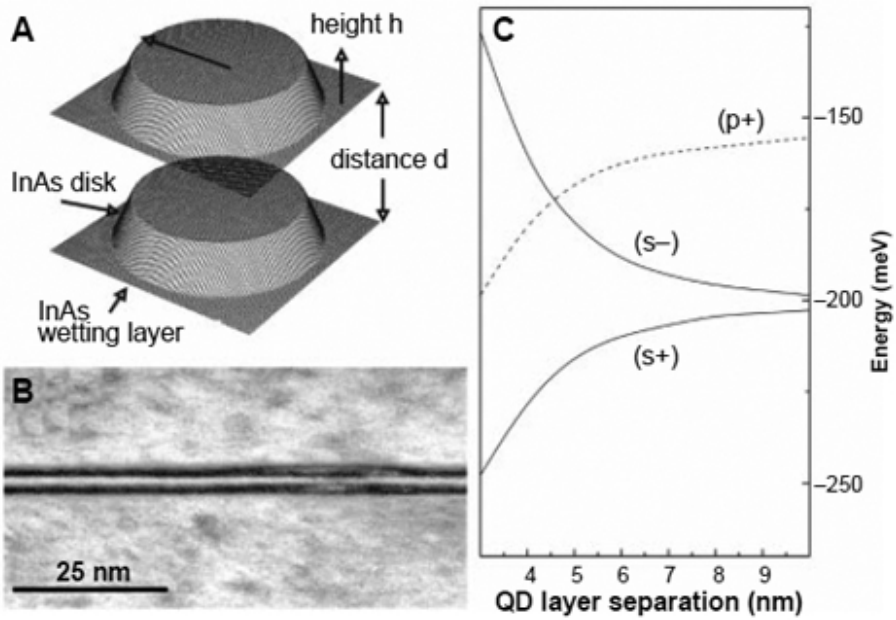


**Figure 3.1**: Quantum dot molecule in the experiment Refs. [6].(A) The assumed shape of the two vertically aligned quantum dots. (B) Transmission electron microscopy (TEM) image of the two layers of quantum dots. (C) Assuming the shape shown in (A), the authors numerically calculate how the symmetric-antisymmetric splitting of the levels depends on the vertical separation of the dots.

an elegant idea: in the course of the Rabi oscillations, the exciton population of a dot changes with time as $\cos \Omega_R t$, where $\Omega_R$ is the Rabi frequency. If the duration of the excitation pulse is $\pi/\Omega_R$ (a $\pi$-pulse), an exciton is present in the dot with probability 1. Then electric field applied to the dot will tear the electron and hole apart, as illustrated in Fig. 3.2, and both electron and hole will contribute to the current in the circuit. As a result, after many pulses, the measured current, $I$, will be simply equal to $fe$, where $f$ is the frequency of the repetition of $\pi$-pulses. Rabi oscillations manifest themselves in the dependence of the current on the amplitude, $A$, (in the frequency units) of an excitation pulse $I = ef \cos^2 \pi A/\Omega_R$. If $A$ is equal to $n\Omega_R$, where $n$ is an integer, then the current is maximal. See Fig. 3.2d. If $A = (n + \frac{1}{2})\Omega_R$, the current is zero, since an exciton is not excited during the pulse duration. With the help of this novel technique, the authors of Ref. [8] were able to probe Rabi oscillations electrically in a remarkably *weakly disturbing* fashion. In all present-day experiments, the quantum dots used were self-assembled. They emerged in the course of interruption of molecular-beam growth of GaAs followed by growing of several layers of InGaAs [9]. The strain caused by lattice mismatch of two materials results in formation of a layer lens-shaped InGaAs dots. Repetition of this interruption yields double layers of these quantum dots used in experiments on double dots.

Pioneering experimental papers [4, 5, 3, 7, 8] were followed by a stream of subsequent studies. We cannot quote all of them. The most prominent advances [10, 12, 13, 14, 15, 16, 17, 18, 19, 20, 21] can be divided into two groups. The first group of papers, Refs. [10, 11, 12, 13, 14, 15, 16], reported the measurements of characteristics of excitons in two coupled dots (quantum dot molecule) by means of photoluminescence. Quantum dot molecules are realized experimentally by extending the self-assembly techniques of Ref. [9] to include strained layers. Then InGaAs dots turn out to grow "one above the other", as illustrated in Fig. 3.1a. Thus, two vertically-aligned dots serve as a quantum dot molecule. In the second group, Refs. [11, 17, 18, 19, 20, 21] studied the quantum dynamics of an exciton in a single dot driven by excitation pulses into the regime of Rabi oscillations. One of the techniques to register Rabi oscillations optically is illustrated in Fig. 3.3 and uses the resonant pulses initiating Rabi oscillations between the ground and the first excited state of an electron in the dot. In the course of these oscillations, the electron relaxes nonradiatively to its excitonic ground state. Then the photoluminescence from this state is measured as a function of pulse duration and laser power. Since the probability that,

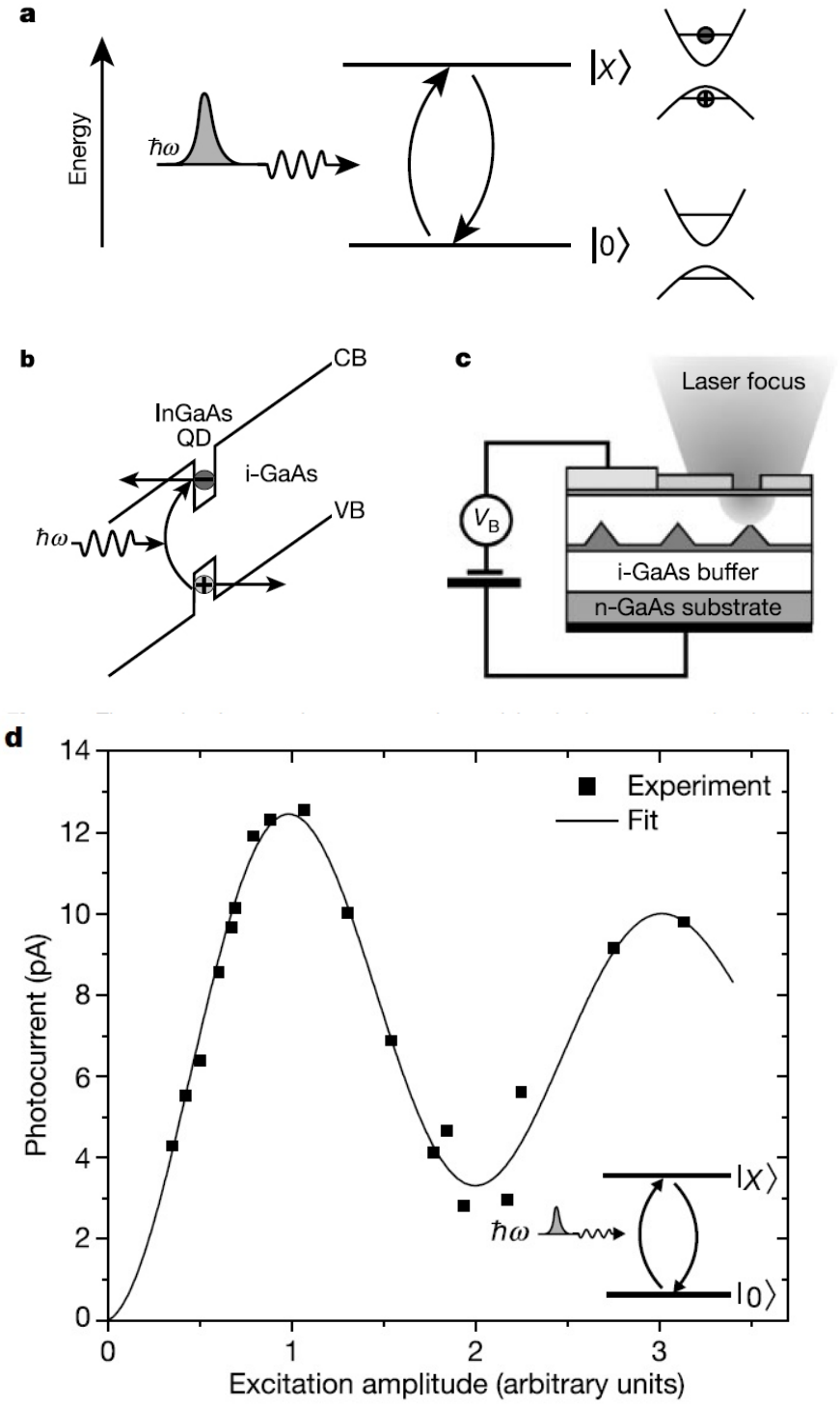


**Figure 3.2**: A schematic illustration of the electrical detection of Rabi oscillations is shown from Ref. [8]. (a) Two level system, an excition in a quantum dot. (b) An applied electric field bends the energy profile of the two-level system, allowing both the electron and hole to tunnel out and contribute to the current. (c) Experimental setup to selectively excite a single dot. (d) The measured photocurrent; the fact that the period of oscillations of the measured photocurrent is a function of excitation *amplitude* proves they are able to measure Rabi oscillations electrically.

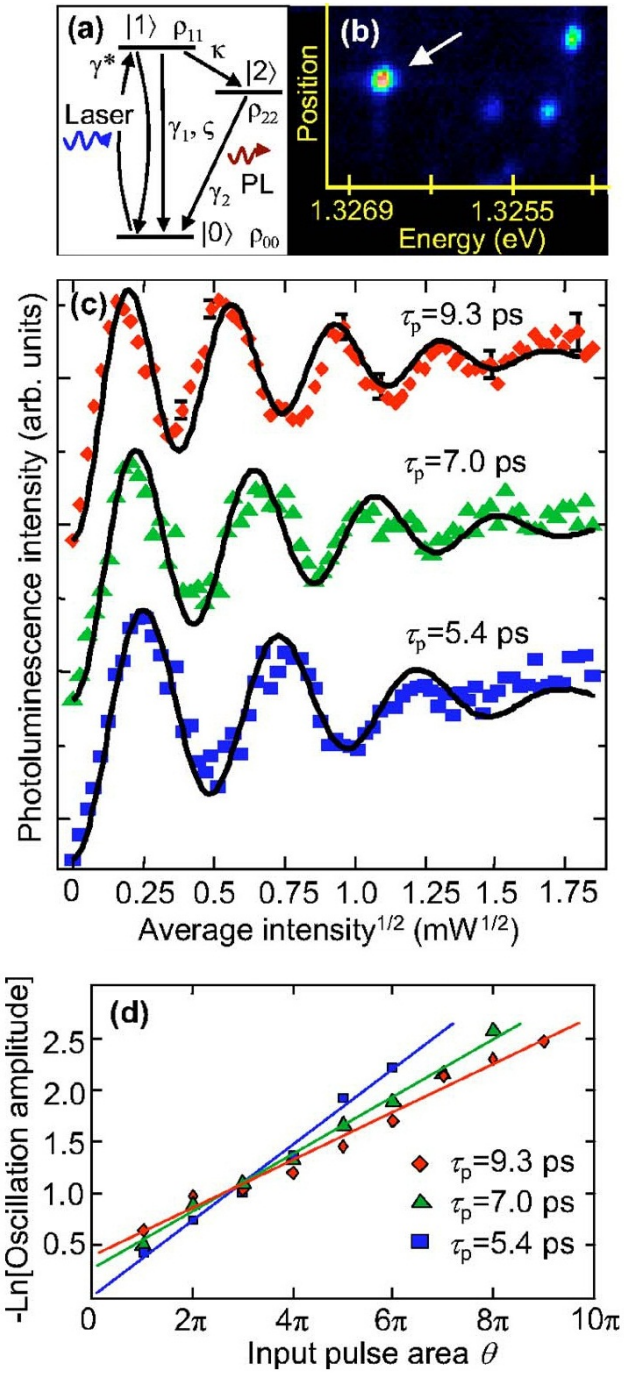


**Figure 3.3**: Optical detection of Rabi oscillations is shown from Ref. [11]. (a) Optical detection of Rabi oscillations requires the third level. (b) Image of a quantum dot shows it is well isolated from other quantum dots. (c) Intensity of the transition $|2> \rightarrow |0>$ versus the excitation amplitude for a given pulse duration, $\tau_p$. Oscillating character, photoluminescence, is due to the fact that for a given pulse duration, it can contain either integer or half-integer Rabi cycles depending on the amplitude. (d) Illustration of the qualitative tendency of damping of the oscillations for different pulse widths as a function of input pulse area.

after the pulse, the electron resides in the first excited state is a periodic function of both, the luminescence signal exhibits Rabi oscillations, as illustrated in Fig. 3.3.

The most recent progress in the field is the experimental demonstration [22] of the Rabi oscillations of *two* excitons in a quantum dot molecule. The oscillations were detected using the pump-probe technique.

The above brief review motivates the research reported in the present chapter. We will study the exciton Rabi oscillations in the system of two tunnel-coupled quantum dots with account of interaction-induced correlation between electron and hole.

As we consider two quantum dots, the following new physical effects come into play: *(a)* due to a finite transparency of barriers, separating the dots, an electron photoexcited, say, in the left dot can, after some time, be found in the right dot. The same applies to the hole. *(b)* the photo-excited electron and hole in the dot attract each other. In an optical experiment, the electron and hole are created simultaneously. The major consequence of this intradot attraction of electron and hole is that, as a result of this attraction, the dynamics of the exciton acquires a *correlated* character. The prime objective of the present chapter is to trace how this correlation manifests itself in the shape of the Rabi oscillations, which arise when the two-dot system is driven by intense resonant light. We will show that the shape of the Rabi oscillations is strongly affected by the interaction effects.

Previous theoretical studies [24, 25, 26] were conducted by solving the system of equations for the density matrix numerically, and could not reveal the effect of interaction on the Rabi oscillations in the quantum dot molecule systematically.

## 3.2 Correlated dynamics of a photoexcited exciton in two coupled dots

The system being considered is depicted in Fig. 3.4. It consists of two coupled quantum dots (QDs) each containing one electron and one hole levels. Possible one-exciton states of the system are labeled $a_1$, $a_2$, $b_1$, and $b_2$, where $a_1$ corresponds to an exciton in the left QD, $a_2$ corresponds to an exciton in the right QD, while $b_1$ and $b_2$ correspond to two possible indirect exciton states.

Before including interactions and studying Rabi oscillations in the system, we will consider the simplest auxiliary problem: suppose that at time $t = 0$ an exciton is excited in the left QD. What is the exciton evolution with time? This evolution is due to tunneling of carriers between the dots. We will also assume that no electric field is applied, so that,

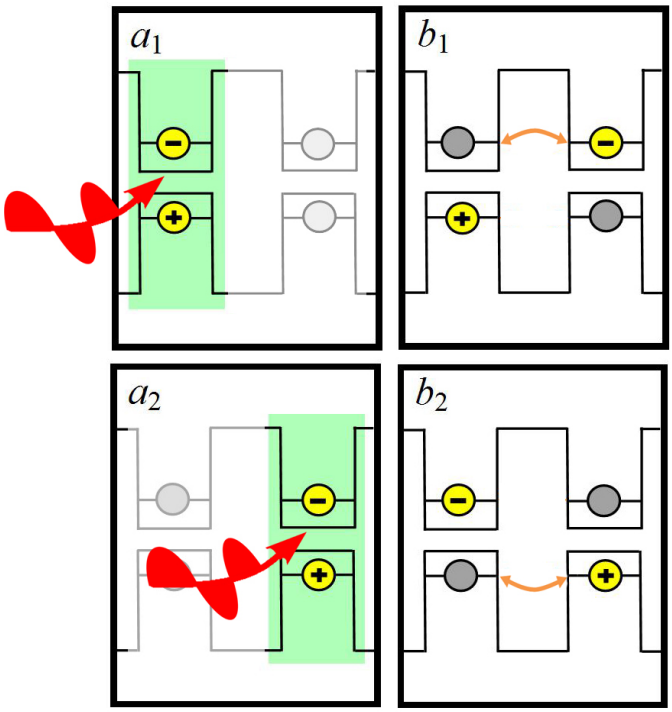


**Figure 3.4**: A schematic illustration of single-exciton states in a quantum dot molecule. A resonant light shone on the molecule can create a direct exciton in either dot (states $a_1$, $a_2$). Due to tunneling, the exciton dynamics involves indirect excitons (states $b_1$, $b_2$). Note that the initial vacuum state, $c$, is not shown.

without tunneling, electron and hole levels in the dots are perfectly aligned. Denote with $\Omega_e$ and $\Omega_h$ the tunnel splittings of the electron and hole levels, respectively. Exciton dynamics are described by 4 probabilities $|a_1(t)|^2$, $|a_2(t)|^2$, $|b_1(t)|^2$, and $|b_2(t)|^2$, where $a_1(t)$, $a_2(t)$, $b_1(t)$, $b_2(t)$ are the amplitudes to find the exciton in the states $a_1$, $a_2$, $b_1$, and $b_2$ after time $t$, respectively. The probabilities are related by the normalization condition

$$|a_1(t)|^2 + |a_2(t)|^2 + |b_1(t)|^2 + |b_2(t)|^2 = 1. \tag{3.1}$$

Without electron-hole interactions, the dynamics reduce to independent beatings of electron and hole between the dots, so that

$$\begin{aligned} |a_1(t)|^2 &= \mathcal{N}_e(t)\mathcal{N}_h(t), & |b_1(t)|^2 &= \mathcal{N}_e(t)\Big(1-\mathcal{N}_h(t)\Big), \\ |a_2(t)|^2 &= \Big(1-\mathcal{N}_e(t)\Big)\Big(1-\mathcal{N}_h(t)\Big), & |b_2(t)|^2 &= \Big(1-\mathcal{N}_e(t)\Big)\mathcal{N}_h(t), \end{aligned} \tag{3.2}$$

where $\mathcal{N}_e(t) = \cos^2 \Omega_e t$ and $\mathcal{N}_h(t) = \cos^2 \Omega_h t$. Note that, with regard to observables, $|a_1(t)|^2$ describes the luminescence from QD1, while $|a_2(t)|^2$ describes the luminescence from QD2.

As a next step, we incorporate electron-hole interaction in the simplest form. Namely, we assume that, at time moments when electron and hole are located in the same dot, they attract each other with Coulomb energy, $U$.

Now, in order to find the time evolution of an exciton, one has to solve the Schrödinger equation

$$i\frac{\partial}{\partial t}\begin{pmatrix} a_1 \\ b_1 \\ b_2 \\ a_2 \end{pmatrix} = \hat{H}\begin{pmatrix} a_1 \\ b_1 \\ b_2 \\ a_2 \end{pmatrix}, \tag{3.3}$$

for the four-component wave function $(a_1(t), b_1(t), b_2(t), a_2(t))$. In Eq. (3.3), we have set $\hbar = 1$. In the matrix representation the Hamiltonian, $\hat{H}$, has the form

$$\hat{H} = \begin{pmatrix} U+\omega_{10} & \Omega_e & \Omega_h & 0 \\ \Omega_e & \omega_{10} & 0 & \Omega_h \\ \Omega_h & 0 & \omega_{10} & \Omega_e \\ 0 & \Omega_h & \Omega_e & U+\omega_{10} \end{pmatrix}, \tag{3.4}$$

where the interaction $U$ is incorporated into the energies of the states $a_1$ and $a_2$.

To get the time evolution of the system, we will now solve Eqs. (3.3) and (3.4).

### 3.2.1 Eigenvalues and eigenvectors

A standard way to find the time evolution of the exciton is to find the eigenvalues of the Hamiltonian Eq. (3.4) and choose the linear combination of the eigenvectors satisfying the initial conditions. The form of the eigenvalues, $\hat{H}\Psi_i = (\zeta_i + \omega_{01})\Psi_i$, is quite simple

$$\begin{aligned} \zeta_{1,2} &= \frac{U}{2} \pm \frac{1}{2}\Big[U^2 + 4(\Omega_e + \Omega_h)^2\Big]^{1/2} = \frac{U}{2} \pm \lambda_1, \\ \zeta_{3,4} &= \frac{U}{2} \pm \frac{1}{2}\Big[U^2 + 4(\Omega_e - \Omega_h)^2\Big]^{1/2} = \frac{U}{2} \pm \lambda_2, \end{aligned} \tag{3.5}$$

where $\lambda_1$ and $\lambda_2$ are defined as

$$\lambda_1 = \frac{1}{2}\sqrt{U^2 + 4(\Omega_e + \Omega_h)^2}, \quad \lambda_2 = \frac{1}{2}\sqrt{U^2 + 4(\Omega_e - \Omega_h)^2}. \tag{3.6}$$

Using Eq. (3.5), we find from the Schrödinger equation the following normalized eigenvectors, $X_i$:

$$X_1 = \frac{1}{\sqrt{2(1+\alpha_1^2)}}\begin{pmatrix} 1 \\ \alpha_1 \\ \alpha_1 \\ 1 \end{pmatrix}, \quad X_2 = \frac{1}{\sqrt{2(1+\alpha_1^2)}}\begin{pmatrix} \alpha_1 \\ -1 \\ -1 \\ \alpha_1 \end{pmatrix}, \tag{3.7}$$

$$X_3 = \frac{1}{\sqrt{2(1+\alpha_2^2)}} \begin{pmatrix} -1 \\ -\alpha_2 \\ \alpha_2 \\ 1 \end{pmatrix}, \quad X_4 = \frac{1}{\sqrt{2(1+\alpha_2^2)}} \begin{pmatrix} -\alpha_2 \\ 1 \\ -1 \\ \alpha_2 \end{pmatrix}, \tag{3.8}$$

where the constants $\alpha_1$ and $\alpha_2$ are defined as follows,

$$\alpha_1 = \frac{2(\Omega_e + \Omega_h)}{U + \sqrt{U^2 + 4(\Omega_e + \Omega_h)^2}}, \tag{3.9}$$

$$\alpha_2 = \frac{-2(\Omega_e - \Omega_h)}{U + \sqrt{U^2 + 4(\Omega_e - \Omega_h)^2}}. \tag{3.10}$$

If $U$ is much smaller than $\Omega_e$, $\Omega_h$, the eigenvalues $\lambda_1, \lambda_2$ are equal to $\Omega_e \pm \Omega_h$, respectively. It is easy to check that this corresponds to independent beating of electron (with frequency $\Omega_e$) and hole (with frequency $\Omega_h$) between the dots. In the realistic limit $U \gg \Omega_e, \Omega_h$, the eigenvalues can be simplified as

$$\zeta_{1,2} \approx \frac{U}{2} \pm \left( \frac{U}{2} + \frac{(\Omega_e + \Omega_h)^2}{U} \right), \quad \zeta_{3,4} \approx \frac{U}{2} \pm \left( \frac{U}{2} + \frac{(\Omega_e - \Omega_h)^2}{U} \right). \tag{3.11}$$

We see that eigenvalues $\zeta_1$ and $\zeta_3$ are large and approximately equal to $U$, while two other eigenvalues are much smaller. The underlying physical meaning is the following: without interactions, all four eigenstates (within $\Omega_e$, $\Omega_h$) had approximately the same energies. With interactions, the states are almost degenerate *pairwise*: $a_1$ and $a_2$ have close energies which exceed the energies of $b_1$ and $b_2$ by the interaction energy, $U$.

Below, we study how the interaction modifies the dynamics of the exciton, which, without interaction, is described by Eqs. (3.2). Using the eigenvectors, Eqs. (3.7), (3.8), and the initial conditions, $a_1(0) = 1$, $b_1(0) = b_2(0) = a_2(0) = 0$, we get

$$|a_1|^2(t) = \cos^2\left[\frac{1}{2}(\lambda_1 + \lambda_2)t\right] \cos^2\left[\frac{1}{2}(\lambda_1 - \lambda_2)t\right] + \frac{1}{4}\Big[\cos(2\phi_1)\sin\lambda_1 t + \cos(2\phi_2)\sin\lambda_2 t\Big]^2, \tag{3.12}$$

$$|a_2|^2(t) = \sin^2\left[\frac{1}{2}(\lambda_1 + \lambda_2)t\right] \sin^2\left[\frac{1}{2}(\lambda_1 - \lambda_2)t\right] + \frac{1}{4}\Big[\cos(2\phi_1)\sin\lambda_1 t - \cos(2\phi_2)\sin\lambda_2 t\Big]^2, \tag{3.13}$$

$$|b_1|^2(t) = \frac{1}{4}\Big(\sin(2\phi_1)\sin\lambda_1 t - \sin(2\phi_2)\sin\lambda_2 t\Big)^2, \tag{3.14}$$

$$|b_2|^2(t) = \frac{1}{4}\Big(\sin(2\phi_1)\sin\lambda_1 t + \sin(2\phi_2)\sin\lambda_2 t\Big)^2, \tag{3.15}$$

where the constants $\phi_1$ and $\phi_2$ are defined as

$$\phi_1 = \arctan\alpha_1, \quad \phi_2 = \arctan\alpha_2. \tag{3.16}$$

Equations (3.12)-(3.15) solve the auxiliary problem of dynamics of one exciton in two coupled quantum dots. It is instructive to show that, in the limit $U \to 0$, we recover

the noninteracting result Eq. (3.2). Indeed, in the limit $U \to 0$, we have $\alpha_1 = 1$ and $\alpha_2 = -1$, then $|a_1(t)|^2 = \cos^2 \Omega_e t \cos^2 \Omega_h t$, as stated earlier. Also for $|b_1|^2$, it can easily be seen that for $U = 0$, $|b_1|^2 = \sin^2 \Omega_e t \cos^2 \Omega_h t$. Also, notice that for $\Omega_e = \Omega_h$, $\alpha_2 = 0$ and $\lambda_2 = U/2$, resulting in $|b_1|^2 = |b_2|^2$, and $|a_1|^2$ and $|a_2|^2$ differ by the phase factor of $\pi/2$.

Consider now the opposite limit $U \gg \Omega_e, \Omega_h$. Then the beating between the two frequencies, $\lambda_1$ and $\lambda_2$, emerging from the last terms in Eqs. (3.12), (3.13) gives rise to *slow* frequency $\approx 2\Omega_e\Omega_h/U$, much slower than intrinsic frequencies $\Omega_e$ and $\Omega_h$. On the other hand, expanding Eqs. (3.14) and (3.15), we see that $\sin^2$-terms oscillate with the *fast* frequency $\approx U/2 \gg \Omega_e, \Omega_h$. Both slow and fast frequencies contain the interaction energy, $U$, so that their emergence is a *many-body* effect. Concerning the general picture of the exciton dynamics, it is illustrated in Fig. 3.5. We see that $|b_1|^2$, $|b_2|^2$ move with the fast frequency, while $|a_1|^2$ and $|a_2|^2$ move with both: the fast frequency is "riding" on the slow frequency. Electron and hole initially in $a_1$, stay in $a_1$ for a long time. Occasionally one particle tunnels to the states $b_1$ or $b_2$ and then the other particle tunnels, and both particles are then in the state $a_2$ where they stay for a long time. Another prominent feature of the exciton dynamic is that probability to find electron and hole in the same dot is much higher than probability to find them in different dots. To illustrate this, we

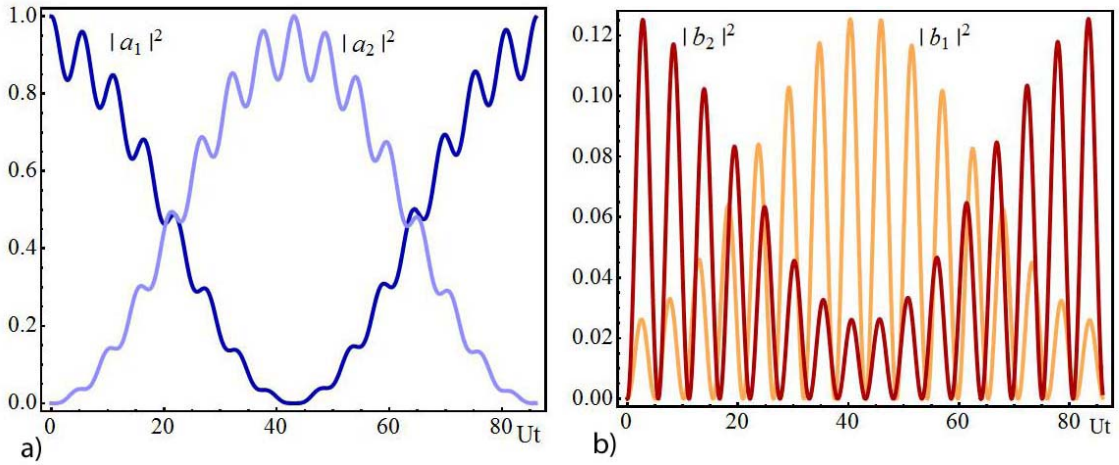


**Figure 3.5**: Population of the states are plotted from Eqs. (3.12)-(3.15) versus the dimensionless time $Ut$, for the values $\Omega_e/U = 0.1$, and $\Omega_h/U = 0.2$. (a) The occupation of the states $a_1$ and $a_2$ evolve with a *fast* frequency $\sim U/2$ riding on a *slow* frequency $\sim 2\Omega_e\Omega_h/U$. (b) Conversely, the intermediate states, $b_1$ and $b_2$, evolve with a *fast* frequency modulated by the *slow* frequency.

notice that in the large-$U$ limit, the occupation of the states can be simplified to

$$|a_1|^2 = \cos^2\left(\frac{2\Omega_e\Omega_h}{U}t\right), \qquad |b_1|^2 = \left(\frac{2\Omega_e}{U}\right)^2 \sin^2\left(\frac{U}{2}t\right),$$

$$|a_2|^2 = \sin^2\left(\frac{2\Omega_e\Omega_h}{U}t\right), \qquad |b_2|^2 = \left(\frac{2\Omega_h}{U}\right)^2 \sin^2\left(\frac{U}{2}t\right), \tag{3.17}$$

so that $|b_1|^2$, $|b_2|^2$ are $\ll 1$.

To conclude this section, we would like to make the following remark. We assumed for simplicity that electron and hole attract each other only in the states $a_1$ and $a_2$, when they reside in the same dot. In reality, they also attract each other in the states $b_1$ and $b_2$, but this attraction is weaker than in $a_1$ and $a_2$. The above consideration applies to the realistic situation if we identify $U$ with the *difference* of attractive interactions in the states $a_1$ and $b_1$. Concerning the numbers, the tunnel splittings $\Omega_e$ and $\Omega_h$ are certainly strongly dependent on the vertical separation between the dots, which varies within interval 2-10 nm. It can be as high as several meV and as low as 0.1meV [6, 7, 13, 15]. In the latest study [23] which involved the photocurrent techniques, the value $\Omega_e$ was reported to be 1.7meV for the vertical separation of the dots being 10nm.

To study the interplay of the Rabi oscillations and effects of tunneling, to which we turn in the next section, it is important to note that the actual Rabi frequency lies within the same interval. Indeed, according to Ref. [11] the typical Rabi frequency in an experiment on a self-assembled quantum dot was several meV.

## 3.3 Exciton in two QDs with near-resonant light

We now turn to the prime question: how many-body effects between two quantum dots modify the Rabi oscillations. Assume that a quantum dot molecule is being driven continuously by the near-resonant light. It is convenient to characterize these oscillations by their Fourier spectrum. For a single-dot, the light will initiate the Rabi oscillations with a *single* frequency and the magnitude depending on detuning from the resonance. Then the Fourier transform of oscillations would represent a single peak. At perfect resonance, the peak position will shift with light intensity, $I$, as $I^{1/2} \propto \Omega_R$. In reality, the decoherence processes, such as spontaneous emission, will broaden the peak. To account for these processes, it requires one to use a description based on the density matrix. However, as long as we are interested only in peak positions and the integral magnitude of the peaks, the description based on the Schödinger equation is sufficient.

The dynamics of the quantum-dot molecule can be modeled using five states. Four of them are shown in Fig. 3.4, while the fifth state is simply the vacuum state, $c$. Using this model, the Schrödinger equation can be written in the rotating wave approximation as

$$i\frac{\partial}{\partial t}\begin{pmatrix} a_1 \\ b_1 \\ b_2 \\ c \\ a_2 \end{pmatrix} = \begin{pmatrix} \omega_{10}+U & \Omega_e & \Omega_h & \Omega_R e^{-i\omega_L t} & 0 \\ \Omega_e & \omega_{10} & 0 & 0 & \Omega_h \\ \Omega_h & 0 & \omega_{10} & 0 & \Omega_e \\ \Omega_R e^{i\omega_L t} & 0 & 0 & 0 & \Omega_R e^{i\omega_L t} \\ 0 & \Omega_h & \Omega_e & \Omega_R e^{-i\omega_L t} & \omega_{10}+U \end{pmatrix} \begin{pmatrix} a_1 \\ b_1 \\ b_2 \\ c \\ a_2 \end{pmatrix}. \tag{3.18}$$

The eigenvalues, $\chi$, of Eq. (3.18), are determined in a standard way by using the following substitutions:

$$\begin{aligned} a_1 &= A_1 \exp[-i(\chi+\omega_{10})t], \qquad & b_1 &= B_1 \exp[-i(\chi+\omega_{10})t], \\ a_2 &= A_2 \exp[-i(\chi+\omega_{10})t], \qquad & b_2 &= B_2 \exp[-i(\chi+\omega_{10})t], \\ & & c &= C \exp[-i(\chi+\omega_{10}-\omega_L)t]. \end{aligned} \tag{3.19}$$

The matrix equation, Eq. (3.18), written as a set of equations, now reads

$$\begin{aligned} (\chi-U)A_1 &= \Omega_e B_1 + \Omega_h B_2 + \Omega_R C, \qquad & \chi B_1 &= \Omega_e A_1 + \Omega_h A_2, \\ (\chi-U)A_2 &= \Omega_h B_1 + \Omega_e B_2 + \Omega_R C, \qquad & \chi B_2 &= \Omega_h A_1 + \Omega_e A_2, \\ & & (\chi+\delta-U)C &= \Omega_R(A_1+A_2), \end{aligned} \tag{3.20}$$

where $\delta = U + \omega_{10} - \omega_L$, and represents detuning of the driving light. In this regime, the eigenvalues can be separated into symmetric and antisymmetric modes. This physically obvious fact is revealed by reducing the system, Eq. (3.20), to two coupled equations by excluding the terms, $B_1$, $B_2$, and $C$. Then one gets

$$\left[(\chi-U) - \frac{1}{\chi}\Big({\Omega_e}^2 + {\Omega_h}^2\Big) - \frac{\Omega_R^2}{\delta-U+\chi}\right] A_1 = \left[\frac{2\Omega_e\Omega_h}{\chi} + \frac{\Omega_R^2}{\delta-U+\chi}\right] A_2, \tag{3.21}$$

$$\left[(\chi-U) - \frac{1}{\chi}\Big({\Omega_e}^2 + {\Omega_h}^2\Big) - \frac{\Omega_R^2}{\delta-U+\chi}\right] A_2 = \left[\frac{2\Omega_e\Omega_h}{\chi} + \frac{\Omega_R^2}{\delta-U+\chi}\right] A_1. \tag{3.22}$$

From Eqs. (3.21) and (3.22), we see that for antisymmetric modes, $A_1 = -A_2$, the Rabi frequency vanishes, while for symmetric modes, the modified Rabi frequency is determined from the roots of the cubic equation. Using $A_1 = A_2$, Eqs. (3.21) and (3.22) give the following cubic equation

$$(\chi+\delta-U)\Big[\chi(\chi-U) - (\Omega_e+\Omega_h)^2\Big] = 2\Omega_R^2\chi. \tag{3.23}$$

Our main finding in this chapter, the nontrivial evolution of the spectrum of the Rabi oscillations with $U$, is encoded in the roots of the cubic equation Eq. (3.23).

What is left to do is to determine the eigenvectors and use the initial conditions, that the state $c$ is initially occupied, $c(0) = 1$, while all other states are unoccupied, $a_1(0) = a_2(0) = b_1(0) = b_2(0) = 0$. Before we proceed further with studying how many-body effects modify the Rabi oscillations, we will first incorporate $\Omega_R$ perturbativly to study the dynamics of the weakly driven system.

### 3.3.1 Weak driving

As $\Omega_R \to 0$, the system initially in the vacuum state $c$ will remain in this state. More interesting is how the population of the states evolves with time at weak driving $\Omega_R \ll U, \Omega_e, \Omega_h$, when the change of the population of the ground state is small and proportional to $\Omega_R^2$. If $U$, $\Omega_e$, $\Omega_h$ are all zero, then the known result for $c^2(t)$ has the form

$$|c(t)|^2 = 1 - \frac{\sqrt{2}\Omega_R^2}{\sqrt{2}\Omega_R^2 + \delta^2} \sin^2\big(\sqrt{\delta^2 + 2\Omega_R^2}\, t\big), \tag{3.24}$$

so that for small $\Omega_R$, the magnitude of the correction is $\Omega_R^2/\delta^2$, while the oscillation frequency is simply equal to detuning between the incident light frequency and the spacing between the ground and excited states. To contrast this result to the case of finite $U$, $\Omega_e$, $\Omega_h$ we notice that at small $\Omega_R$, the solutions of Eq. (3.23) are $\chi = U - \delta$ and also $\chi_1 = \zeta_1$, $\chi_2 = \zeta_2$, which are given by Eq. (3.5). Using these solutions and satisfying the initial conditions, we get

$$\begin{aligned} |c(t)|^2 \;=\; 1 - \frac{4\Omega_R^2}{\delta(U-\delta) + \big(\Omega_e + \Omega_h\big)^2} \Bigg[ 1 - \left(\frac{\zeta_1 - \delta}{\zeta_2 - \delta}\right) \frac{\zeta_1 \cos\left[(\zeta_2 - \delta)\, t\right]}{2\zeta_1 - U} \\ + \left(\frac{\zeta_2 - \delta}{\zeta_1 - \delta}\right) \frac{\zeta_2 \cos\left[(\zeta_1 - \delta)\, t\right]}{2\zeta_1 - U} \Bigg]. \end{aligned} \tag{3.25}$$

Equation (3.25) has a transparent physical meaning: weak driving of the system causes relatively weak $\propto \Omega_R^2$ oscillating correction to the occupation of the ground state, while corresponding frequencies are the "internal" frequencies of the system. In a way, this is analogous to a harmonic oscillator under weak *nonresonant* drive. A nontrivial question is, what are the relative amplitudes of the two internal frequencies in the oscillating correction in Eq. (3.25). It can be readily seen from Eq. (3.25) that, when $U$ is comparable to $(\Omega_e + \Omega_h)$, the amplitudes are also comparable to each other. However, for $U \gg (\Omega_e + \Omega_h)$, the "fast" frequency, being close to $U$, has a much smaller amplitude than the "slow" frequency, $(\Omega_e + \Omega_h)^2/U$. The ratio of amplitudes is then $\sim (\Omega_e + \Omega_h)^2/U^2$.

At this point, an important remark is in order. Equation (3.23) has *three* roots, and, in principle, there should be three oscillating corrections in Eq. (3.25). However, the

third correction having frequency $\delta - U$ has an amplitude $\propto \Omega_R^4$, i.e., much smaller than the oscillating terms kept in Eq. (3.25). This situation will change in the case of resonant driving to which we now turn.

### 3.3.2 Resonant driving

It is clear that, when $\Omega_R$ exceeds all internal frequencies of the system, i.e., the spacings between the energies of the states $a_1$ and $b_1$, then $|c|^2$ will assume the conventional "Rabi" form $c^2(t) = \cos^2(\sqrt{2}\Omega_R t)$. The really interesting issue is the evolution of the frequencies and amplitudes in Eq. (3.25) as $\Omega_R$ becomes comparable to internal frequencies. To assess this regime, we rewrite the cubic equation, Eq. (3.23), by using the dimensionless variable,

$$\chi = s\eta + \frac{1}{3}\big(2U - \delta\big), \tag{3.26}$$

where

$$s = \left[\frac{1}{12}\left(2U - \delta\right)^2 + 2\Omega_R^2 + \Big(\Omega_e + \Omega_h\Big)^2 + \frac{1}{4}\delta^2\right]^{1/2}. \tag{3.27}$$

Then the cubic equation, Eq. (3.23), assumes the form

$$\eta^3 - \eta + f = 0. \tag{3.28}$$

The dimensionless eigenvalues are now to be determined by a single dimensionless parameter $f$ defined as

$$f = \frac{\frac{1}{108}(2U-\delta)^3 - \frac{1}{6}\big(2U-\delta\big)\Big[4\Omega_R^2 - \big(\Omega_e+\Omega_h\big)^2 + \frac{1}{2}\delta^2\Big] - \frac{1}{2}\delta\big(\Omega_e+\Omega_h\big)^2}{\left[\frac{1}{12}\big(2U-\delta\big)^2 + 2\Omega_R^2 + \Big(\Omega_e+\Omega_h\Big)^2 + \frac{1}{4}\delta^2\right]^{3/2}}. \tag{3.29}$$

Graphical solution of Eq. (3.28) is illustrated in Fig. 3.6. Since all three roots, $\eta_i$, must be real, the parameter $f$ must reside within the interval $-\frac{2}{3\sqrt{3}}, \frac{2}{3\sqrt{3}}$ for *any* set of parameters, $U, \Omega_R, \Omega_e + \Omega_h$, and $\delta$. It is seen from Eq. (3.29) that weak interaction corresponds to small $f \ll 1$, while the limiting value $f \approx \frac{2}{3\sqrt{3}}$ corresponds to $U \to \infty$. As we will see below, the nontrivial evolution of the spectrum of the Rabi oscillations takes place at intermediate $f$. At intermediate $f$, the roots of Eq. (3.28) are given by

$$\eta_1 = -\mathrm{sgn}(f)\frac{2}{\sqrt{3}}\cos\left(\frac{\psi}{3}\right), \quad \eta_2 = -\mathrm{sgn}(f)\frac{2}{\sqrt{3}}\cos\left(\frac{\psi}{3} + \frac{2\pi}{3}\right),$$

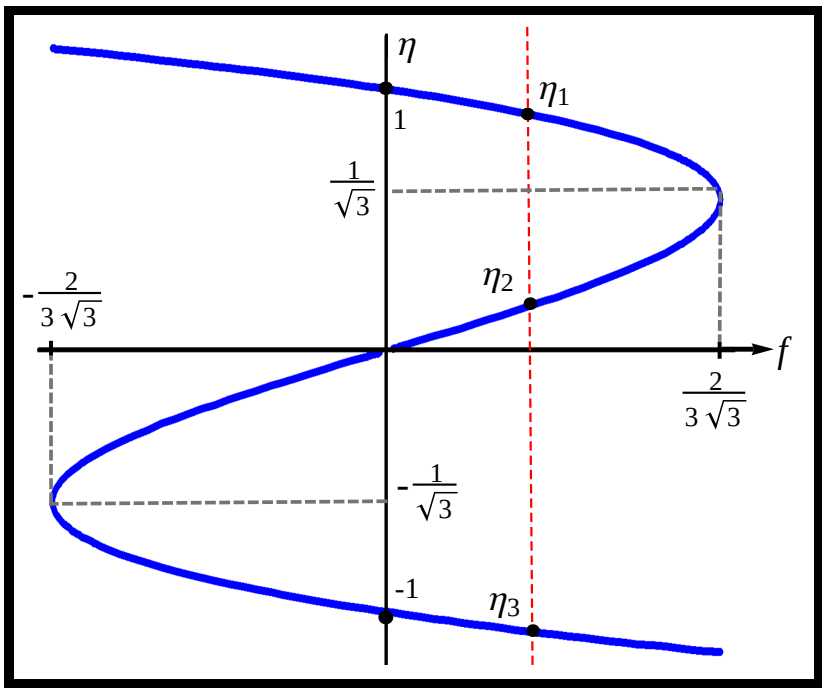


**Figure 3.6**: Graphic solution of the cubic equation, Eq. (3.28). Note that at $f = 0$ we have $\eta_1 = 1$, $\eta_2 = 0$, and $\eta_3 = -1$, while at the maximum $f = +2/3\sqrt{3}$ we have two degenerate eigenvalues, $\eta_1 = \eta_2 = \frac{1}{\sqrt{3}}$, and a third distant, $\eta_3 = -\frac{2}{\sqrt{3}}$.

$$\eta_3 = -\mathrm{sgn}(f)\frac{2}{\sqrt{3}}\cos\left(\frac{\psi}{3} - \frac{2\pi}{3}\right). \tag{3.30}$$

where the phase $\psi$ is determined as

$$\psi = \arctan\left(\frac{1}{f}\sqrt{\frac{4}{27} - f^2}\right). \tag{3.31}$$

The eigenvectors of the system Eq. (3.20) corresponding to the roots can be conveniently cast in the form

$$X_i = \begin{pmatrix} \frac{3s\eta_i - (U-2\delta)}{6\Omega_R} \\ 1 \\ \frac{3s\eta_i - (U-2\delta)}{6\Omega_R} \end{pmatrix}. \tag{3.32}$$

We are now in position to calculate the population of the state $c$. Using the eigenvectors, Eq. (3.32), and eigenvalues, Eq. (3.30), the general expression of $|c|^2$ can be written as

$$|c|^2 = C_1^2 + C_2^2 + C_3^2 + 2C_1C_2\cos\left[(\eta_1 - \eta_2)st\right] + 2C_1C_3\cos\left[(\eta_1 - \eta_3)st\right] + 2C_2C_3\cos\left[(\eta_2 - \eta_3)st\right], \tag{3.33}$$

where the three constants $C_1$, $C_2$, and $C_3$, are determined from the initial conditions. The value of these three constants is easily solved for, which gives

$$C_1 = \frac{\big[3s\eta_1 + (2U-\delta)\big]\big[3s\eta_2 - (U-2\delta)\big]\big[3s\eta_3 - (U-2\delta)\big]}{27s^2\big(U-\delta\big)(3\eta_1^2-1)},$$
$$C_2 = \frac{\big[3s\eta_2 + (2U-\delta)\big]\big[3s\eta_1 - (U-2\delta)\big]\big[3s\eta_3 - (U-2\delta)\big]}{27s^2\big(U-\delta\big)(3\eta_2^2-1)},$$
$$C_3 = \frac{\big[3s\eta_3 + (2U-\delta)\big]\big[3s\eta_1 - (U-2\delta)\big]\big[3s\eta_2 - (U-2\delta)\big]}{27s^2\big(U-\delta\big)(3\eta_3^2-1)}. \tag{3.34}$$

Equations (3.30), (3.31), and (3.34) constitute the analytical solution of the problem. We see that the Fourier spectrum of the Rabi oscillations consists of three peaks corresponding to the frequencies $(\eta_1-\eta_2)s$, $(\eta_1-\eta_3)s$, and $(\eta_2-\eta_3)s$ (the third equal to the difference between the first two) with heights given by $2C_1C_2$, $2C_1C_3$, and $2C_2C_3$, respectively.

Before proceeding to the analysis of the spectrum, we would like to point out that our study of the Rabi oscillations in a quantum dot molecule is conceptually related to the study reported in Refs. [27, 28, 29], of the Rabi oscillations in the system of two localized spins driven by the ac magnetic field. In Refs. [27, 28, 29] the spins were coupled by "density-density" type interaction, which was either *weak* exchange or *weak* dipole-dipole interaction, which, in our theory, is "mimicked" by $U$ being present only in the states $a_1$, $a_2$. On the other hand, there is no analog of the tunnel splittings, $\Omega_e$, $\Omega_h$ in the two-spin model.

## 3.4 Analysis

Below, we will measure $\Omega_R$, $\delta$, and $U$ in the natural units, $\Omega_e+\Omega_h$, which is the net tunnel splitting:

$$z = \frac{\sqrt{2}\Omega_R}{(\Omega_e+\Omega_h)}, \quad \Delta = \frac{\delta}{2(\Omega_e+\Omega_h)}, \quad u = \frac{U}{(\Omega_e+\Omega_h)}. \tag{3.35}$$

Then parameter $s$ introduced above takes the form

$$s(u,\Delta,z) = (\Omega_e+\Omega_h)\left[\frac{1}{3}(u-\Delta)^2 + \big(1+z^2\big) + \Delta^2\right]^{1/2}. \tag{3.36}$$

In terms of new variables the expression for parameter $f$ takes the form

$$f(u,\Delta,z) = \frac{(u-\Delta)\Big[\frac{2}{27}(u-4\Delta)(u+2\Delta) - \frac{1}{3}(2z^2-1)\Big] - \Delta}{\big[\frac{1}{3}(u-\Delta)^2 + \big(1+z^2\big) + \Delta^2\big]^{3/2}}. \tag{3.37}$$

What makes the Rabi oscillations in a quantum dot molecule nontrivial is the fact that $f$ exhibits a *nonmonotonic* dependence on $z$ within a certain domain of $u$ and $\Delta$, as can

be seen in Fig. 3.7. Besides the obvious extremum at $z = 0$, the position of the nontrivial extremum $z = z_c$ can be found analytically

$$z_c = \sqrt{u^2 - 2\Delta u - \frac{1}{2}\Big(9\Delta - 7\Big)}\ , \tag{3.38}$$

which corresponds to the value of $f$

$$f_c = \frac{-\frac{16}{27}(u-\Delta)^3 + (3\Delta - 2)(u-\Delta) - \Delta}{\left[\frac{4}{3}(u-\Delta)^2 - \frac{9}{2}(\Delta - 1)\right]^{3/2}}. \tag{3.39}$$

Presence of extrema in Fig. 3.7, 3.8 translates into a nontrivial transformation of the spectrum from weak $\Omega_R$, where it is determined by Eq. (3.25), to large $\Omega_R$, where the conventional Rabi oscillations are restored. To illuminate this nontriviality, we start from the noninteracting case. Setting $u = 0$, we plot $f(0, \Delta, z)$ from Eq. (3.37) for four characteristic values of $\Delta$. See Fig. 3.7. For these $\Delta$-values, we plot from Eq. (3.33) the corresponding Fourier spectrum and the peak intensities as a function of $z$. See Fig. 3.9, 3.10, 3.11.

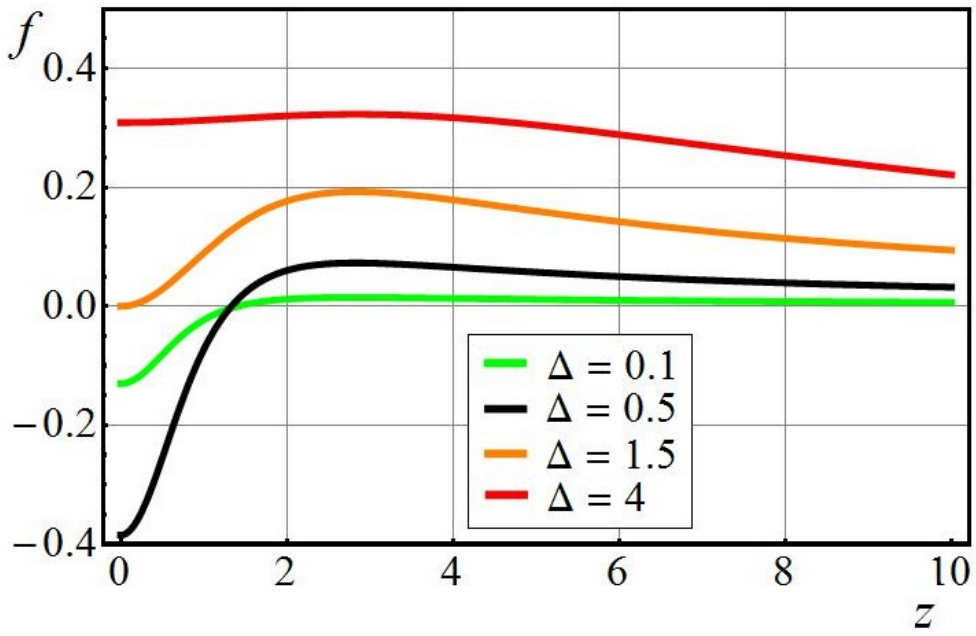


**Figure 3.7**: The function $f(0, \Delta, z)$ is plotted for four characteristic values of the dimensionless detuning, $\Delta$, from Eq. (3.37). For small $\Delta = 0.1$ the function $f$ remains small; as $\Delta$ increases, the $z = 0$ value of $f$ decreases to the limiting value $-\frac{2}{3\sqrt{3}}$, which is achieved at $\Delta = 1/2$. Further increasing $\Delta$ leads to the growth of $f(0, \Delta, 0)$ until it reaches the upper limiting value of $\frac{2}{3\sqrt{3}}$.

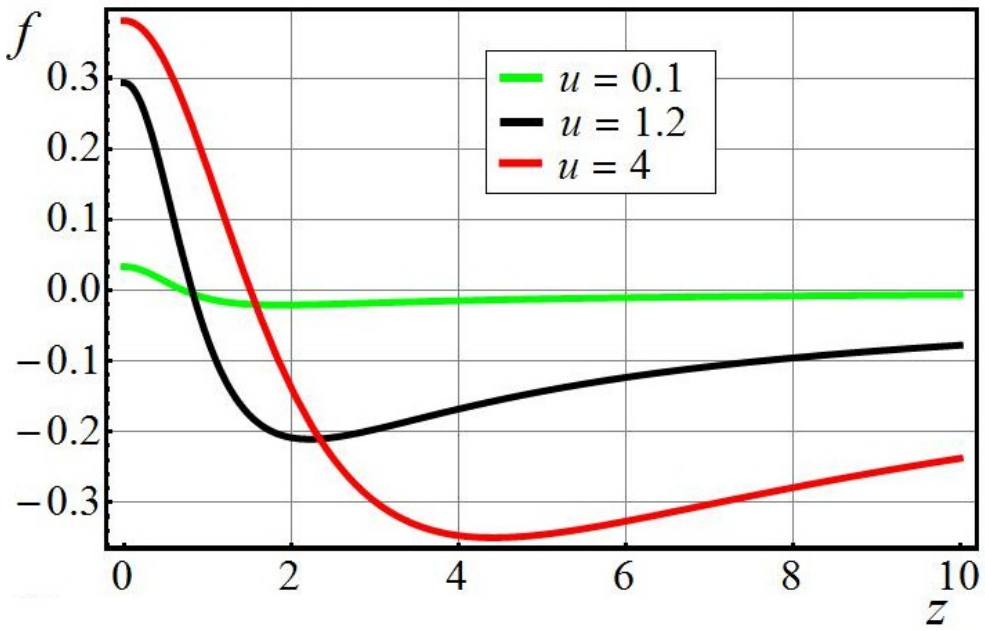


**Figure 3.8**: The function $f(u, 0, z)$ is plotted for three values of the dimensionless interaction parameter, $u$, corresponding to perfect resonance, $\Delta = 0$, for an isolated dot. As $u$ increases, the zero-$z$ value of $f$ increases monotonically and approaches the limiting value of $\frac{2}{3\sqrt{3}}$.

The behavior of the spectrum at small $z$ can be, essentially, understood from the weak driving limit. See Eq. (3.25). As follows from Eq. (3.25), the dimensionless positions of the main peaks are $(\frac{1}{4}u^2+1)^{1/2}+\frac{1}{2}u-2\Delta$ and $(\frac{1}{4}u^2+1)^{1/2}-\frac{1}{2}u+2\Delta$. These peaks have the magnitudes proportional to $z^2$. The third peak at dimensionless frequency $(u^2+4)^{1/2}$ is not captured by Eq. (3.25), since its magnitude is proportional to $z^4$. Results of the exact calculation for $u = 0$ and $\Delta = 0.1$, see Fig. 3.9, are in accord with this prediction. The exceptional behavior at small $z$ corresponds to $\Delta = 1/2$. We see that positions of two peaks are degenerate at $z = 0$, and, correspondingly, the third peak starts from zero frequency. Moreover, the positions of degenerate peaks go apart *linearly* with $z$. The precursor of this peculiar behavior can be again traced to Eq. (3.25). Namely, the denominator of Eq. (3.25) turns to zero at

$$\delta = \frac{U}{2} \pm \sqrt{\frac{U^2}{4} + (\Omega_e + \Omega_h)^2}. \tag{3.40}$$

For $u = 0$, Eq. (3.40) defines $\Delta = 1/2$. The physical origin of this anomaly is that, without interaction, the point of zero detuning shifts from $\Delta = 0$ to $\Delta = 1/2$ due to tunneling. For this reason, the position of the lowest peak in Fig. 3.10 is linear with

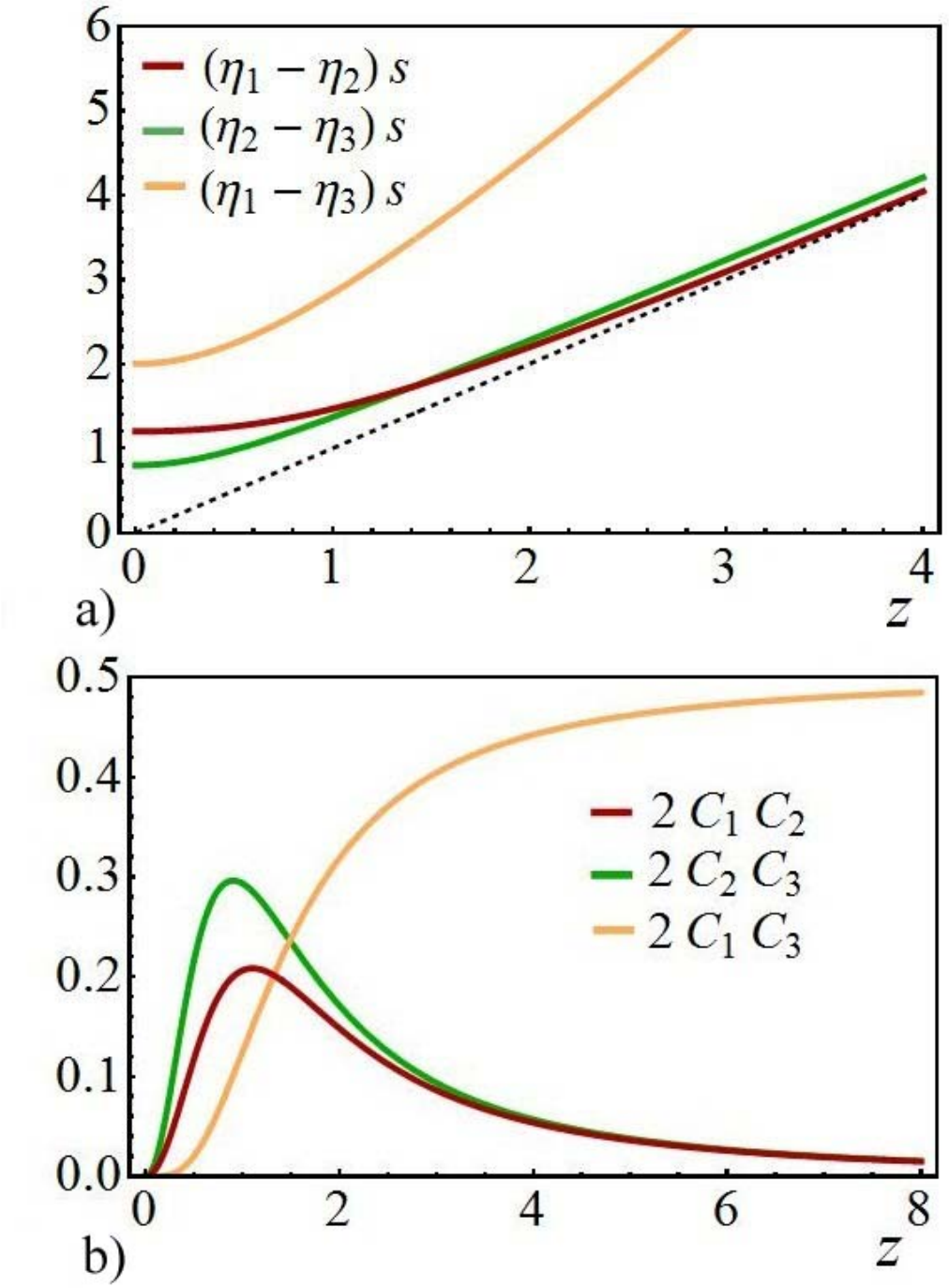


**Figure 3.9**: The Fourier transform (top) and corresponding magnitudes (bottom) for the occupation of the vacuum state, Eq. (3.33), for $\Delta = 0.1$ and $u = 0$. The behavior at small $z$ is described by Eq. (3.25), while at large $z \gg 1$, the system resumes the conventional Rabi oscillations. For intermediate $z$, we see that there is a strong redistribution of the magnitudes.

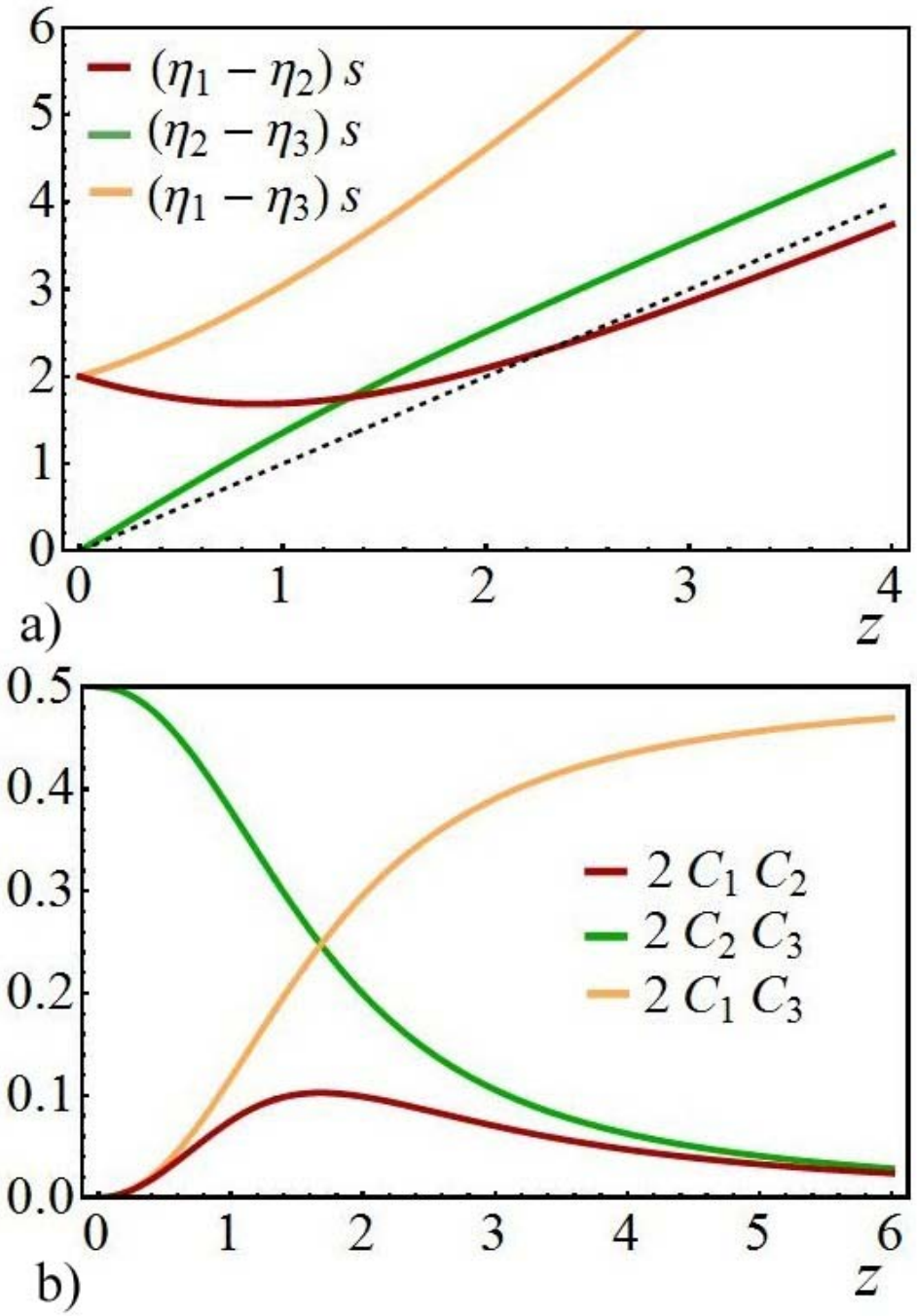


**Figure 3.10**: The same as Fig. 3.9 for $\Delta = 0.5$. Note that at small $z$, the system exhibits "true" resonance, i.e., Rabi oscillations for weak driving, described by Eq. (3.25).

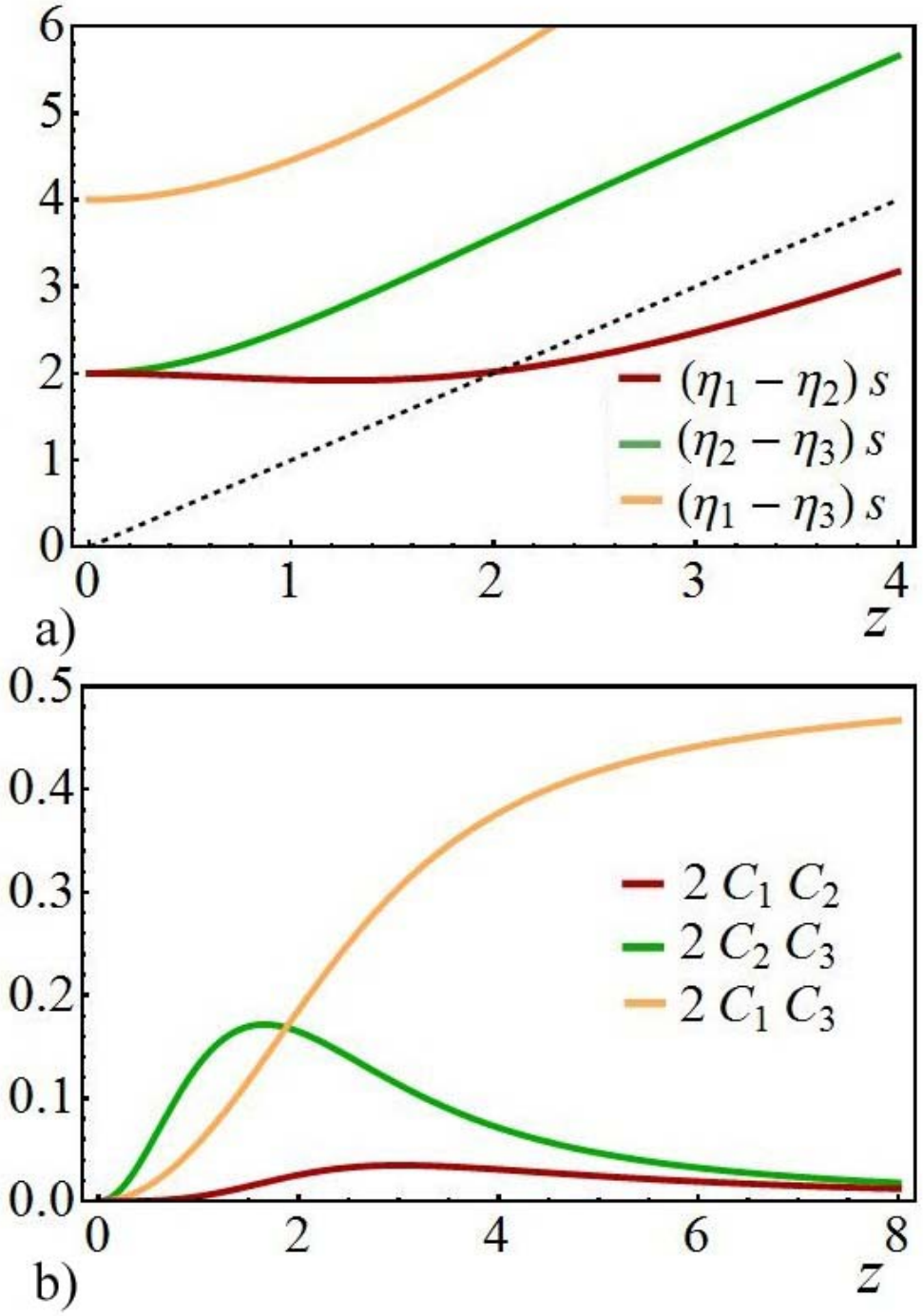


**Figure 3.11**: The same as Fig. 3.9 for $\Delta = 1.5$. At small $z$, we see two degenerate frequencies, which can be predicted from Fig. 3.7. In Fig. 3.7, for small $z$, we have $f \approx 0$, which corresponds to the relation $\eta_1 - \eta_2 \approx \eta_2 - \eta_3$, as seen in Fig. 3.6.

$z$ and has a magnitude close to 0.5, corresponding to fully developed Rabi oscillations. Based on the exact expressions Eq. (3.34), we specify the behavior of intensities of all three peaks at small $z$. Note that at $\Delta = 1/2$, the value of $f(0, 1/2, 0)$ is equal to the limiting value $-\frac{2}{3\sqrt{3}}$. In the vicinity of this value the asymptotic expressions for $\eta$-values are

$$\eta_1 = \frac{1}{3}\left(2\sqrt{3} - \frac{2}{3\sqrt{3}} + f\right), \quad \eta_2 = -\frac{1}{\sqrt{3}}\left(1 + 3^{1/4}\sqrt{\frac{2}{3\sqrt{3}} + f}\right),$$
$$\eta_3 = -\frac{1}{\sqrt{3}}\left(1 - 3^{1/4}\sqrt{\frac{2}{3\sqrt{3}} + f}\right). \tag{3.41}$$

On the other hand, at small $z$, the difference between $f(0, 1/2, z)$ and $-\frac{2}{3\sqrt{3}}$ is proportional to $z^2$. This suggests that $\eta_2$ and $\eta_3$ have corrections linear in $z$, which is reflected in the positions of spectral lines in Fig. 3.10. We now turn to Eq. (3.34) and find that at $\Delta = 1/2$, we have $(C_2 - 1/2) = (1/2 - C_3) \propto z$, while $C_1 \propto z^2$. The difference of signs in the corrections $(C_2 - 1/2)$ and $(C_3 - 1/2)$ comes from the last brackets in the numerators in the expressions for $C_2$ and $C_3$, and the fact that linear in $z$ corrections to $\eta_2$ and $\eta_3$ have opposite signs. Therefore, the magnitude, $2C_2C_3$, of the low-frequency peak decreases quadratically from $z = 0$, where it is equal to 0.5, while the magnitudes of two other peaks grow with $z$ as $z^2$. Since $f(0, 3/2, z)$ behaves quadratically with $z$, Eq. (3.43) suggests that the two degenerate spectral lines go apart as $z^2$ at small $z$. Concerning the peak magnitudes, the lower of two degenerate peaks grows slowly, as $z^4$, at small $z$, while the upper peak, as well as the double-frequency peak, behave as $z^2$. This could be expected on the basis of weak-driving expansion Eq. (3.25), which suggests that only two peaks exhibit $z^2$-behavior. Another peculiarity in the small-$z$ behavior of the spectral lines takes place at $\Delta = 3/2$, where the two peaks are again degenerate, while the third peak is at double frequency. The origin of this degeneracy is that $f(0, 3/2, 0) = 0$, as follows from Eq. (3.37). At small finite $f$, the corresponding $\eta$-values can be simplified to

$$\eta_1 = 1 - \frac{f}{2}, \quad \eta_2 = f, \quad \eta_3 = -1 - \frac{f}{2}. \tag{3.42}$$

Since $f(0, 3/2, z)$ behaves quadratically with $z$, Eq. (3.43) suggests that the two degenerate spectral lines go apart as $z^2$ at small $z$. Concerning the peak magnitudes, the lower of two degenerate peaks grows slowly, as $z^4$, at small $z$, while the upper peak, as well as the double-frequency peak, behave as $z^2$. This could be expected on the basis of weak-driving expansion Eq. (3.25), which suggests that only two peaks exhibit $z^2$-behavior. Another

peculiarity in the small-$z$ behavior of the spectral lines takes place at $\Delta = 3/2$, where the two peaks are again degenerate, while the third peak is at double frequency. The origin of this degeneracy is that $f(0, 3/2, 0) = 0$, as follows from Eq. (3.37). At small finite $f$ the corresponding $\eta$-values can be simplified to

$$\eta_1 = 1 - \frac{f}{2}, \quad \eta_2 = f, \quad \eta_3 = -1 - \frac{f}{2}. \tag{3.43}$$

Analysis of the spectral lines for strong driving $z \gg 1$ is straightforward. This is because parameter $f$ falls off with increasing $z$ as $1/z$, see Eq. (3.37). This means that the expressions Eq. (3.43) for $\eta$-values apply for large $z$. Taking into account that parameter $s$ grows linearly with $z$, we conclude that the position of the upper spectral line is $2z$, which corresponds to the conventional Rabi oscillations. The positions of two satellites are close to $z$. Their deviations from $z$ have equal values and opposite signs. A nontrivial feature is that these deviations, $\pm 3sf/2$, *saturate* with increasing $z$ at $\frac{2}{3}(u-\Delta)(\Omega_e+\Omega_h)$. Concerning the magnitudes of the peaks, it can be easily seen from Eq. (3.34) that at large $z$, the coefficients $C_1$ and $C_3$ approach $1/2$. This suggests that the main spectral line approaches the conventional magnitude $2C_1C_3 = 0.5$. It is less trivial to extract from the expression for $C_2$ that it behaves as $1/z^2$ at large $z$, which corresponds to $(\Omega_e+\Omega_h)^2/2\Omega_R^2$ in the dimensional units. This fall off of the magnitude of the satellites is illustrated by all numerical curves in Figs. 3.9-3.11.

The most interesting behavior of the spectral lines takes place at intermediate $z$, namely around $z = 2$, i.e., $\Omega_R \approx \sqrt{2}(\Omega_e + \Omega_h)$. As can be seen in Figs. 3.9-3.11, a strong redistribution of magnitudes takes place in this domain. While for smaller $z$ the green line $s(\eta_2 - \eta_3)$ has a maximal magnitude, while the yellow "Rabi" line is suppressed, for larger $z$, the maximal magnitude is transferred to this Rabi line, $s(\eta_1 - \eta_3)$.

The analysis of the evolution of spectrum with increasing the interaction parameter $u$ is much similar to the above analysis of the evolution with $\Delta$. To easier embrace this evolution, the magnitudes of the peaks are encoded in the thicknesses of the spectral lines in Fig. 3.12 and 3.13. In Fig. 3.13, we see that at small $z$, two of the magnitudes are much bigger than the third one, in accord with weak-driving analysis. The condition Eq. (3.40) of peak degeneracy is never met at $\Delta = 0$, but it is progressively satisfied as $U$ increases. For this reason, the situation low-field Rabi oscillation, that took place at $\Delta = 1/2$ and $u = 0$, also takes place at $\Delta = 0$ *asymptotically* in the limit of large $u$. The large-$z$ behaviors of the spectrum versus $\Delta$ and versus $u$ are similar to each other. What distinguishes the evolution with $u$ is the behavior of lines at intermediate $z$. In Fig. 3.13,

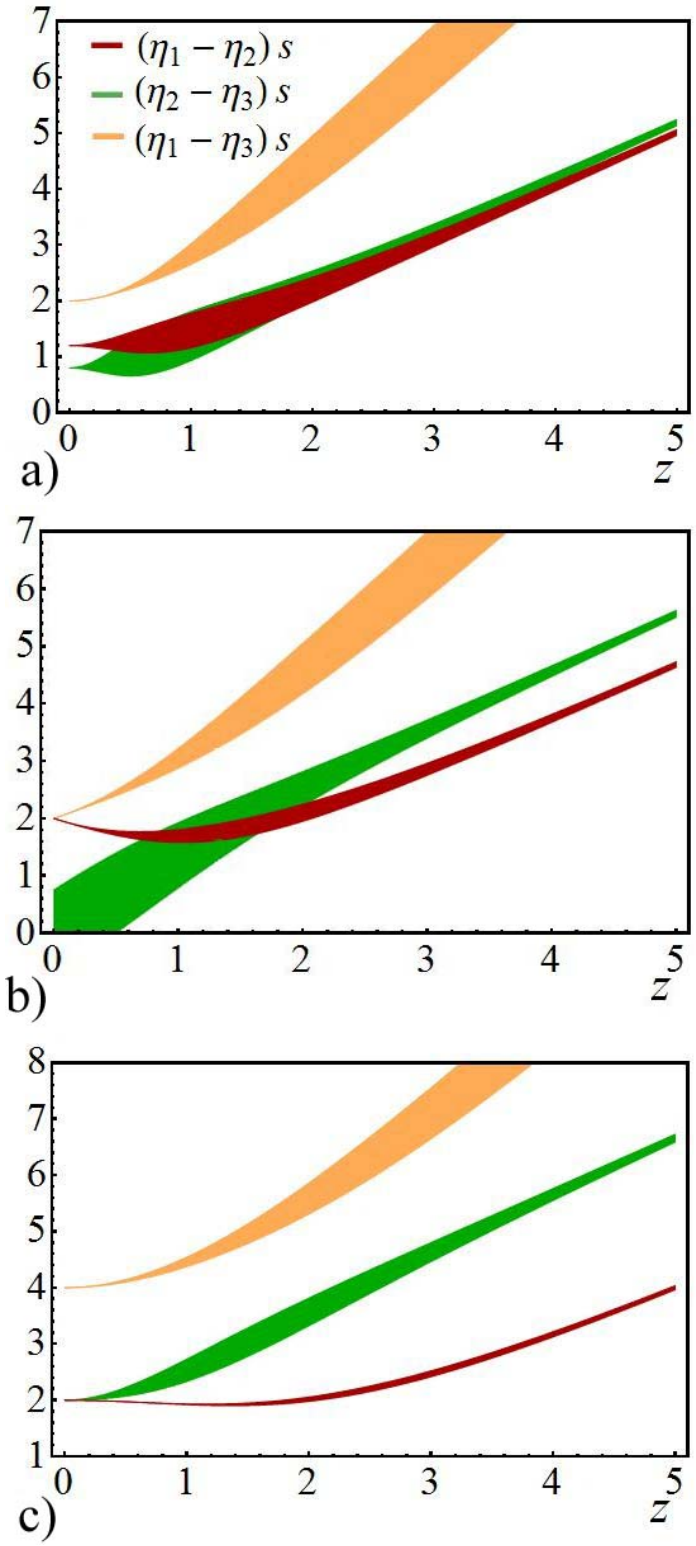


**Figure 3.12**: Both the peak positions and intensities are shown, corresponds to Fig. 3.9-3.11, for $u = 0$ and three values of $\Delta$, (a) $\Delta = 0.1$, (b) $\Delta = 0.5$, (c) $\Delta = 1.5$. The intensities are encoded in the thicknesses of the lines.

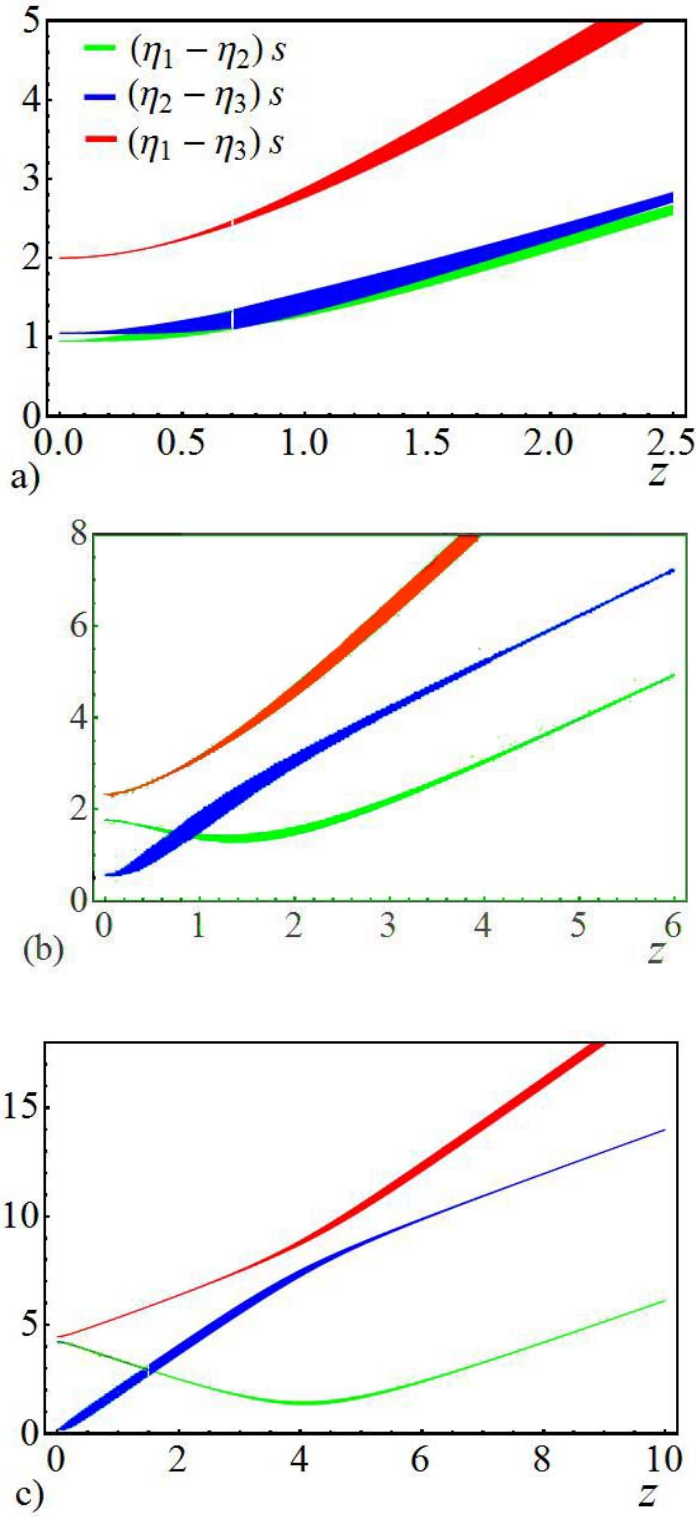


**Figure 3.13**: Both the peak positions and intensities are shown for $\Delta = 0$ and three values of $u$: (a) $u = 0.1$, (b) $u = 1.2$, (c) $u = 4$. The intensities are encoded in the thicknesses of the lines. We see similar features as with the evolution of $\Delta$, for instance, in (a) the minimum in the blue or green lines corresponds to the minimum in $f$, as seen in Fig. 3.8. (b) We see that for both weak and strong driving, $z$, that the position of the dominate peak is close to the conventional Rabi frequency. While for intermediate $z$, we see a redistribution of magnitudes from the green line to the red line.

we see clear minima in the positions of the lowest line. These minima could be traced to the minima in the dependence of $f(u, 0, z)$ in Fig. 3.8. These minima are deep and are specific for finite $u$ rather than finite $\Delta$. It can be seen from Fig. 3.13, that the magnitude of the lower line has a maximum as the line passes through a minimum.

Our overall prediction for the experiment on the Rabi oscillations in a quantum dot molecule is that the Fourier transform of these oscillations should contain three major components with their magnitudes strongly sensitive to the amplitude, $\Omega_R$, of the driving field. The "smoking gun" prediction is rather abrupt redistribution in the intensities of these components as $\Omega_R$ exceeds the "internal" frequency of the system set by combination of interaction and tunneling.

## 3.5 Relation to the Rabi oscillations in spin pairs detected by PEDMR

In the bulk of this chapter, we studied peculiarities of the Rabi oscillations in a quantum dot molecule, which we modeled by two identical two-level systems coupled by tunneling. Correlated exciton dynamics in this system was due to difference between intrasystem and intersystem electron-hole interaction. We would like to point out that an arrangement, similar to a quantum dot molecule, can be identified in organic light-emitting diodes (OLEDs).

In OLEDs, the role of a two-level system is played by Zeeman levels of a carrier in a magnetic field. Since recombination of two carriers (electron and hole) plays a crucial role in the performance of OLEDs, the most interesting situation takes place when these carriers are situated close in space. Then the spin levels of these two carriers can be loosely viewed as a quantum dot molecule. There is certainly no one-to-one correspondence between the Hamiltonian of a quantum dot molecule and the spin part of the Hamiltonian of the electrostatically bound carrier pair in OLED. First, the tunneling that played an important role in the quantum dot molecule is not present in the spin Hamiltonian. In principle, this tunneling could be emulated by the spin-orbit coupling. However, in OLEDs, this coupling is weak. Secondly, there is no excitonic effect, which we modeled by parameter $U$ in a pair of Zeeman levels. On the other hand, a pair of two Zeeman levels possesses specifics that are missing in a quantum dot molecule, namely, the exchange interaction between two spins within a given carrier pair.

For the reasons listed above, it is interesting to explore what features of the collective Rabi oscillations uncovered for the quantum dot molecule carry over to the Rabi oscilla-

tions in an electrostatically bound carrier pair in OLED. Additional motivation for this study is that experimental analysis of the Fourier spectrum of the Rabi oscillations, to which predictions of the present chapter pertain, was recently reported in Ref. [24] for oscillations excited in OLEDs. These oscillations and their Fourier transforms are shown in Figs. 3.14, 3.15. In theoretical interpretation of their results, the authors of Ref. [24] pointed out the importance of asymmetry of the components of the pair caused by the fact that electron and hole have a different nuclear environment. For this reason, unlike the quantum dot molecule, in the subsequent consideration, we assume that the Zeeman splittings $\omega_a$ and $\omega_b$, for spins **a** and **b**, respectively, see Fig. 3.16, are slightly different. The Hamiltonian of the system in the presence of the driving magnetic field, $B_1$, directed along $x$-axis reads

$$\hat{H} = \frac{\omega_a}{2}\hat{\sigma}_{za} + \frac{\omega_b}{2}\hat{\sigma}_{zb} + \frac{J}{4}\hat{\sigma}_a \cdot \hat{\sigma}_b + \frac{\gamma B_1}{2}\left(\hat{\sigma}_{xa} + \hat{\sigma}_{xb}\right)\cos\omega_L t, \tag{3.44}$$

where $\gamma$ is the gyromagnetic ratio and $J$ is the exchange constant.

To make connection to the corresponding Eq. (3.18), we write the Schrödinger equation in the RWA for all four amplitudes defined in Fig. 3.16.

$$i\frac{\partial}{\partial t}\begin{pmatrix} A_1 \\ A_2 \\ A_+ \\ A_- \end{pmatrix} = \frac{1}{2}\begin{pmatrix} -(\omega_a+\omega_b)-\frac{J}{2} & 0 & \Omega_R e^{-i\omega_L t} & \Omega_R e^{-i\omega_L t} \\ 0 & (\omega_a+\omega_b)-\frac{J}{2} & \Omega_R e^{i\omega_L t} & \Omega_R e^{i\omega_L t} \\ \Omega_R e^{i\omega_L t} & \Omega_R e^{-i\omega_L t} & -(\omega_a-\omega_b)+\frac{J}{2} & -J \\ \Omega_R e^{i\omega_L t} & \Omega_R e^{-i\omega_L t} & -J & (\omega_a-\omega_b)+\frac{J}{2} \end{pmatrix}\begin{pmatrix} A_1 \\ A_2 \\ A_+ \\ A_- \end{pmatrix}, \tag{3.45}$$

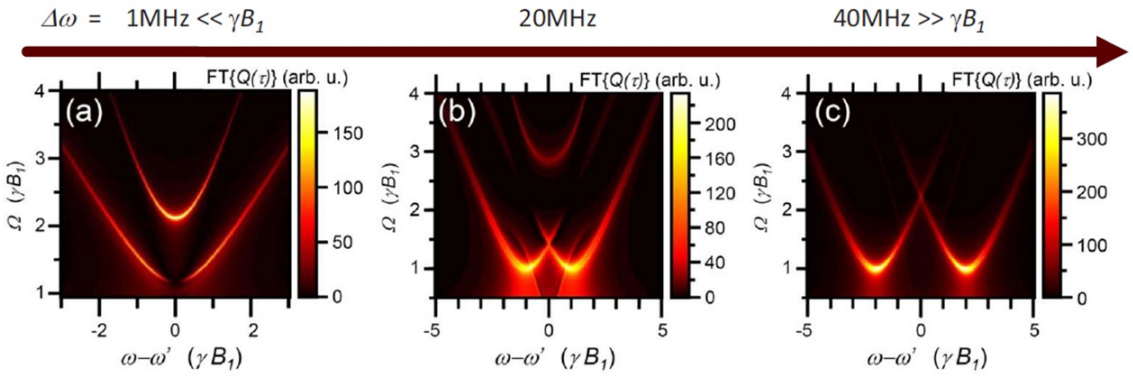


**Figure 3.14**: Numerical results are shown corresponding the Hamiltonian, Eq. (3.44), for spin-exchange coupling $J/h$ = 1MHz, from Ref. [28]; (a) $\Delta$ = 0.5MHz$\ll \Omega_R$, (b) $\Delta$ = 1MHz, (c) $\Delta$ = 20MHz$\gg \Omega_R$. The Authors plot the peak position, $\Omega$, versus detuning, $\delta$, (in the units of $\Omega_R$). From our results obtained in Figs. 3.13 b, c, we see the similar finding that different peaks have *opposite* slopes as a function of $\delta$.

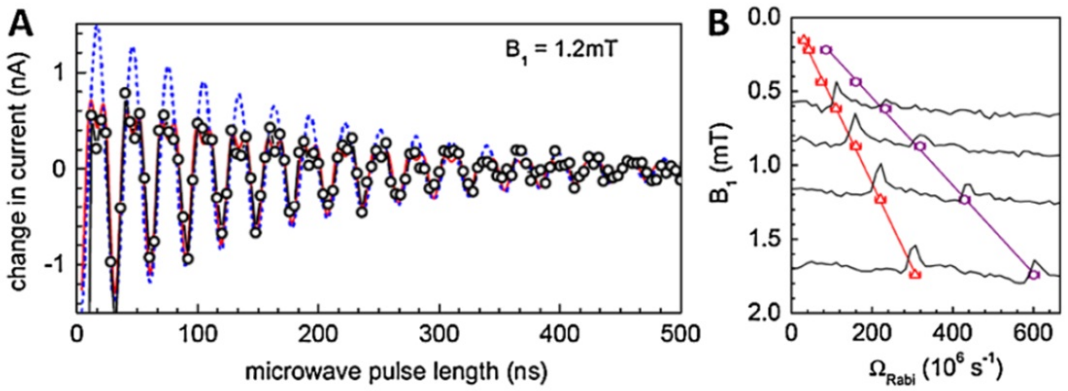


**Figure 3.15**: Plot of the measured Rabi oscillations on pairs of electrostatically bound charge carriers, for weak spin-exchange coupling is shown in (a); while in (b), the Fourier transform spectra of Rabi oscillations obtained at different $B_1$ field strengths is shown, from Ref. [30]. The red line corresponds to the frequency $\Omega_R$ where both spins precess independently, while the purple line corresponds to $2\Omega_R$ where the spin pair precesses jointly.

where $\Omega_R = \gamma B_1$. Using the substitutions

$$A_1 = a_1 e^{-i(\chi+\omega_L)t}, \quad A_2 = a_2 e^{-i(\chi-\omega_L)t}, \quad A_+ = a_+ e^{-i\chi t}, \quad A_- = a_- e^{-i\chi t}, \tag{3.46}$$

we get the following system of algebraic equations for the quasienergies

$$\begin{aligned}
\left(\chi + \Delta - \frac{J}{4}\right) a_+ &= \frac{\Omega_R}{2}\Big(a_1 + a_2\Big) - \frac{J}{2} a_-, \qquad \left(\chi - \delta + \frac{J}{4}\right) a_1 = \frac{\Omega_R}{2}\Big(a_+ + a_-\Big), \\
\left(\chi - \Delta - \frac{J}{4}\right) a_- &= \frac{\Omega_R}{2}\Big(a_1 + a_2\Big) - \frac{J}{2} a_+, \qquad \left(\chi + \delta + \frac{J}{4}\right) a_2 = \frac{\Omega_R}{2}\Big(a_+ + a_-\Big),
\end{aligned} \tag{3.47}$$

where

$$\delta = \frac{1}{2}\Big(\omega_a + \omega_b\Big) - \omega_L, \tag{3.48}$$

and

$$\Delta = \frac{1}{2}\Big(\omega_a - \omega_b\Big). \tag{3.49}$$

The system, Eqs. (3.47), can be reduced to two coupled equations for the amplitudes $a_1$ and $a_2$, which read

$$\left[\tilde{\chi} + \Delta - \frac{J}{2} - \frac{\Omega_R^2}{2}\left(\frac{\tilde{\chi}}{\tilde{\chi}^2 - \delta^2}\right)\right] a_+ = \frac{1}{2}\left[\left(\frac{\tilde{\chi}}{\tilde{\chi}^2 - \delta^2}\right)\Omega_R^2 - J\right] a_-, \tag{3.50}$$

$$\left[\tilde{\chi} - \Delta - \frac{J}{2} - \frac{\Omega_R^2}{2}\left(\frac{\tilde{\chi}}{\tilde{\chi}^2 - \delta^2}\right)\right] a_- = \frac{1}{2}\left[\left(\frac{\tilde{\chi}}{\tilde{\chi}^2 - \delta^2}\right)\Omega_R^2 - J\right] a_+, \tag{3.51}$$

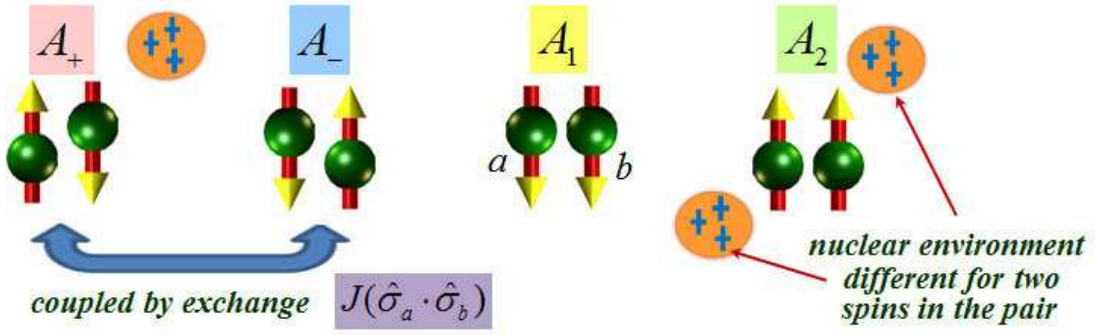


**Figure 3.16**: Schematic illustration of the spin states in the electron-hole bound carrier pair. The states $A_1$ and $A_2$ are coupled through exchange interaction, while the states $A_+$ and $A_-$ are coupled to $A_1$ and $A_2$ though spin Rabi oscillations.

where $\tilde{\chi} = \chi + \frac{1}{4}J$. It follows from Fig. 3.16 that there are four relevant states instead of three, as in the case of a quantum dot molecule. The implications of this is that their will be, in general, 6 peaks in the Fourier transform rather than 3 as we had before.

Note that the system Eqs.(3.50), (3.51) can be strongly simplified in the limiting case when $\Delta \ll J$. Neglecting $\Delta$, we find that the solutions get split into symmetric, $a_+ = a_-$, and antisymmetric, $a_+ = -a_-$. In the absence of driving, the four quasienergies are: $J$, 0, and $\pm\delta$. Only $\tilde{\chi} = J$ corresponds to $a_+ = -a_-$. Concerning three other quasienergies, at finite $\Omega_R$, they will transform to 0 and $\pm\sqrt{\delta^2 + \Omega_R^2}$. Then in the Fourier transform, we will have three peaks, two peaks at $\sqrt{\delta^2 + \Omega_R^2}$, and a third at $2\sqrt{\delta^2 + \Omega_R^2}$. In this sense, the limit of large $J$ reminds the situation in a quantum dot molecule.

Before proceeding further, it is instructive to analyze the limit $J = 0$, when the spin pairs are completely decoupled. Then the quasienergies, from Eqs. (3.50) and (3.51), can be easily solved for, which give

$$\tilde{\chi}_{1,2}^2 = \frac{1}{2}\left(\delta^2 + \Delta^2 + \Omega_R^2\right) + \sqrt{\frac{1}{4}\left(\delta^2 + \Delta^2 + \Omega_R^2\right)^2 - \delta^2\Delta^2}, \tag{3.52}$$

$$\tilde{\chi}_{3,4}^2 = \frac{1}{2}\left(\delta^2 + \Delta^2 + \Omega_R^2\right) - \sqrt{\frac{1}{4}\left(\delta^2 + \Delta^2 + \Omega_R^2\right)^2 - \delta^2\Delta^2}. \tag{3.53}$$

It is straightforward to find the peak positions in the Fourier transform. We find that there are four peaks,

$$f_1 = 2\tilde{\chi}_2, \qquad f_2 = \tilde{\chi}_2 - \tilde{\chi}_4, \qquad f_3 = \tilde{\chi}_2 + \tilde{\chi}_4, \qquad f_4 = 2\tilde{\chi}_4. \tag{3.54}$$

In the strong-driving limit, one peak, $f_1$, is close to $2\Omega_R$, while two peaks, $f_2$ and $f_3$, are split about $\Omega_R$, and the fourth peak is close to zero. Experimental results [30], shown in

Fig. 3.15, correspond to this weak $J$ limit. At strong driving, the presence of two peaks with positions $\Omega_R$ and $2\Omega_R$ is apparent from the plots. Note also that there appears to be a signature of a peak with position near zero. The actual experimental data are the result of averaging the distribution over $\Delta$ and $\delta$. This reflects the difference in random hyperfine fields acting on components of the pair. Overall, the shapes of the peaks at strong driving compare favorably with the shape calculated in the Preface and shown in Fig. 1.1: at least their asymmetries are in the same direction.

Eqs. (3.50), (3.51) predict that at weaker driving fields, the low-frequency $\Omega_R$ peak splits into two. This splitting, though, will not be seen in the experiment: it can be shown that two peaks will overlap upon averaging. It might seem that, as $\Omega_R$ increases, the role of disorder becomes progressively less. However, the separation between two central peaks also goes to zero with increasing $\Omega_R$.

Consider now the resonant condition, when $\delta = 0$. Then we have one quasienergy with $\tilde{\chi} = 0$ and three others that satisfy the cubic equation

$$\tilde{\chi}^2(\tilde{\chi} - J) - (\Delta^2 + \Omega_R^2)\tilde{\chi} + \Omega_R^2 J = 0. \tag{3.55}$$

We can now reduce Eq. (3.55) to the form Eq. (3.28) that we had for a quantum dot molecule. Then the expression for parameter $f$ for the two-spin system that replaces Eq. (3.29) acquires the form

$$f = -\frac{J\left[2J^2 + 9(\Delta^2 + 4\Omega_R^2)\right]}{\sqrt{27}\left[J^2 + 3(\Delta^2 + \Omega_R^2)\right]^{3/2}}. \tag{3.56}$$

We see that, in terms of dependence on $\Omega_R$, Eq. (3.56) has the same structure as Eq. (3.29). This immediately suggests that dependence $f(\Omega_R)$ has an extremum which leads to peculiar evolution of Fourier components of the Rabi oscillations with $\Omega_R$, uncovered above. Our main prediction for this system is that, in addition to the three peaks, which coincide with our prediction for a quantum dot molecule, $f_1 = \chi_1 - \chi_2$, $f_2 = \chi_3 - \chi_1$, and $f_3 = f_1 + f_2$, there will be three more peaks: $f_4 = \chi_1$, $f_5 = \chi_2$, $f_6 = \chi_3$.

In conclusion of this section, we would like to make connection of our results to Ref. [30], where the Fourier-transform components in a pair of bound carriers were simulated numerically. The results for different values of $\Delta$ and $\delta$ are plotted in Fig. 3.14. For each given, $\Delta$, the plots show the peak position (in the units of $\Omega_R$) versus $\delta$ (in the units of $\Omega_R$). The exchange, $J$, is kept the same for all plots. The most prominent feature of the numerical results is that different peaks have *opposite* slopes as a function of $\delta$.

This is consistent with our results. Although we studied the peak positions versus $\Omega_R$ instead of $\Delta$, it can be seen that the evolution of the peak positions can be understood from analyzing the parameter $f$ as a function of $\Delta$. See Eq. (3.56). This is because the evolution of $f$ with $\Delta$ will show similar behavior as it did with $\Omega_R$.

## 3.6 References


[1] L. Childress, M. V. Gurudev Dutt, J. M. Taylor, A. S. Zibrov, F. Jelezko, J. Wrachtrup, P. R. Hemmer, and M. D. Lukin, Science **314**, 281 (2006).

[2] R. Hanson, L. H. Willems van Beveren, I. T. Vink, J. M. Elzerman, W. J. M. Naber, F. H. L. Koppens, L. P. Kouwenhoven, and L. M. K. Vandersypen, Phys. Rev. Lett. **94**, 196802 (2005).

[3] X. Li, Y. Wu, D. Steel, D. Gammon, T. H. Stievater, D. S. Katzer, D. Park, C. Piermarocchi, and L. J. Sham, Science **301** 809 (2003).

[4] T. H. Stievater, X. Li, D. G. Steel, D. Gammon, D. S. Katzer, D. Park, C. Piermarocchi, L. J. Sham, Phys. Rev. Lett. **87**, 133603 (2001).

[5] H. Kamada, H. Gotoh, J. Temmyo, T. Takagahara, H. Ando, Phys. Rev. Lett. **87**, 246401 (2001).

[6] M. Bayer, P. Hawrylak, K. Hinzer, S. Fafard, M. Korkusinski, Z. R. Wasilewski, O. Stern, A. Forchel, Science **291**, 451 (2001).

[7] E. A. Stinaff, M. Scheibner, A. S. Bracker, I. V. Ponomarev, V. L. Korenev, M. E. Ware, M. F. Doty, T. L. Reinecke, D. Gammon, Science **311**, 636 (2006).

[8] A. Zrenner, E. Beham, S. Stufler, F. Findeis, M. Bichler, G. Abstreiter, Nature Phys. **418**, 612 (2002).

[9] H. Drexler, D. Leonard, W. Hansen, J. P. Kotthaus, and P. M. Petroff, Phys. Rev. Lett. **73**, 2252 (1994).

[10] A. Tackeuchi, T. Kuroda, K. Mase, Y. Nakata, N. Yokoyama, Phys. Rev. B **62**, 1568 (2000).

[11] Q. Q. Wang, A. Muller, P. Bianucci, E. Rossi, Q. K. Xue, T. Takagahara, C. Piermarocchi, A. H. MacDonald, C. K. Shih, Phys. Rev. B **72**, 035306 (2005).

[12] H. J. Krenner, M. Sabathil, E. C. Clark, A. Kress, D. Schuh, M. Bichler, G. Abstreiter, J. J. Finley, Phys. Rev. Lett. **94**, 057402 (2005).

[13] M. Scheibner, M. Yakes, A. S. Bracker, I. V. Ponomarev, M. F. Doty, C. S. Hellberg, L. J. Whitman, T. L. Reinecke, D. Gammon, Nature Phys. **4**, 291-5 (2008).

[14] L. Robledo, J. Elzerman, G. Jundt, M. Atatüre, A. Högele, S. Fält, A. Imamoglu, Science **320**, 772-5 (2008).

[15] M. F. Doty, J. I. Climente, M. Korkusinski, M. Scheibner, A. S. Bracker, P. Hawrylak, D. Gammon, Phys. Rev. Lett. **102**, 047401 (2009).

[16] Y. I. Mazur, V. G. Dorogan, D. Guzun, E. Marega, Jr., G. J. Salamo, G. G. Tarasov, A. O. Govorov, P. Vasa, C. Lienau, Phys. Rev. B **82**, 155413 (2010).

[17] H. Htoon, T. Takagahara, D. Kulik, O. Baklenov, A. L. Holmes, Jr., C. K. Shih, Phys. Rev. Lett. **88**, 087401 (2002).

[18] T. Unold, K. Mueller, C. Lienau, T. Elsaesser, A. D. Wieck, Phys. Rev. Lett. **94**, 137404 (2005).

[19] S. J. Boyle, A. J. Ramsay, A. M. Fox, M. S. Skolnick, A. P. Heberle, M. Hopkinson, Phys. Rev. Lett. **102**, 207401 (2009).

[20] M. Zecherle, C. Ruppert, E. C. Clark, G. Abstreiter, J.J. Finley, M. Betz, Phys. Rev. B **82**, 125314 (2010).

[21] S. Michaelis de Vasconcellos, S. Gordon, M. Bichler, T. Meier, A. Zrenner, Nature Photonics **4**, 545 - 548 (2010).

[22] D. Kim, S. G. Carter, A. Greilich, A. S. Bracker, and D. Gammon, Nature Phys. **7**, 223 (2011).

[23] K. Müller, A. Bechtold, C. Ruppert, M. Zecherle, G. Reithmaier, M. Bichler, H. J. Krenner, G. Abstreiter, A. W. Holleitner, J. M. Villas-Bôas, J. J. Finley, ArXiv:1111.3137 (2011).

[24] J. M. Villas-Bôas, S. E. Ulloa, A. O. Govorov, Phys. Rev. Lett. **94**, 057404 (2005).

[25] J. E. Rolon, S. E. Ulloa, Phys. Rev. B **82**, 115307 (2010).

[26] H. S. Borges, L. Sanz, J. M. Villas-Bôas, A. M. Alcalde, Phys. Rev. B **81**, 075322 (2010).

[27] V. Rajevac, C. Boehme, C. Michel, A. Gliesche, K. Lips, S. D. Baranovskii, and P. Thomas, Phys. Rev. B **74**, 245206 (2006).

[28] A. Gliesche, C. Michel, V. Rajevac, K. Lips, S. D. Baranovskii, F. Gebhard, and C. Boehme, Phys. Rev. B **77**, 245206 (2008).

[29] C. Michel, A. Gliesche, S. D. Baranovskii, K. Lips, F. Gebhard, and C. Boehme, Phys. Rev. B **79**, 052201 (2009).

[30] D. R. McCamey, K. J. van Schooten, W. J. Baker, S.-Y. Lee, S.-Y. Paik, J. M. Lupton, and C. Boehme, Phys. Rev. Lett. **104**, 017601 (2010).

[31] R. H. Dicke, Phys. Rev. **93**, 99 (1954).

# PART II

# INTERPLAY OF SPIN-ORBIT COUPLING AND ZEEMAN SPLITTING IN ALTERNATING CURRENT ABSORPTION IN LOW-DIMENSIONAL SYSTEMS

## 4.1 Preface

In the next two chapters, we study a single-particle ac phenomenon of spin resonance in a system of two-dimensional fermions. Spin resonance is simply the resonant absorption of an ac field between Zeeman-split levels. If the resonance is excited by an electric field component of light, then absorption is possible only in the presence of spin-orbit coupling. In all previous studies of this phenomenon, spin-orbit coupling was assumed to be vanishingly small and was treated perturbatively. Correspondingly, the absorption line had a shape of a single $\delta$-peak.

In chapter I, we study what happens when the spin-orbit coupling strength is finite. We demonstrate that there is a nontrivial interplay between Zeeman splitting, $\Delta_Z$, and spin-orbit coupling, $\Delta_{SO}$. In the spectrum, the absorption line acquires a finite width, and its shape becomes highly anisotropic. The behavior of the absorption coefficient near the absorption edges is singular. A peculiar situation arises near the "compensation" condition where $\Delta_Z$ and $\Delta_{SO}$ have nearly equal magnitudes. In the vicinity of this condition, the Fermi surface of electron gas undergoes a strong restructuring. This restructuring is reflected in a nontrivial shape of the absorption line. We show that at $\Delta_Z = \Delta_{SO}$, the electron gas can absorb the ac field of a very low frequency. Moreover, we demonstrate that the absorption lineshape evolves with increasing temperature in a nontrivial fashion, namely, the peak position keeps moving with temperature towards high frequencies even if the temperature is comparable to the Fermi energy, which is quite unusual. The analysis is enabled by the fact that in the presence of both spin-orbit coupling and Zeeman splitting, the energy spectrum can be found analytically.

In the second chapter, we generalized the theory of absorption in a parallel magnetic field and in the presence of spin-orbit coupling to a quantum wire. In this case, without spin-orbit coupling, the absorption spectrum consists of several discrete lines corresponding to different size-quantization subbands. Weak spin orbit coupling introduces finite widths of these lines and, in higher order, allows the absorption between Zeeman-split components of size-quantization subbands. Capturing these effects analytically, for arbitrary confining potential, requires "gauging out" of the spin-orbit term in the Hamiltonian before the perturbation theory with respect to $\Delta_{SO}$ is developed. Gauge transformation adds a "spin-orbit phase" to the size-quantization wave functions.

For strong enough spin-orbit coupling, we again focus on the condition $\Delta_{SO} = \Delta_Z$, which is now satisfied simultaneously for all subbands. We demonstrate that the low-frequency part of the absorption spectrum in the wire near this condition is universal,

i.e., it does not depend on the form of the confining potential. To analyze the absorption in the wire in the entire frequency range and for arbitrary spin-orbit coupling strength, we considered a particular example of rigid-walls confinement, where the subband's dispersion laws and the corresponding wave functions can be found analytically. Interestingly, the wave functions are combinations of *four* components, two of which oscillate between the boundaries, while the other two *decay* away from the boundaries.

# CHAPTER 5

# INTERPLAY OF SPIN-ORBIT COUPLING AND ZEEMAN SPLITTING IN THE ABSORPTION LINESHAPE OF 2D FERMIONS

## 5.1 Introduction

In a spin system with isotropic exchange, the absorption spectrum of an ac magnetic field is a $\delta$-peak at $\omega = \Delta_Z$, where $\Delta_Z$ is the Zeeman splitting, independently of the exchange interaction strength [1]. Similarly to the Kohn theorem for cyclotron resonance [2], this fact is the consequence of coupling of a spatially homogeneous exciting field to the center of mass of the system. Therefore, any deviation of the absorption spectrum from the $\delta$-shape implies a violation of the spin-rotation symmetry, which is either due to anisotropic terms in the Hamiltonian or due to development of spontaneous ordering below critical temperature.

The subject of the present paper is the shape of the absorption in the spin-liquid ground state [3] of the frustrated antiferromagnet in the presence of Dzyaloshinskii-Moriya (DM) interaction, which originates from the spin-orbit interaction in the underlying system of electrons [4, 5]. We find that electron spin resonance (ESR), which measures the ac absorption, can be used to probe the fractionalized spinon excitations. Specifically, we assume that the ground state of the frustrated spin system is described by the Fermi sea of the neutral spin excitations (spinons). Emergence of the Fermi sea of neutral excitations is at the core of the RVB state proposed by Anderson 25 years ago [6, 7]. Recently, the spin liquid state with spinon Fermi surface was found for the half-filled Hubbard model on a triangular lattice [9, 8] for intermediate $U/t$ values.

Dzyaloshinskii-Moriya interaction that gives a nontrivial shape to the spin resonance is most conveniently introduced into the Hubbard model via a spin-dependent hopping term

$$H = \sum_{i,j} \{c^{+}_{i,\alpha}(-t\delta_{\alpha\beta} + i\vec{\lambda}_{ij} \cdot \vec{\hat{s}}_{\alpha\beta})c_{j,\beta} + \text{h.c.}\} + U \sum_{i} n_{i\uparrow} n_{i\downarrow}. \tag{5.1}$$

Here $2\vec{\hat{s}}$ is the vector of Pauli matrices, $\alpha$ and $\beta$ are spin indices, and $\vec{\lambda}_{ij}$ is the DM vector on the link $(ij)$. The first $(t)$ and the last $(U)$ terms are responsible for the Fermi surface formation. Here we argue that, in course of reduction of these terms to the Hamiltonian of spinons, as outlined below, the second term in Eq. (5.1) generates a term in the spinon Hamiltonian which has a form of spin-orbit coupling familiar from 2D electron gas in semiconductor structures [10]. Technically, the reduction is achieved with the help of the slave-rotor technique [11, 12, 13] where the spinon inherits spin of the electron $c_{i,\alpha}$ while the rotor variable $e^{i\theta_i}$ inherits its charge, $c_{i,\alpha} = f_{i,\alpha}e^{i\theta_i}$. The phase with a condensate of charge rotor $\langle e^{i\theta}\rangle \neq 0$ is the usual metallic phase while the one with no such condensate represents a Mott phase where the charge degrees of freedom are gapped. Importantly, spin excitations of this phase are neutral spinons $f_{i,\alpha}$ forming a Fermi-liquid state. This reasoning suggests that the minimal model for gapless spinons is given by the noninteracting part of (5.1) where hopping $t$ and spin-orbit coupling $\lambda$ should be viewed as effective parameters renormalized by gapped charge fluctuations which are controlled by the Hubbard $U$ term (the notion that spinons can be treated as neutral fermions [9, 8, 14, 15] has an important caveat that they interact strongly with the emerging gauge field [16, 13]).

Regarding the DM term in Eq. (5.1), we focus on the case of *uniform* spin-orbit interaction $\vec{\lambda}_{i,j} = \lambda\hat{n} \times (\vec{r}_i - \vec{r}_j)$. Here vectors $\vec{r}_{i,j}$ denote nearest-neighbor lattice sites and $\hat{n} = \hat{z}$ is normal to the plane. Note in passing that, for a square lattice, precisely this arrangement is known to realize in, e.g., $YBa_2Cu_3O_{6+x}$ [17, 18, 19]. For the chosen form of spin-orbit interaction, the DM term of (5.1) assumes the form

$$\hat{H}_{SO}(\mathbf{k}) = -2\lambda \sum_{k} c^{\dagger}_{k,\alpha}\{\hat{s}_x \sin[k_y] - \hat{s}_y \sin[k_x]\}c_{k,\beta}. \tag{5.2}$$

One can recognize in Eq. (5.2) the lattice version of the celebrated Rashba spin-orbit term [20, 10] in the Hamiltonian of the 2D electron gas.

It is also quite natural that the magnetic field couples to spinons via the Zeeman interaction. In fact, the magnetic field also couples to the orbital motion of spinons via the higher order closed loop processes [21] ($\propto t^3/U^2$ for triangular lattice, for example). For the sake of argument, we do not consider these processes here: for example, "orbital"

coupling is absent in geometry where the magnetic field is parallel to the two-dimensional layer.

We thus see that under the assumptions made, the Hamiltonian of a strongly interacting Fermi system (5.1) in the spin-liquid phase (so that $\langle e^{i\theta} \rangle = 0$) maps onto that of (spinon) Fermi gas with spin-orbit interaction of the Rashba type. Hence, the basic features of the ESR response in an exotic spin liquid state can be captured within a much simpler model of two-dimensional electron gas subject to spin-orbit interaction. Surprisingly, despite several decades of intensive research in the latter area, we are not aware of the calculation of ESR response in two-dimensional electron gas subject to both spin-orbit and Zeeman interactions.

In earlier studies of spin-orbit coupled two-dimensional electron gas the combined effect of Zeeman field and spin-orbit interaction was considered in relation to electric dipole spin resonance [22] (EDSR), which is the absorption of the ac electric field between the Zeeman-split levels. Obviously, it is spin-orbit interaction which allows this absorption to occur, since it couples the electron spin to the electric field. In theoretical papers [23, 24] on EDSR in two-dimensional electron gas a spin-orbit term of the form Eq. (5.2) in the small-$\mathbf{k}$ limit was added to the Hamiltonian of free electrons. Then the matrix element of transition between two spin levels was calculated for different orientations of magnetic field. However, we cannot use the results of Refs. [23, 24] for finding the lineshape of ESR. This is because in these papers it was assumed that the magnitude, $\Delta_{SO}$, of the spin-orbit term is much smaller than the Zeeman splitting, $\Delta_Z$, so that $\Delta_{SO}$ was treated perturbatively. As a result, in the absence of disorder, the lineshape of the resonance was simply a $\delta$-peak. The natural basis in which the magnitude of this peak is calculated [23, 24] is the basis of spin projections on the applied magnetic field.

Another group of relevant earlier papers [25, 26] dealt with the phenomenon of chiral resonance, which takes place when $\Delta_{SO}$ is finite. In this case spin-orbit term splits the free-electron spectrum into two branches, separated by $\Delta_{SO}$, which correspond to different chiralities. Then the dipole absorption of the ac electric field between the branches is allowed. The absorption spectrum of the chiral resonance has a box-like shape [26] centered at $\omega = \Delta_{SO}$ with a width of the order of $\Delta_{SO}^2/E_F$, where $E_F$ is the Fermi energy. The absorption is calculated in a natural basis of spinors, describing opposite chiralities. Still, we cannot use the results of Refs. [25, 26] for calculating the ESR lineshape, since magnetic field was assumed zero in these papers. Instead, we will adopt the general approach of Ref. [26] to the calculation of the ac response. This approach is

based on the calculation of the *optical conductivity*. We will subsequently demonstrate that the ESR lineshape can be expressed through the optical conductivity in a simple way.

The outline of the paper is as follows. Calculation of the optical conductivity for arbitrary relation between $\Delta_{SO}$ and $\Delta_Z$, is presented in Sect. II of the present paper. In Sect. III. the results of this calculation are used to find the ESR lineshape for different orientations of the ac magnetic field.

Normally, $\sigma(\omega)$ is a peak with two sharp edges, which are imposed by the energy conservation, as illustrated in Fig. 5.1. Notably, we demonstrate that $\sigma(\omega)$ exhibits a singular behavior near these edges. The character of singularities is different for the ac field parallel and perpendicular to the external in-plane magnetic field. We trace how these singularities are smeared out upon increasing the temperature, $T$.

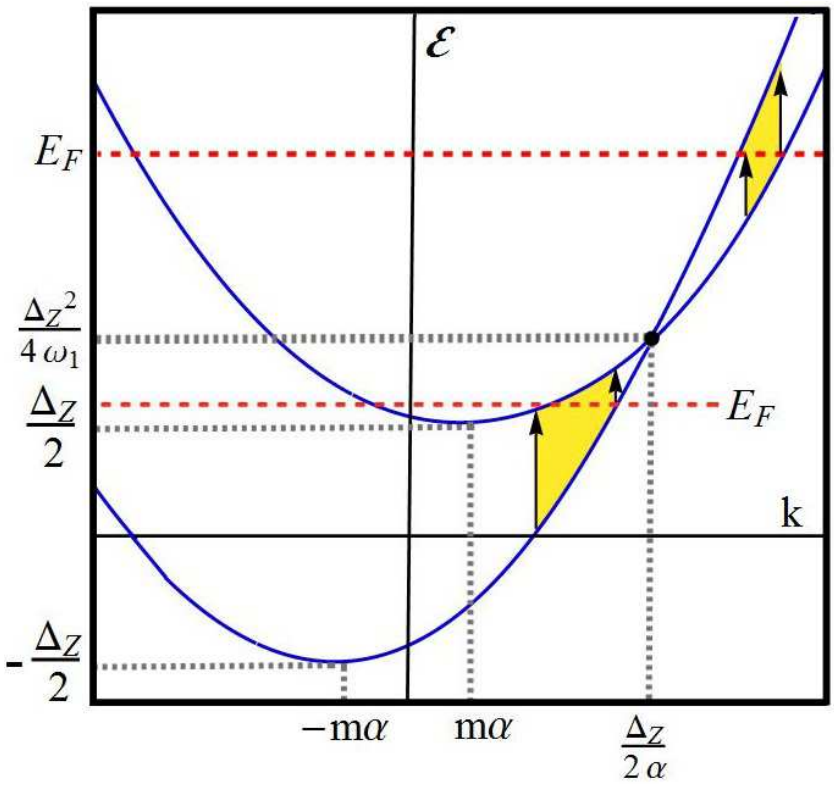


**Figure 5.1**: Energy dispersion of two subbands in the presence of Zeeman splitting and spin-orbit coupling are plotted from Eq. (5.5). The curves cross at $k_x = \Delta_Z/2\alpha$. Yellow regions designate the momenta of the states taking part in absorption. For Fermi-level position $E_F = \Delta_Z^2/4\omega_1$, where $\omega_1 = 2m\alpha^2$, there is no threshold for absorption.

The most nontrivial behavior of $\sigma(\omega)$ corresponds to the situation $\Delta_Z = \Delta_{SO}$, when Zeeman splitting is "compensated" by the spin-orbit splitting along the direction of the magnetic field. As a result of this compensation, the two branches of the electron spectrum, $\mathcal{E}^{(1)}(\mathbf{k})$ and $\mathcal{E}^{(2)}(\mathbf{k})$, cross each other at a certain momentum $\mathbf{k} = (k_0, 0)$ while the Fermi level $E_F = \mathcal{E}^{(1)}(\mathbf{k}) = \mathcal{E}^{(2)}(\mathbf{k})$ is located at the point of crossing, as illustrated in Fig. 5.1. The underlying reason why the shape of $\sigma(\omega)$ is peculiar near the condition $\Delta_Z = \Delta_{SO}$ is the following.

As the difference $\Delta_Z - \Delta_{SO}$ changes sign, the Fermi surfaces $\mathcal{E}^{(1)}(\mathbf{k}) = E_F$ and $\mathcal{E}^{(2)}(\mathbf{k}) = E_F$ undergo rapid restructuring. This restructuring is illustrated in Figs. 5.2 and 5.3. Since the states responsible for absorption lie between the two Fermi points, see Fig. 5.1, in the vicinity of $\Delta_Z = \Delta_{SO}$, the absorption remains finite at low frequencies $\omega \ll \Delta_Z$. We will show that in this regime, the absorption spectrum exhibits features that evolve with temperature, even when $T$ is comparable to the Fermi energy.

## 5.2 Optical conductivity with finite $\Delta_Z$ and $\Delta_{SO}$

### 5.2.1 Hamiltonian and eigenfunctions

Assume that electrons are confined to the $(x, y)$ plane, while the magnetic field, creating the splitting, $\Delta_Z$, is directed along the $y$-axis. For concreteness, we choose

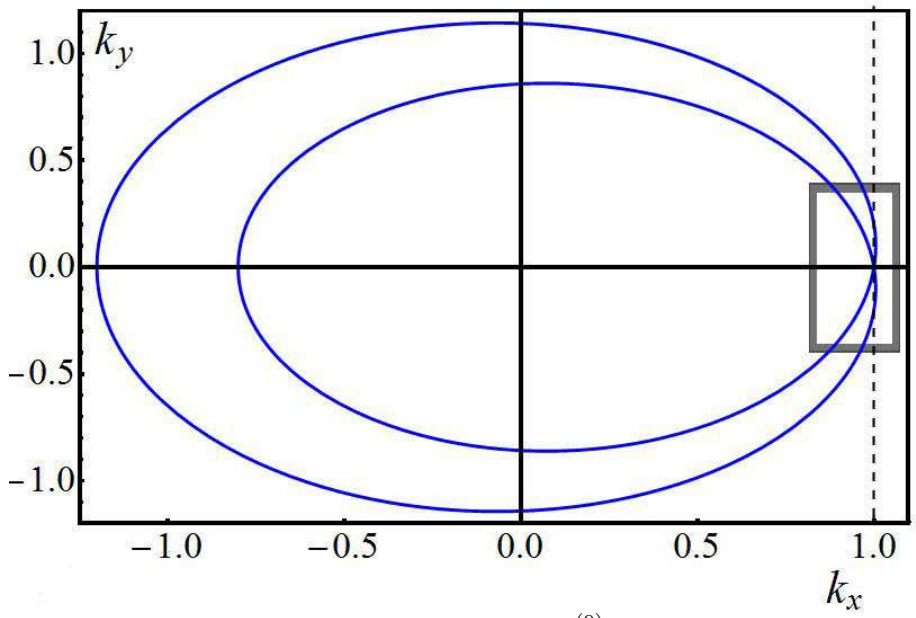


**Figure 5.2**: Two Fermi surfaces corresponding to $E_F^{(0)} = \Delta_Z^2/4\omega_1$ and $\omega_1/\Delta_Z = 0.1$ are plotted from Eq. (5.29), where the projections of momenta $k_x$ and $k_y$ are in the units $\Delta_Z/2\alpha$.

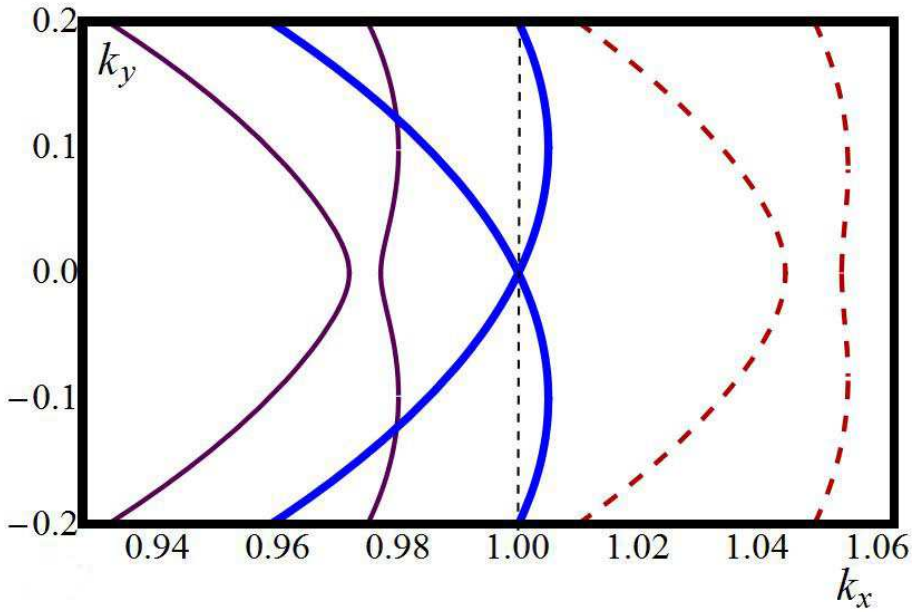


**Figure 5.3**: Evolution of the Fermi surfaces near the point $k_y = 0$ for different $E_F$ (enclosed by the gray box in Fig. 5.2): (thin line) $E_F = 0.95E_F^{(0)}$, (thick line) $E_F = E_F^{(0)}$, (dashed line) $E_F = 1.1E_F^{(0)}$.

the Rashba-type [20, 10] form of spin-orbit coupling

$$\hat{H}_{SO}(\mathbf{k}) = 2\alpha(k_x\hat{s}_y - k_y\hat{s}_x), \tag{5.3}$$

where $\alpha$ is the spin-orbit constant. In the matrix form, the Hamiltonian of the system reads

$$\hat{H} = \begin{pmatrix} \frac{\hbar^2}{2m}(k_x^2+k_y^2) & i\frac{\Delta_Z}{2} - \alpha(ik_x + k_y) \\ -i\frac{\Delta_Z}{2} - \alpha(-ik_x + k_y) & \frac{\hbar^2}{2m}(k_x^2+k_y^2) \end{pmatrix}, \tag{5.4}$$

where $m$ is the effective mass (we set $\hbar = 1$ throughout the paper). The two branches of the spectrum and corresponding spinors are given by

$$\mathcal{E}_{\mathbf{k}}^{1(2)} = \frac{k^2}{2m} \pm \sqrt{\alpha^2 k_y^2 + \left(\alpha k_x - \frac{\Delta_Z}{2}\right)^2}, \tag{5.5}$$

$$u_{\mathbf{k}}^{(1),(2)} = \frac{1}{\sqrt{2}} \begin{pmatrix} \frac{\alpha(ik_x+k_y)-i\frac{\Delta_Z}{2}}{\frac{k^2}{2m}-\mathcal{E}_{\mathbf{k}}^{1(2)}} \\ 1 \end{pmatrix}. \tag{5.6}$$

To express the optical conductivity in terms of the spectrum Eq. (5.5) and eigenfunctions Eq. (5.6), one has to add to the Hamiltonian Eq. (5.4) the term

$$\hat{H}_{int}^{e} = e\mathbf{E}\cdot\boldsymbol{\rho}\cos\omega t, \tag{5.7}$$

where **E** is the external electric field, and calculate the ac current. This calculation is not straightforward because the eigenfunctions from different branches corresponding to the *same* momentum are orthogonal to each other. For this reason, it is much more convenient to adopt the approach of Ref. [27]. Within this approach, the system response to the scalar perturbation

$$V^e(\boldsymbol{\rho},t) = V_0\cos(\omega t - \mathbf{q}\cdot\boldsymbol{\rho}), \tag{5.8}$$

with finite wave vector, $\mathbf{q}$, is studied. The energy absorption rate, $I(\mathbf{q})$, caused by this perturbation, is calculated using the Golden rule. The optical conductivity at finite $\mathbf{q}$ is related to $I(\mathbf{q})$ as follows

$$\sigma(\mathbf{q},\omega) = \frac{\big(1-e^{-\omega/T}\big)I(\mathbf{q})}{2V_0^2q^2}, \tag{5.9}$$

where $\exp(-\omega/T)$ accounts for the emission processes. The static limit $\mathbf{q}\to 0$ is taken only at the final step, yielding

$$\sigma(\omega) = \pi e^2\big(1-e^{-\omega/T}\big)\lim_{\mathbf{q}\to 0}\left(\frac{\omega}{q^2}\right)\sum_{\mathbf{k}}\big|\langle u^{(1)}_{\mathbf{k}}|u^{(2)}_{\mathbf{k}+\mathbf{q}}\rangle\big|^2\delta\big(\mathcal{E}^{(2)}_{\mathbf{k}+\mathbf{q}}-\mathcal{E}^{(1)}_{\mathbf{k}}-\omega\big)\Big[1-f\big(\mathcal{E}^{(2)}_{\mathbf{k}+\mathbf{q}}\big)\Big]f\big(\mathcal{E}^{(1)}_{\mathbf{k}}\big), \tag{5.10}$$

where $f(\mathcal{E}) = \Big\{1+\exp[(\mathcal{E}-E_F)/T]\Big\}^{-1}$ is the Fermi distribution.

The formal reason why absorption of the ac field is permitted in the presence of spin-orbit coupling is that, at small $\mathbf{q}$, the product $\langle u^{(1)}_{\mathbf{k}}|u^{(2)}_{\mathbf{k}+\mathbf{q}}\rangle$ is a linear function of $\mathbf{q}$, as readily follows from Eq. (5.6)

$$\langle u^{(1)}_{\mathbf{k}}|u^{(2)}_{\mathbf{k}+\mathbf{q}}\rangle = i\Big(\frac{\alpha}{2}\Big)\frac{(\alpha k_x-\frac{1}{2}\Delta_Z)q_y-\alpha k_yq_x}{(\alpha k_x-\frac{1}{2}\Delta_Z)^2+\alpha^2k_y^2}, \tag{5.11}$$

so that the combination, $|\langle u^{(1)}_{\mathbf{k}}|u^{(2)}_{\mathbf{k}+\mathbf{q}}\rangle|^2/q^2$, remains finite in the limit of $\mathbf{q}\to 0$. In subsequent sections, we analyze Eq. (5.10), first at $T=0$, and then at finite temperatures.

### 5.2.2 Optical conductivity at $T = 0$

It follows from Eq. (5.11) that at finite Zeeman splitting, the optical conductivity is highly anisotropic. For polarization perpendicular to the magnetic field, vector $\mathbf{q}$ is directed along the $x$-axis. Substituting Eq. (5.11) into Eq. (5.10), and converting the sum into an integral in polar coordinates, we get

$$\sigma_\perp(\omega) = \left(\frac{e^2\alpha^4\omega}{16\pi}\right)\int dkk^3\int\frac{d\phi}{\Omega(\phi)^4}\sin^2\phi\;\delta\big(2\Omega(\phi)-\omega\big)$$

$$\times\Theta\left(\frac{k^2}{2m}+\Omega(\phi)-E_F\right)\Theta\left(E_F-\frac{k^2}{2m}+\Omega(\phi)\right), \tag{5.12}$$

where we have introduced the notation

$$\Omega(\phi)=\sqrt{\alpha^2k^2-\alpha\Delta_Z k\cos\phi+\frac{\Delta_Z^2}{4}}. \tag{5.13}$$

The factor $\Omega(\phi)^{-4}$ in the integrand emerges from the denominator in the product $\langle u^{(1)}_{\mathbf{k}}|u^{(2)}_{\mathbf{k+q}}\rangle$, see Eq. (5.11). The numerator in this product is proportional to $k_y$, giving rise to $\sin^2\phi$ in the integrand. It is convenient to first perform the angular integration in Eq. (5.12) with the help of the $\delta$-function. Then the remaining integral over $k$ can be cast in the form

$$\sigma_\perp(\omega)=\left(\frac{e\,\alpha}{\sqrt{\pi}\,\omega\,\Delta_Z}\right)^2\int\limits_{\sqrt{m(2E_F-\omega)}}^{\sqrt{m(2E_F+\omega)}}dk\,k\left[\alpha^2k^2\Delta_Z^2-\left(\alpha^2k^2+\frac{\Delta_Z^2}{4}-\frac{\omega^2}{4}\right)^2\right]^{1/2}. \tag{5.14}$$

Integration in Eq. (5.14) can be performed explicitly, yielding

$$\begin{aligned}\sigma_\perp(\omega) &= \left(\frac{e^2}{8\pi}\right)\int_{r_i}^{r_f}dr\sqrt{1-r^2}\\ &= \left(\frac{e^2}{16\pi}\right)\left(\arcsin r+r\sqrt{1-r^2}\right)\Bigg|_{r_i}^{r_f}.\end{aligned} \tag{5.15}$$

The limits of integration in Eq. (5.15) are given by

$$r_{f,i}(\omega)=\frac{1}{2\Delta_Z\omega}(\Delta_{SO}^2-\omega^2\pm2\omega_1\omega-\Delta_Z^2), \tag{5.16}$$

where the frequency $\omega_1$ is defined as

$$\omega_1=2m\alpha^2=\frac{\Delta_{SO}^2}{4E_F}. \tag{5.17}$$

Expression Eq. (5.15) is valid when both $r_i$, $r_f$ lie within interval $-1<r_i,r_f<1$. For frequencies at which both $r_i$ and $r_f$ are outside this interval, we have $\sigma_\perp(\omega)\equiv 0$. When only one of the limits, say $r_f$, is outside the interval, one should set $r_f=1$ in Eq. (5.15).

For polarization parallel to the magnetic field, the calculation of conductivity is completely similar to the calculation of $\sigma_\perp(\omega)$. The only difference is in the product, $\langle u^{(1)}_{\mathbf{k}}|u^{(2)}_{\mathbf{k+q}}\rangle$, which, for $\mathbf{q}$ directed along $y$, is proportional to $(\alpha k_x-\Delta_Z/2)$. In polar coordinates, this factor leads to replacement of $\sin^2\phi$ in the integrand of Eq. (5.12) by $(\cos\phi-\Delta_Z/\alpha k)^2$. As a result, instead of Eq. (5.15), the momentum integration reduces to

$$\sigma_\parallel(\omega)=\left(\frac{e^2}{8\pi}\right)\int_{r_i}^{r_f}dr\frac{r^2}{\sqrt{1-r^2}}$$

$$= \left(\frac{e^2}{16\pi}\right)\left(\arcsin r - r\sqrt{1-r^2}\right)\Bigg|_{r_i}^{r_f}. \tag{5.18}$$

Equations (5.15) and (5.18) constitute our main results. We start their analysis from the limiting cases $\Delta_{SO} \gg \Delta_Z$ and $\Delta_{SO} \ll \Delta_Z$.

#### 5.2.2.1 $\Delta_{SO} \gg \Delta_Z$

It is instructive to trace how the shape of the chiral resonance emerges from Eqs. (5.15), (5.18). Taking the limit $\Delta_Z \to 0$, we find that $r_i$ and $r_f$ should be set to $-1$ and 1, respectively, for $\omega$ within the interval $|\omega - \Delta_{SO}| < \omega_1$. Outside of this interval, we have $r_i = r_f = \pm 1$ and the absorption is zero. This yields the lineshape

$$\sigma(\omega) = \left(\frac{e^2}{16}\right)\Theta\left[1 + \left(\frac{\omega^2 - \Delta_{SO}^2}{2\omega\omega_1}\right)\right]\Theta\left[1 - \left(\frac{\omega^2 - \Delta_{SO}^2}{2\omega\omega_1}\right)\right], \tag{5.19}$$

with sharp ends, which can be further simplified by introducing $\delta\omega = \omega - \Delta_{SO}$ and taking into account that $\omega_1 \ll \Delta_{SO}$. Then we reproduce the result of Refs. [26, 28]

$$\sigma(\delta\omega) = \frac{e^2}{16}\,\Theta\left(1 - \frac{|\delta\omega|}{\omega_1}\right), \tag{5.20}$$

where $\Theta(x)$ is the step-function.

Next we study how a small Zeeman splitting, $\Delta_Z \ll \omega_1$, smears the steps at $\omega - \Delta_{SO} = \pm\omega_1$. Introducing dimensionless deviation from the right boundary

$$\eta(\omega) = \frac{(\Delta_{SO} - \omega + \omega_1)}{\Delta_Z}, \tag{5.21}$$

we get the following behavior of $\sigma_\perp$, $\sigma_\parallel$ near the right boundary

$$\sigma_{\perp,\parallel} = \left(\frac{e^2}{16\pi}\right)\left[\frac{\pi}{2} - \arcsin\eta(\omega) \mp \eta(\omega)\sqrt{1-\eta^2(\omega)}\right]. \tag{5.22}$$

This behavior is illustrated in Fig. 5.4. We see that a step at $\delta\omega = \omega_1$ extends, at finite $\Delta_Z$, over an interval $\delta\omega - \omega_1 = \pm\Delta_Z$. Optical conductivity is strongly anisotropic within this interval. In particular, $\sigma_\parallel$ has a zero slope at the center of the interval. As $\Delta_Z$ exceeds $\omega_1$, the flat top in optical conductivity disappears completely.

#### 5.2.2.2 $\Delta_Z \gg \Delta_{SO}$

Consider now the EDSR limit of strong Zeeman splitting, $\Delta_Z \gg \Delta_{SO}$. Then Eqs. (5.15), (5.18) reduce to

$$\sigma_\perp(\omega) = \left(\frac{\sqrt{2}e^2}{4\pi}\right)\left(\frac{\omega_1}{\Delta_Z}\right)\left[\frac{\Delta_{SO}^2 - (\omega - \Delta_Z)^2}{2\Delta_Z\omega}\right]^{1/2}, \tag{5.23}$$

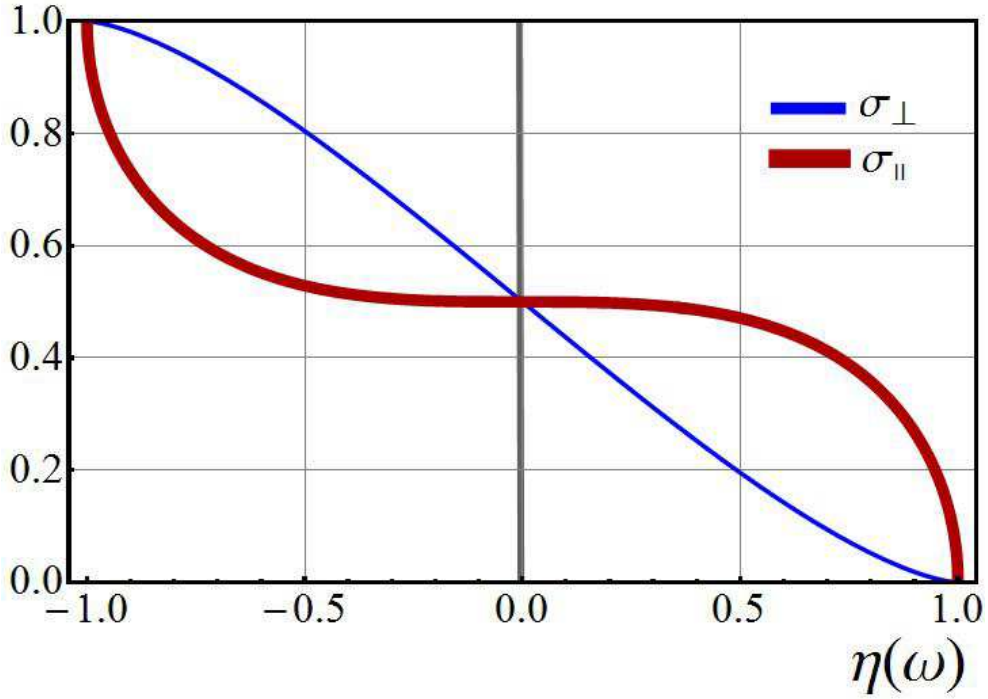


**Figure 5.4**: Smearing of the right edge of the chiral resonance at small $\Delta_Z \ll \omega_1$ is plotted from Eq. (5.22) as a function of dimensionless deviation, $\eta(\omega)$, Eq. (5.21), from the boundary. $\sigma_\parallel$ and $\sigma_\perp$ are plotted in the units $e^2/16$.

$$\sigma_\parallel(\omega) = \left(\frac{e^2}{4\sqrt{2}\pi}\right)\left(\frac{\omega_1}{\Delta_Z}\right)\left[\frac{\Delta_{SO}^2 - (\omega-\Delta_Z)^2}{2\Delta_Z\omega}\right]^{-1/2}. \tag{5.24}$$

The fact that the EDSR spectrum is confined to the interval $|\omega - \Delta_Z| < \Delta_{SO}$ could be expected on general grounds. It is also natural that optical conductivity is proportional, via $\omega_1$, to the square of the SO coupling strength. Less trivial is the fact that EDSR absorption is highly anisotropic, so that $\sigma_\perp$ turns to zero at the edges, while $\sigma_\parallel(\omega)$ exhibits a divergence near the edges. This can be seen in Fig. 5.5.

#### 5.2.2.3 $\Delta_Z \sim \Delta_{SO}$

Consider now the intermediate regime when $\Delta_Z$ and $\Delta_{SO}$ are of the same order. Since we assumed that Fermi energy is bigger than both $\Delta_Z$ and $\Delta_{SO}$, the condition $\Delta_Z \sim \Delta_{SO}$ automatically implies that both $\Delta_Z$ and $\Delta_{SO}$ are much bigger than $\omega_1$. Then the integrands in Eqs. (5.15), (5.18) can simply be multiplied by $r_f - r_i = 2\omega_1/\Delta_Z$, yielding

$$\sigma_\perp(\omega) = \left(\frac{e^2}{8\pi}\right)\frac{2\omega_1}{\Delta_Z}\sqrt{1-r^2(\omega)}, \tag{5.25}$$

$$\sigma_\parallel(\omega) = \left(\frac{e^2}{8\pi}\right)\frac{2\omega_1}{\Delta_Z}\frac{r^2(\omega)}{\sqrt{1-r^2(\omega)}}, \tag{5.26}$$

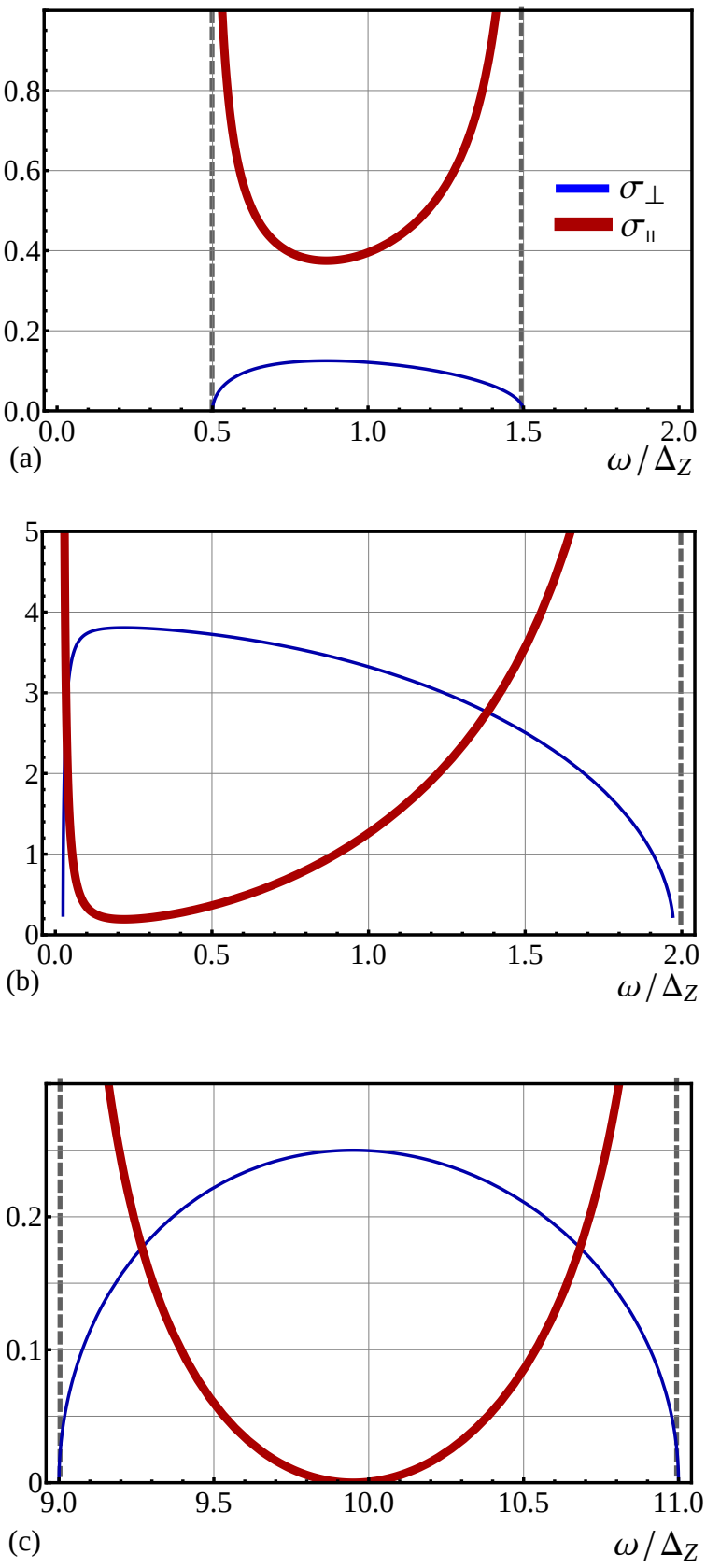


**Figure 5.5**: Optical conductivity at zero temperature, Eqs. (5.25), (5.26) vs. dimensionless frequency, $\omega/\Delta_Z$, are plotted in the units $(e^2/\pi)(\omega_1/\Delta_Z)$, for three values of the ratio $\Delta_{SO}/\Delta_Z$. (a) $\Delta_{SO}/\Delta_Z = 0.5$, Zeeman splitting dominates. (b) Zeeman and SO splitting nearly "compensate" each other, $\Delta_{SO}/\Delta_Z = 0.99$. (c) $\Delta_{SO}/\Delta_Z = 10$, SO splitting dominates.

where

$$r(\omega) = \frac{1}{2\Delta_Z \omega}(\Delta_{SO}^2 - \omega^2 - \Delta_Z^2), \tag{5.27}$$

is given by Eq. (5.16) with $\omega_1 = 0$. It is seen that $\sigma_\perp$ monotonically grows with $r^2$, while $\sigma_\parallel$ monotonically decreases with $r^2$. At the same time, the *frequency* dependencies of $\sigma_\perp$ and $\sigma_\parallel$ are strongly nonmonotonic. Firstly, for $\Delta_{SO} > \Delta_Z$, $r(\omega)$ turns to zero at $\omega = \omega_0 = (\Delta_{SO}^2 - \Delta_Z^2)^{1/2}$. A zero in $\sigma_\parallel$ is accompanied by a maximum in $\sigma_\perp$. For the opposite relation, $\Delta_Z > \Delta_{SO}$, there is a minimum in $r^2(\omega)$ at $\omega = \tilde{\omega_0} = (\Delta_Z^2 - \Delta_{SO}^2)^{1/2}$.

This minimum translates into a minimum in $\sigma_\parallel(\omega)$ and a maximum in $\sigma_\perp(\omega)$. The behaviors of $\sigma_\parallel(\omega)$ and $\sigma_\perp(\omega)$ for different relations between $\Delta_Z$ and $\Delta_{SO}$ are illustrated in Fig. 5.5.The most interesting behavior of optical conductivity takes place near the point of "compensation", where $\Delta_Z$ and $\Delta_{SO}$ are close to each other. Then the minimum in $\sigma_\parallel$ and the maximum in $\sigma_\perp$ become very sharp. This implies that absorption becomes possible at very low frequencies. On the physical level, the low-frequency absorption is the result of crossing of the Fermi surfaces $\mathcal{E}^{(1)}(\mathbf{k}) = E_F$ and $\mathcal{E}^{(2)}(\mathbf{k}) = E_F$, see Fig. 5.1, which takes place at $\Delta_Z = \Delta_{SO}$. The Fermi energy is equal to

$$E_F^{(0)} = \frac{\Delta_Z^2}{4\omega_1} \tag{5.28}$$

at the point of crossing. As the difference $\Delta_Z - \Delta_{SO}$ increases, the Fermi surfaces undergo restructuring. In Fig. 5.3, we show the evolution of the Fermi surfaces

$$E_F = \frac{1}{2m}\left(k_x^2 + k_y^2\right) \pm \sqrt{\alpha^2 k_y^2 + \left(\alpha k_x - \frac{\Delta_Z}{2}\right)^2}, \tag{5.29}$$

as $E_F$ departs from $E_F^{(0)}$. Since the states responsible for absorption lie between the two Fermi points, Fig. 5.1, the low-frequency part of the absorption spectrum follows this departure.

### 5.2.3 Optical conductivity at finite temperature

We now turn to the general expression Eq. (5.10) for optical conductivity and perform integration over the directions of momentum, $\mathbf{k}$. This yields the following generalizations of Eqs. (5.15), (5.18) to finite $T$

$$\sigma_\perp(\omega) = \left(\frac{e\,\alpha}{2\sqrt{\pi}\omega\Delta_Z}\right)^2 \sinh\left(\frac{\omega}{2T}\right) \int_0^\infty dk\; k \frac{\sqrt{\left[4\alpha^2k^2 - (\omega + \Delta_Z)^2\right]\left[(\omega - \Delta_Z)^2 - 4\alpha^2k^2\right]}}{\cosh\left(\frac{k^2}{2mT} - \frac{E_F}{T}\right) + \cosh\left(\frac{\omega}{2T}\right)}, \tag{5.30}$$

$$\sigma_{\parallel}(\omega) = \left(\frac{e\,\alpha}{2\sqrt{\pi}\omega\Delta_Z}\right)^2 \sinh\left(\frac{\omega}{2T}\right)\int_0^\infty dk\; k\frac{(4\alpha^2k^2-\Delta_Z^2-\omega^2)^2}{\sqrt{\left[4\alpha^2k^2-(\omega+\Delta_Z)^2\right]\left[(\omega-\Delta_Z)^2-4\alpha^2k^2\right]}}$$
$$\times\frac{1}{\cosh\left(\frac{k^2}{2mT}-\frac{E_F}{T}\right)+\cosh\left(\frac{\omega}{2T}\right)}. \tag{5.31}$$

Expressions Eqs. (5.30) and (5.31), describe the broadening of the optical conductivity peak at finite temperature. We can expect on general grounds that the chiral resonance broadens with $T$ much faster than the EDSR peak. This is because the distance between the two Zeeman-split branches of the spectrum is $\Delta_Z$ at any momentum, while the SO-splitting is proportional to the momentum. In the latter case, the transitions between the states away from the Fermi surface, which become possible with increasing $T$, have different frequencies. For the same reason, the low-frequency absorption that becomes possible near the condition $\Delta_{SO}=\Delta_Z$ is most sensitive to increasing $T$.

#### 5.2.3.1 Temperature smearing of the chiral resonance

In the particular case of the chiral resonance, $\Delta_Z \to 0$, the integration over $k$ can be performed explicitly, since the integrand is non-zero only in the vicinity of $k=\omega/2\alpha$. Then it is sufficient to substitute $k=\omega/2\alpha$ into the denominator. This leads [28] to the following finite-$T$ generalization of Eq. (5.20)

$$\sigma(\delta\omega)=\left(\frac{e^2}{32}\right)\left(\frac{\sinh\left(\frac{\Delta_{SO}+\delta\omega}{2T}\right)}{\cosh\left[\frac{\Delta_{SO}}{4T}\left(1-\frac{\delta\omega}{\omega_1}\right)\right]\cosh\left[\frac{\Delta_{SO}}{4T}\left(1+\frac{\delta\omega}{\omega_1}\right)\right]}\right). \tag{5.32}$$

At low $T \ll \Delta_{SO}$, the hyperbolic sine and cosines can be replaced by the corresponding exponents. Then we find that, outside the plateau, $\sigma(\omega)$ falls off as $\exp(-\frac{\Delta_{SO}}{2T\omega_1}|\delta\omega\pm\omega_1|)$. Thus, the plateau is only slightly rounded near the edges, namely, within the interval $|\delta\omega\pm\omega_1| \sim T\omega_1/\Delta_{SO} \ll \omega_1$. Upon increasing $T$, at $T \gg \Delta_{SO}$, we can neglect 1 in both cosh-terms. Then the denominator will become $\cosh^2(\Delta_{SO}\delta\omega/4T\omega_1)$. We see that characteristic width of the absorption spectrum is $\sim T\omega_1/\Delta_{SO}$, which is much bigger than $\omega_1$. Note however, that, since $\omega_1=\Delta_{SO}^2/4E_F$, this width remains smaller than $\Delta_{SO}$ as long as $T$ remains smaller than $E_F$. Evolution of the shape of the chiral resonance with $T$ is illustrated in Fig. 5.6.

#### 5.2.3.2 Temperature smearing of EDSR

Consider now the opposite limit of EDSR. The prime modification which finite but low temperature imposes on $T=0$ expression Eq. (5.23) is a smearing of the square-root

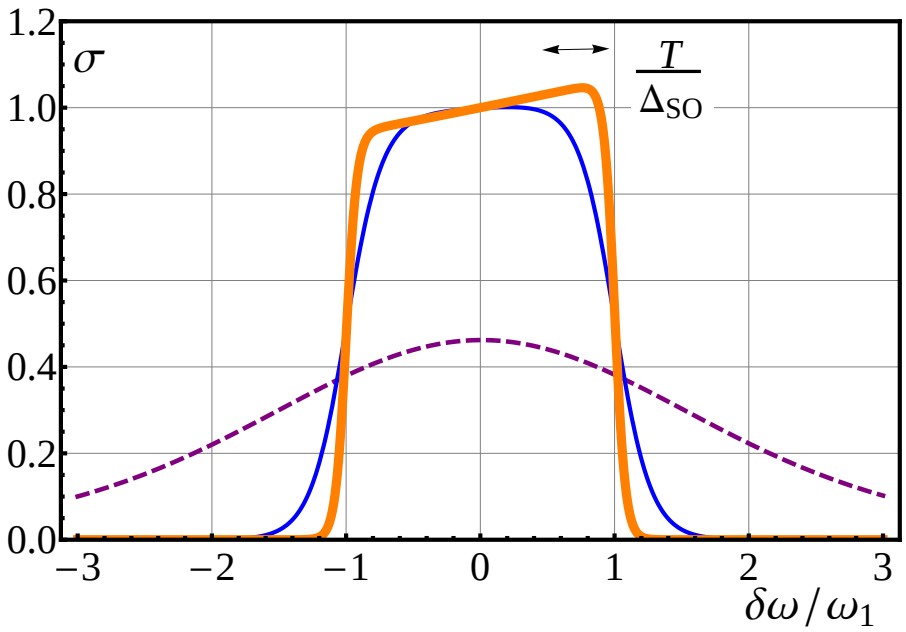


**Figure 5.6**: The optical conductivity, Eq. (5.32), in the case of spin-orbit coupling only, is plotted in the units $e^2/16$ as function of dimensionless deviation $\delta\omega/\omega_1$, for three dimensionless temperatures, $\Delta_{SO}/T$, corresponding to the spin-obit coupling of $\Delta_{SO}/E_F = 0.01$. Thick line: Low temperature limit, $\Delta_{SO}/T = 50$, shows that the optical conductivity approaches a box-like shape. Thin line: As temperature increases, $\Delta_{SO}/T = 15$ , the edges become rounded and the pulse begins to increase. Dashed line: For even higher temperatures, $\Delta_{SO}/T = 2$, the optical conductivity becomes smeared and the width of the pulse becomes comparable to $\omega_1$.

singularities at the edges. Due to temperature smearing, the factor $(|\omega - \Delta_Z| \pm \Delta_{SO})^{1/2}$ gets replaced by $(\omega_1 T/\Delta_{SO})^{1/2}$. To see this, it is convenient to transform from integration over $k$ to integration over $r$, as it was done at $T = 0$. Then from Eq. (5.30), we get

$$\sigma_\perp = \left(\frac{e^2}{8\pi}\right) \int_{-1}^{1} dr \sqrt{1-r^2} \left[ \frac{\sinh(\omega/2T)}{\cosh\left(\frac{2\Delta_Z \omega r + \Delta_Z^2 + \omega^2 - \Delta_{SO}^2}{4\omega_1 T}\right) + \cosh(\omega/2T)} \right]. \tag{5.33}$$

It is seen that for $T \ll \Delta_Z$, we reproduce the zero-temperature result. In the opposite limit, $T \gg \Delta_Z$, the major contribution to the integral still comes from $r$ close to $-1$. In this limit, the hyperbolic sine and cosine can be replaced by the argument and 1, respectively. Introducing the dimensionless variables, $v = (\Delta_Z \omega/2\omega_1 T)(r+1)$ and

$$a(\omega) = \frac{(\Delta_Z - \omega)^2 - \Delta_{SO}^2}{2\Delta_Z \omega}, \tag{5.34}$$

we can rewrite $\sigma_\perp$ as

$$\sigma_\perp(\omega) = \left(\frac{e^2}{4\pi}\right)\left(\frac{\omega_1}{\Delta_Z}\right)^{3/2}\left(\frac{T}{\Delta_Z}\right)^{1/2} g_\perp\left(\frac{|a(\omega)|\Delta_Z\omega}{2\omega_1 T}\right), \tag{5.35}$$

where the dimensionless function $g_\perp(x)$ is defined as

$$g_\perp(x) = \int_0^\infty \frac{dv\sqrt{v}}{\cosh(x \pm v) + 1}. \tag{5.36}$$

In the above definition, the sign is minus for $a(\omega) > 0$ and plus for $a(\omega) < 0$. Consider first positive $a(\omega)$. For $x \gg 1$, the function $g_\perp(x)$ behaves as $2x^{1/2}$, and we reproduce the zero-temperature result. For $x \ll 1$, we can replace $g_\perp(x)$ by $g(0) \approx 1.07$, so that

$$\sigma_\perp = \left(\frac{e^2}{4\pi}\right)\left(\frac{\omega_1}{\Delta_Z}\right)^{3/2}\left(\frac{T}{\Delta_Z}\right)^{1/2}. \tag{5.37}$$

Comparing Eqs. (5.36) and (5.23), we conclude that the smearing of the square-root singularity takes place within the interval, $(\Delta_Z - \omega - \Delta_{SO}) \sim \omega_1 T/\Delta_{SO}$.

The large-$x$ asymptote, for negative $a$, of $g_\perp$ is $g_\perp = \sqrt{\pi}e^{-x}$. The exponential describes the decay of $\sigma_\perp$ in the region of $\omega$ where it was zero at $T = 0$.

In a similar way, the smearing of inverse square-root divergence in Eq. (5.24) is described by the function $g_\parallel(x)$ defined as

$$g_\parallel(x) = \int_0^\infty \frac{dv}{\sqrt{v}\big(\cosh(x \pm v) + 1\big)}. \tag{5.38}$$

Then Eq. (5.31) reads

$$\sigma_\parallel(\omega) = \left(\frac{e^2}{16\pi}\right)\left(\frac{\omega_1}{T}\right)^{1/2} g_\parallel\left(\frac{|a(\omega)|\Delta_Z\omega}{2\omega_1 T}\right). \tag{5.39}$$

For positive $a(\omega)$ in the limit $x \gg 1$, the function $g_\parallel$ tends to $2/\sqrt{x}$ and Eq. (5.39) reduces to Eq. (5.24). The inverse square-root singularity is smeared in the same domain, $(\Delta_Z - \omega - \Delta_{SO}) \sim \omega_1 T/\Delta_{SO}$, as for $\sigma_\perp$, where the argument of $g_\parallel$ is $\sim 1$. In this domain, the ratio $\sigma_\parallel/\sigma_\perp$ remains big but finite, $\sigma_\parallel/\sigma_\perp \sim \frac{\Delta_Z^2}{\omega_1 T}$. For $a(\omega)$ negative, in the large-$x$ limit, we have $g_\parallel = 2\sqrt{\pi}e^{-x}$. Substituting this $g_\parallel$ into Eq. (5.39), we find that to the left of the smeared anomaly $\sigma_\parallel$ decays as

$$\sigma_\parallel = \left(\frac{e^2}{8\sqrt{\pi}}\right)\left(\frac{\omega_1}{T}\right)^{1/2} \exp\left[\frac{-\Delta_{SO}}{2\omega_1 T}\big|\Delta_{SO} - (\omega - \Delta_Z)\big|\right]. \tag{5.40}$$

#### 5.2.3.3 $\Delta_Z = \Delta_{SO}$ at finite $T$

As stated in the Introduction, the most nontrivial situation corresponds to $\Delta_Z = \Delta_{SO}$, where the two Fermi surfaces undergo restructuring. The expressions for $T = 0$ optical conductivity under this condition read

$$\sigma_\perp(\omega) = \left(\frac{e^2}{8\pi}\right)\frac{\omega_1}{\Delta_Z^2}\sqrt{4\Delta_Z^2 - \omega^2}, \tag{5.41}$$

$$\sigma_\parallel(\omega) = \left(\frac{e^2}{8\pi}\right)\frac{\omega_1}{\Delta_Z^2}\frac{\omega^2}{\sqrt{4\Delta_Z^2 - \omega^2}}, \tag{5.42}$$

We will now analyze how temperature affects the low-$\omega$ part of absorption and the sharp edge at $\omega = 2\Delta_Z$.

It is convenient to make the change of variable $k^2 = 2m(E_F + QT)$ in Eq. (5.30), after which it takes the form

$$\begin{aligned}\sigma_\perp(\omega) \;=\; &\left(\frac{e^2}{32\pi\omega^2}\right)\left(\frac{\Delta_{SO}}{\Delta_Z}\right)^2\left(\frac{T}{E_F}\right)\sinh\left(\frac{\omega}{2T}\right)\int dQ \\ &\times\frac{\sqrt{4\Delta_{SO}^2\Delta_Z^2\left(1+\frac{QT}{E_F}\right) - \left(\Delta_{SO}^2\left(1+\frac{QT}{E_F}\right) + \Delta_Z^2 - \omega^2\right)^2}}{\cosh Q + \cosh\left(\frac{\omega}{2T}\right)}.\end{aligned} \tag{5.43}$$

Now look at the point where $\Delta_{SO} = \Delta_Z$, in the limit $T \gg \omega$. Then Eq. (5.43) reduces to

$$\sigma_\perp(\omega) = \left(\frac{e^2}{64\pi}\right)\left(\frac{\Delta_Z^2}{\omega E_F}\right)\int dQ\frac{\sqrt{\frac{4\omega^2}{\Delta_Z^2} - \left(\frac{QT}{E_F} - \frac{\omega^2}{\Delta_Z^2}\right)^2}}{\cosh Q + 1}. \tag{5.44}$$

Similarly, the $T \gg \omega$ limit of Eq. (5.31) assumes the form

$$\sigma_\parallel(\omega) = \left(\frac{e^2}{64\pi}\right)\left(\frac{\Delta_Z^2}{\omega E_F}\right)\int dQ\frac{\left(\frac{QT}{E_F} - \frac{\omega^2}{\Delta_Z^2}\right)^2}{(\cosh Q + 1)\sqrt{\frac{4\omega^2}{\Delta_Z^2} - \left(\frac{QT}{E_F} - \frac{\omega^2}{\Delta_Z^2}\right)^2}}. \tag{5.45}$$

Consider first the domain $\omega \ll \Delta_Z$. Then in the combination $(\frac{QT}{E_F} - \frac{\omega^2}{\Delta_Z^2})$ in the integrands of Eqs. (5.44) and (5.45), the term $(\omega/\Delta_Z)^2$ can be dropped. This allows us to simplify Eqs. (5.44) and (5.45) to

$$\sigma_\perp(\omega) = \left(\frac{e^2}{32\pi}\right)\left(\frac{\Delta_Z}{E_F}\right)G_\perp\left(\frac{2\omega E_F}{\Delta_Z T}\right), \tag{5.46}$$

$$\sigma_\parallel(\omega) = \left(\frac{e^2}{32\pi}\right)\left(\frac{\Delta_Z}{E_F}\right)G_\parallel\left(\frac{2\omega E_F}{\Delta_Z T}\right), \tag{5.47}$$

where the functions $G_\perp$ and $G_\parallel$ are defined as

$$G_\perp(s) = \frac{1}{s}\int_{-s}^{s} \frac{dQ}{\cosh Q + 1}\sqrt{s^2 - Q^2}, \tag{5.48}$$

$$G_\parallel(s) = \frac{1}{s}\int_{-s}^{s} \frac{dQ}{\cosh Q + 1}\frac{Q^2}{\sqrt{s^2 - Q^2}}. \tag{5.49}$$

These functions are plotted in Fig. 5.7a inset. At $s \ll 1$, they both behave as $\pi s/4$. For $s \gg 1$, the function $G_\perp$ saturates at $G_\perp(\infty) = 2$, while the function $G_\parallel$ falls off as $G_\parallel(s) \approx 2\pi^2/3s^2$.

It can be seen from Fig. 5.7a inset that $G_\parallel(s)$ has a maximum at $s = \tilde{s} = 1.83$. This translates into the maximum in absorption at frequency

$$\tilde{\omega} = \frac{0.91\Delta_Z T}{E_F}. \tag{5.50}$$

This sharp maximum clearly shows in the absorption lines plotted in Fig. 5.7a,b which were calculated numerically from the full expression Eq. (5.45) for particular temperatures, $T/E_F = 0.05$ and $T/E_F = 0.2$. Remarkably, the position of maximum moves linearly with temperature for low temperatures. The maximum starts to disappear when temperature becomes high enough, $T/E_F = 0.5$. It is also seen from Figs. 5.7b,c that the right boundary $\omega \approx 2\Delta_Z$ of the absorption spectrum is smeared with temperature. This smearing can be described analytically in terms of the functions $g_\perp$ and $g_\parallel$ defined by Eqs. (5.36) and (5.38). Indeed, for $\omega$ close to $2\Delta_Z$, the square root in the numerator of Eq. (5.44) can be simplified to $\sqrt{2}(\omega/\Delta_Z)\left[\frac{QT}{E_F} - \frac{2}{\Delta_Z}(\omega - 2\Delta_Z)\right]^{1/2}$. Then $\sigma_\parallel(\omega)$ and $\sigma_\perp(\omega)$ acquire the form

$$\sigma_\perp(\omega) = \left(\frac{\sqrt{2}e^2}{64\pi}\right)\left(\frac{\Delta_Z}{E_F}\right)\left(\frac{T}{E_F}\right)^{1/2} g_\perp\left(\frac{2E_F}{T}\frac{(\omega - 2\Delta_Z)}{\Delta_Z}\right), \tag{5.51}$$

$$\sigma_\parallel(\omega) = \left(\frac{e^2}{64\sqrt{2}\pi}\right)\left(\frac{\Delta_Z}{E_F}\right)\left(\frac{E_F}{T}\right)^{1/2} g_\parallel\left(\frac{2E_F}{T}\frac{(\omega - 2\Delta_Z)}{\Delta_Z}\right). \tag{5.52}$$

It is worth noting that even at high temperature $T = 0.5E_F$ the right boundary $\omega = 2\Delta_Z$ is very well pronounced.

## 5.3 ESR lineshape

In this section, we use the above results for the absorption of the electric field to calculate the ESR lineshape.

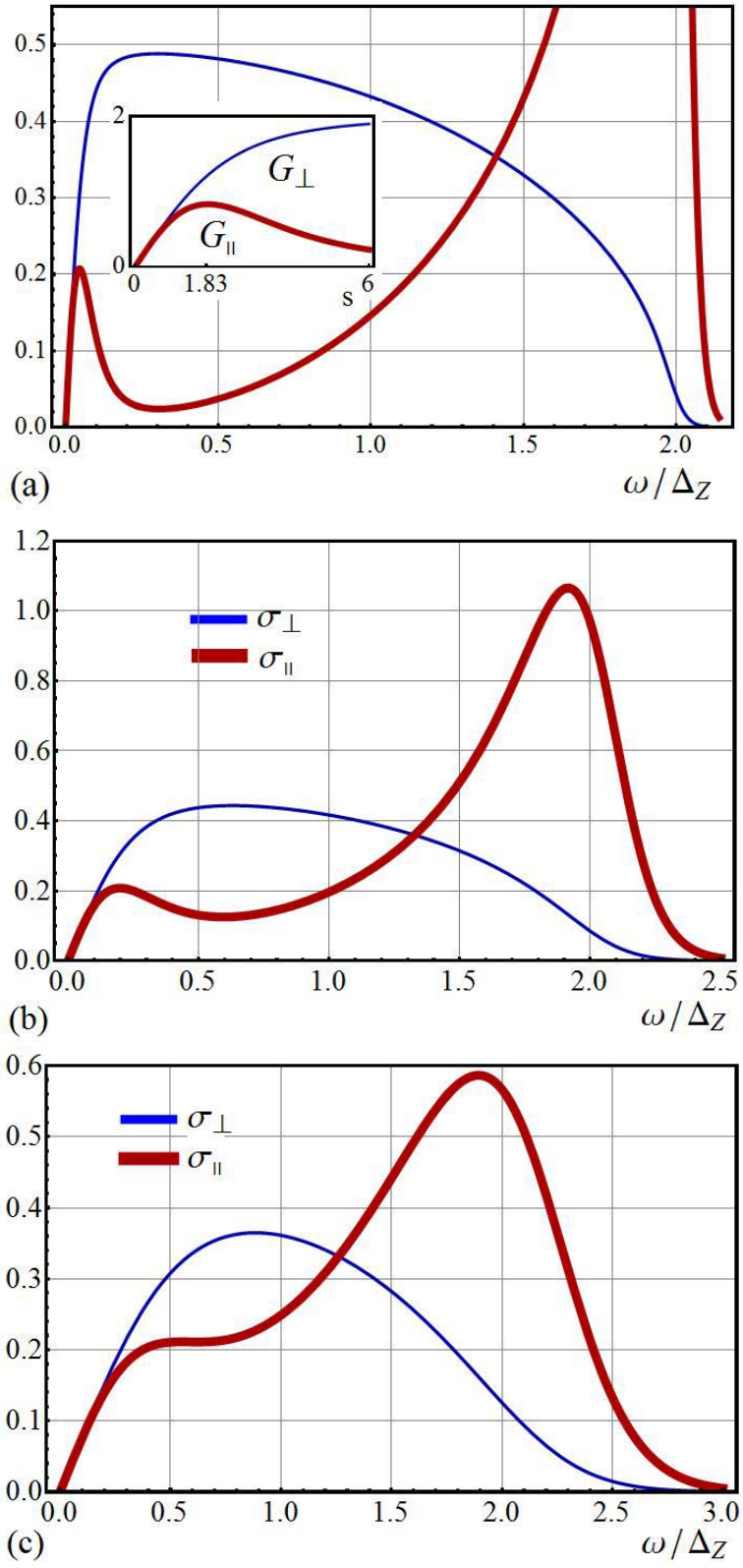


**Figure 5.7**: Evolution of optical conductivity with $T$ in the regime $\Delta_Z = \Delta_{SO}$. Eqs. (5.44) and (5.45) are plotted in the units $(e^2/16\pi)(\Delta_Z/E_F)$ for three values of $T/E_F$; (a) low temperature limit $T/E_F = 0.05$. (b) intermediate temperature $T/E_F = 0.2$. (c) "high" temperature $T/E_F = 0.5$. Inset in (a) shows the dimensionless functions $G_\perp(s)$ and $G_\parallel(s)$ calculated from Eqs. (5.48) and (5.49), respectively.

For ESR, the corresponding interaction Hamiltonian of spins with the ac magnetic field reads

$$\hat{H}^m_{int} = \gamma\big(2\hat{\mathbf{s}}\cdot\mathbf{B}\big)\cos\omega t, \tag{5.53}$$

where $\gamma$ is the gyromagnetic ratio. The quantity describing the ESR strength, the imaginary part of susceptibility, can be expressed via the eigenfunctions of the free Hamiltonian Eq. (5.4) as follows

$$\chi_i(\omega) = 8\pi\gamma^2\big(1-e^{-\omega/T}\big)\sum_{\mathbf{k}}\big|\langle u^{(1)}_{\mathbf{k}}\big|\hat{s}_i\big|u^{(2)}_{\mathbf{k}}\rangle\big|^2\delta\big(\mathcal{E}^{(2)}_{\mathbf{k}}-\mathcal{E}^{(1)}_{\mathbf{k}}-\omega\big)\Big[1-f\big(\mathcal{E}^{(2)}_{\mathbf{k}}\big)\Big]f\big(\mathcal{E}^{(1)}_{\mathbf{k}}\big), \tag{5.54}$$

where $i$ is the polarization axis of the ac magnetic field.

Our prime observation is that the values $\chi_i$ can be expressed in a simple way though the components of optical conductivity, $\sigma_\perp(\omega)$ and $\sigma_\parallel(\omega)$, calculated above. Consider, for example, the ac magnetic field polarized along $x$. Then, using Eqs. (5.5), (5.6), the matrix element $\langle u^{(2)}_{\mathbf{k}}\big|\hat{s}_x\big|u^{(1)}_{\mathbf{k}}\rangle$ can be expressed as

$$\langle u^{(1)}_{\mathbf{k}}\big|\hat{s}_x\big|u^{(2)}_{\mathbf{k}}\rangle = i\frac{\alpha k_x-\Delta_Z/2}{\mathcal{E}^{(2)}_{\mathbf{k}}-\mathcal{E}^{(1)}_{\mathbf{k}}}. \tag{5.55}$$

Upon transformation to polar coordinates, the numerator of Eq. (5.55) turns into $k\cos\phi-\Delta_Z/2$, while the $\delta$-function in Eq. (5.54) insures that the denominator is equal to $\omega$. In this way, the summation over momenta in Eq. (5.54) reduces to the same integration as in Eq. (5.18) and we arrive at the relation

$$\chi_x(\omega) = \frac{2\gamma^2}{e^2\alpha^2}\omega\sigma_\parallel(\omega). \tag{5.56}$$

From comparing Eq. (5.54) to Eq. (5.10), it is obvious that this relation applies at all temperatures.

Similarly, the matrix element $\langle u^{(1)}_{\mathbf{k}}\big|\hat{s}_y\big|u^{(2)}_{\mathbf{k}}\rangle$ in polar coordinates assumes the form $i\alpha k\sin\phi/(\mathcal{E}^{(2)}_{\mathbf{k}}-\mathcal{E}^{(1)}_{\mathbf{k}})$. This makes Eq. (5.54) for $i=y$ proportional to $\sigma_\perp$ in Eq. (5.12), and leads to

$$\chi_y(\omega) = \frac{2\gamma^2}{e^2\alpha^2}\omega\sigma_\perp(\omega). \tag{5.57}$$

Concerning polarization of the magnetic field along $z$, we have

$$\langle u^{(1)}_{\mathbf{k}}\big|\hat{s}_z\big|u^{(2)}_{\mathbf{k}}\rangle = -1, \tag{5.58}$$

so that summation over momenta does not contain angular dependence at all. This allows to relate $\chi_z(\omega)$ to the sum of $\sigma_\perp(\omega)$ and $\sigma_\parallel(\omega)$ as follows

$$\chi_z = \frac{2\gamma^2}{e^2\alpha^2}\omega\big[\sigma_\perp(\omega)+\sigma_\parallel(\omega)\big]. \tag{5.59}$$

We see that ESR line shape for different polarizations of the ac magnetic field can be written in terms of optical conductivity $\sigma_\perp$ and $\sigma_\parallel$. Response to the ac field polarized perpendicular to the static field, namely, $\chi_x$ and $\chi_z$, is determined mostly by $\sigma_\parallel(\omega)$, which diverges in an inverse square-root fashion at the boundaries of the absorption interval. In a weak static field, the lineshape is a $\delta$-peak at $\omega = \Delta_{SO}$ [29].

It is natural that the ac field parallel to the static field causes less singular response, than the ac field normal to the static field. Indeed, $\chi_y$ is proportional to $\sigma_\perp(\omega)$, which exhibits square-root suppression at the boundaries of the absorption interval.

## 5.4 Discussion

Interplay of spin-orbit interaction and in-plane magnetic field results in a strongly anisotropic line shape of the ESR response of the two-dimensional fermion gas. The response is most singular at the upper and lower boundaries of the fermion continuum when the ac magnetic field is perpendicular to the static magnetic field. See Fig. 5.5 and Section 5.3. The behavior of the ESR lineshape is most "lively" near the "compensation" point $\Delta_Z = \Delta_{SO}$, where it exhibits a nontrivial temperature dependence up to high temperature $T \sim E_F$.

A possible way to reveal these features experimentally is to fix the polarization of microwave radiation and to rotate the sample with respect to the external static magnetic field.

Restricting two-dimensional gas to a quantum wire geometry when the motion along, say, $y$-axis is quantized, will result in "slicing" the Fermi-surface along several allowed $k_y$ momenta. The wire geometry is analyzed in Part II Chapter 2. In the extreme case of the single channel quantum wire, when only the lowest transverse subband is populated, the ESR lineshape will be reduced to two delta-function-like features at the lower and upper boundaries of the ESR continuum. This is exactly the response found previously [30] within a different, purely one-dimensional treatment of an insulating Heisenberg spin chain with uniform DM interaction. Ref. [31] finds a very similar response of a conducting quantum wire with spin-orbit interaction to an ac electric field. The correspondence between the two above mentioned one-dimensional studies illustrates nicely the central point of our work that ESR is an effective probe of the Fermi surfaces irrespective of their origin. Both conventional Fermi surface [31] and spinon Fermi surface [30] give rise to the same ESR response.

One-dimensional geometry also allows one to address effects of electron-electron inter-

actions omitted in the present work. Although relatively marginal even in one-dimensional geometry [30], these are difficult to account for at finite frequencies as recent detailed investigation shows [32]. Extending this approach to two-dimensional systems, along the lines of renormalization group calculations in [33], represents an interesting outstanding problem.

It is worth noting that ideas outlined here have been recently successfully tested experimentally [34] in quasi-one-dimensional spin-1/2 antiferromagnet $Cs_2CuCl_4$ where uniform DM interaction on chain bonds was found to split the an ESR signal into two peaks already in the finite-temperature spin-liquid phase, just as we describe above. Many higher-dimensional candidate spin-liquid materials, such as two-dimensional $\kappa$-(BEDT-TTF)$_2$Cu$_2$(CN)$_3$ [35] and three-dimensional $Na_4Ir_3O_8$ [36], have been argued to possess spin-liquid ground states with spinon Fermi surfaces [8, 9, 37, 13, 38]. DM and other kinds of spin-orbit interactions are most certain to be present in these materials – this is certainly the case for $Na_4Ir_3O_8$ and highly likely for the organic material as well (its close relative, $\kappa$-(BEDT-TTF)$_2$Cu[N(CN)$_2$]Cl, does have substantial DM interaction [39]). Our work shows that spin-orbit interaction can turn ESR absorption experiment into an insightful probe of the unusual spinon Fermi surfaces in these and related materials.

## 5.5 References


[1] M. Oshikawa and I. Affleck, Phys. Rev. B **65**, 134410 (2002).

[2] W. Kohn, Phys. Rev. **123**, 1242 (1961).

[3] L. Balents, Nature **464**, 199 (2010).

[4] I. E. Dzyaloshinskii, Journal of Physics and Chemistry of Solids **4**, 241 (1958).

[5] T. Moriya, Phys. Rev. **120**, 91 (1960).

[6] P. W. Anderson, Science **235**, 1196 (1987).

[7] Interestingly, the proposal has even a more peculiar history – the first mentioning of neural fermions in connection with antiferromagnets goes back to the paper by I. Pomeranchuk, Journal of Physics USSR **4**, 357 (1941).

[8] S.-S. Lee and P. A. Lee, Phys. Rev. Lett. **95**, 036403 (2005).

[9] O. I. Motrunich, Phys. Rev. B **72**, 045105 (2005).

[10] Yu. A. Bychkov and E. I. Rashba, Pis'ma Zh. Eksp. Teor. Fiz. **39**, 66 (1984) [JETP Lett. **39**, 78 (1984)].

[11] S. Florens and A. Georges, Phys. Rev. B **70**, 035114 (2004).

[12] E. Zhao and A. Paramekanti, Phys. Rev. B **76**, 195101 (2007).

[13] D. Podolsky, A. Paramekanti, Y. B. Kim, and T. Senthil, Phys. Rev. Lett. **102** 186401 (2009).

[14] D. F. Mross and T. Senthil, Phys. Rev. B **84**, 041102 (2011).

[15] Y. Zhou and P. A. Lee, Phys. Rev. Lett. **106**, 056402 (2011).

[16] P. A. Lee, N. Nagaosa, and X.-G. Wen, Rev. Mod. Phys. **78**, 17 (2006).

[17] D. Coffey, T. M. Rice, and F. C. Zhang, Phys. Rev. B **44**, 10112 (1991).

[18] L. Shekhtman, O. Entin-Wohlman, and A. Aharony, Phys. Rev. Lett. **69**, 836 (1992).

[19] N. E. Bonesteel, Phys. Rev. B **47**, 11302 (1993).

[20] E. I. Rashba, Fiz. Tverd. Tela (Leningrad) **2**, 1224 (1960) [Sov. Phys. Solid State **2**, 1109 (1960)].

[21] O. I. Motrunich, Phys. Rev. B **73**, 155115 (2006).

[22] E. I. Rashba and V. I. Sheka, Fiz. Tverd. Tela **3**, 1735 (1961) [Sov. Phys. Solid State **3**, 1257 (1961)].

[23] E. I. Rashba and Al. L. Efros, Phys. Rev. Lett. **91**, 126405 (2003).

[24] E. I. Rashba and Al. L. Efros, Phys. Rev. B **73**, 165325 (2006).

[25] A. Shekhter, M. Khodas, and A. M. Finkelstein, Phys. Rev. B **71**, 165329 (2005).

[26] A.-K. Farid and E. G. Mishchenko, Phys. Rev. Lett. **97**, 096604 (2006).

[27] E. G. Mishchenko, M. Yu. Reizer, and L. I. Glazman, Phys. Rev. B **69**, 195302 (2004).

[28] L. I. Magarill, A. V. Chaplik, and M. V. Entin, Zh. Eksp. Teor. Fiz. **92**, 153, (2001).

[29] S. I. Erlingsson, J. Schliemann, and D. Loss, Phys. Rev. B **71**, 035319 (2005).

[30] S. Gangadharaiah, J. Sun, and O. A. Starykh, Phys. Rev. B **78**, 054436 (2008).

[31] Ar. Abanov, V. L. Pokrovsky, W. M. Saslow, P. Zhou, Phys. Rev. B **85**, 085311 (2012).

[32] H. Karimi and I. Affleck, Phys. Rev. B **84**, 174420 (2011).

[33] R. A. Zak, D. L. Maslov, and D. Loss, Phys. Rev. B **82**, 115415 (2010).

[34] K. Yu. Povarov, A. I. Smirnov, O. A. Starykh, S. V. Petrov, and A. Ya. Shapiro, Phys. Rev. Lett. **107**, 037204 (2011).

[35] Y. Shimizu, K. Miyagawa, K. Kanoda, M. Maesato, and G. Saito, Phys. Rev. Lett. **91**, 107001 (2003).

[36] Y. Okamoto, M. Nohara, H. Aruga-Katori, and H. Takagi, Phys. Rev. Lett. **99**, 137207 (2007).

[37] M. J. Lawler, A. Paramekanti, Y. B. Kim, and L. Balents, Phys. Rev. Lett. **101**, 197202 (2008).

[38] D. Pesin and L. Balents, Nature Phys. **6**, 376 (2010).

[39] D. Smith, C. P. Slichter, J. A. Schlueter, A. M. Kini, and R. G. Daugherty, Phys. Rev. Lett. **93**, 167002 (2004).

# CHAPTER 6

# INTERPLAY OF SPIN-ORBIT COUPLING AND ZEEMAN SPLITTING IN THE ABSORPTION LINESHAPE OF 1D QUANTUM WIRE

## 6.1 Introduction

In the previous chapter, we established that the absorption spectrum of 2D electron gas has a peculiar shape near the "compensation" condition when the Zeeman energy, $\Delta_Z$, is equal to the spin-orbit splitting, $\Delta_{SO}$. This origin of this peculiar shape is explained qualitatively in Fig. 6.1. At zero $\Delta_Z$, the absorption is due to the chiral resonance (CR), and the line is a narrow peak. At very small $\Delta_{SO}$, the absorption is due to the EDSR mechanism, and the line is again a narrow peak. At $\Delta_Z \approx \Delta_{SO}$, the spectrum of 2D electrons becomes anisotropic. As a result, the absorption peak transforms into a band which ranges between $|\Delta_Z - \Delta_{SO}|$ and $|\Delta_Z + \Delta_{SO}|$. The objective of the present chapter is to study how this peculiar absorption lineshape is modified in the quantum-wire geometry when electron motion is restricted along one axis, say along $y$.

General interest in quantum wires with spin-orbit coupling was initiated in 1999 after the publication of paper [1]. The main finding of this paper is illustrated in Fig. 6.2. Normally, the evolution of the conductance, $G$, with density (or the Fermi level, $E_F$) is monotonic. It represents a sequence of steps of height $2e^2/h$. Every next step occurs when $E_F$ crosses the bottom of the next size-quantization subband. As was first noted in Ref. [1], in the presence of SO coupling, the dispersion law, $E_n^{\pm}(k)$, of some subbands becomes nonmonotonic with local minima at finite values of momenta. This results in negative slopes in subband dispersion curves, $E_n^{\pm}(k)$ (+ and − correspond to different directions of propagation), at zero longitudinal momentum, $k = 0$. Negative slope is a direct consequence of the fact that $\hat{H}_{SO}$ is an odd function of $\mathbf{k}$. Presence of the regions with negative slopes gives rise to narrow peaks [1] in the dependence, $G(E_F)$.

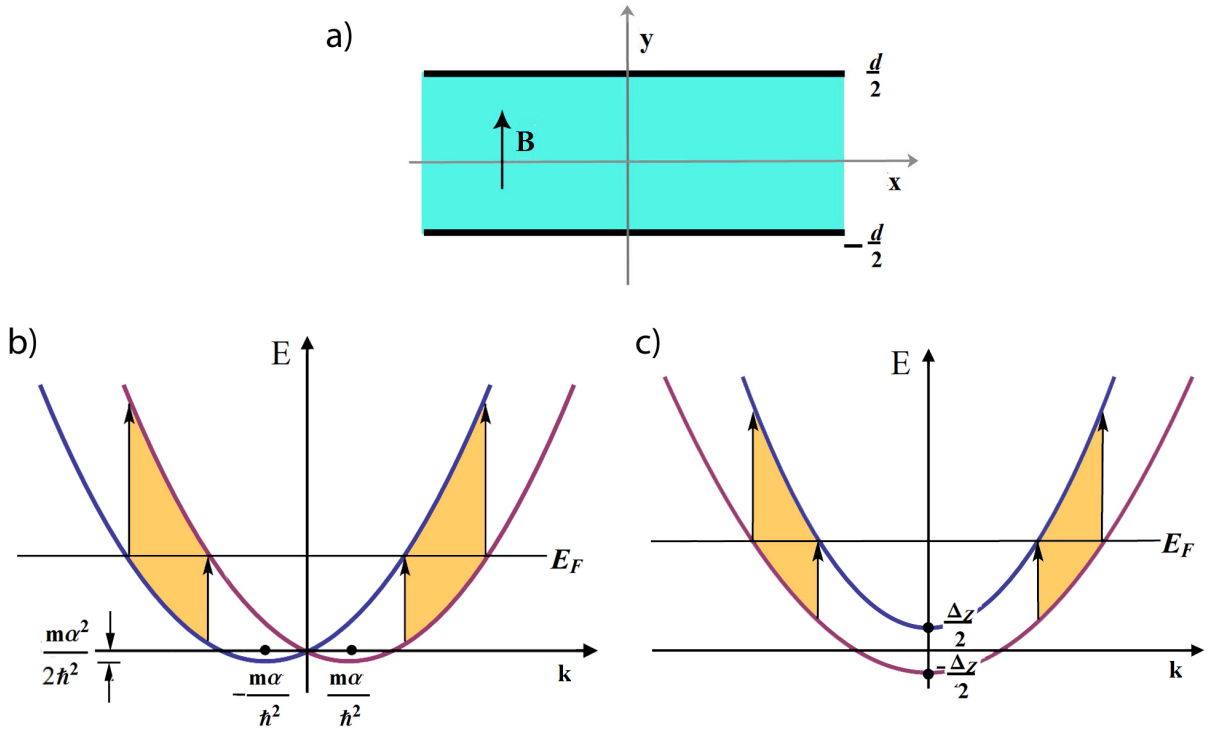


**Figure 6.1**: The three effects that we consider are illustrated separately. (a) Geometry considered in the present chapter: quantum wire with magnetic field perpendicular to the axis, (b) Schematic illustration of absorption in the regime of chiral resonance (CR), (c) Schematic illustration of absorption in the regime of EDSR. The domain of momenta participating in absorption is shown in yellow, with initial states below the Fermi-level, and final states above the Fermi-level.

Different aspects of this effect were addressed in subsequent theoretical papers [2, 3, 4, 5, 6, 7, 8, 9, 10] in connection to the spin transport. Presence of a local maximum is appealing for potential applications since its position depends on the SO coupling strength, and can be thus tuned by applying the gate voltage.

Degeneracy of $E_n^{\pm}(k)$ at $k = 0$ is lifted by the in-plane magnetic field. Nontrivial interplay [11, 12, 13, 14, 15] of Zeeman splitting in energy, $\Delta_Z$, and SO splitting of subbands in the momentum space affects the subband dispersions when $\Delta_Z$ is comparable to the depth of the minima in $E_n^{\pm}(k)$. This interplay manifests itself in "spin-orbit gaps" in $G(E_F)$ curves [11]. These gaps are illustrated in Fig. 6.3, 6.4. Experimental observation of these gaps has been recently reported in Ref. [16] and the corresponding $G(E_F)$ curves are shown in Fig. 6.5.

In Ref. [17], the sensitivity of $G(E_F)$ to the orientation of the Zeeman field, which is

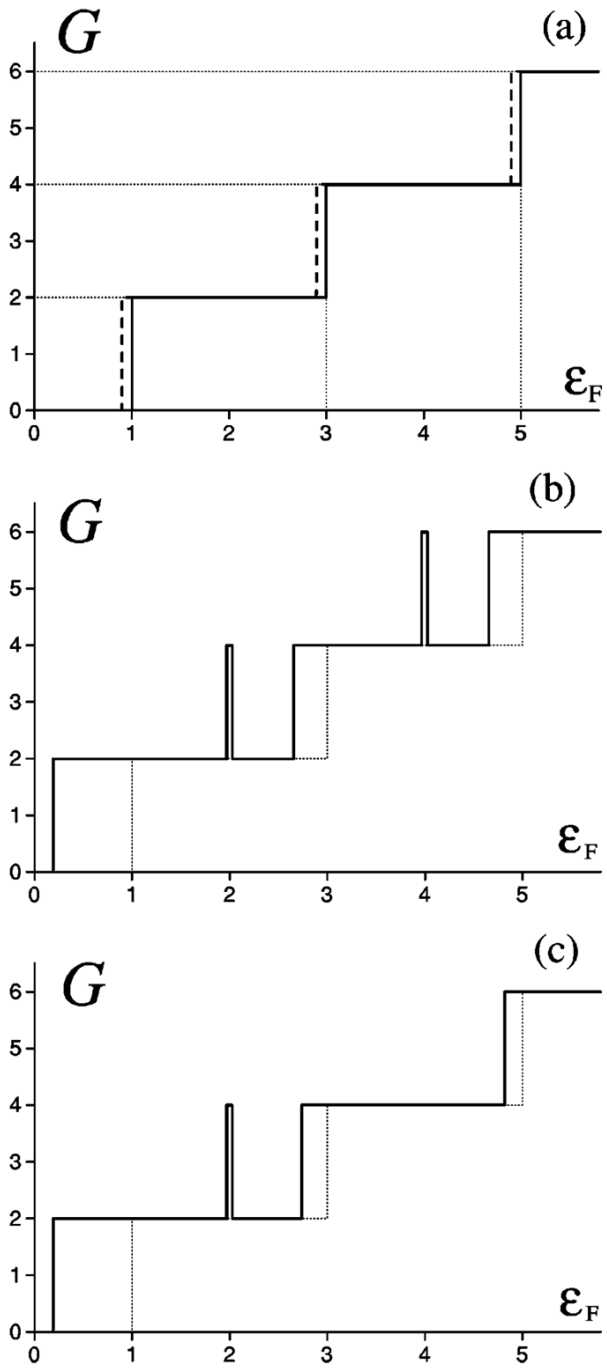


**Figure 6.2**: From Ref. [1] The conductance, $G$, of a quantum wire with parabolic confinement in units of $e^2/h$ vs the Fermi energy, $E_F$: (a) zero SO coupling; (b) and (c) finite SO coupling with different relative strengths of the Rashba and Dresselhaus terms.

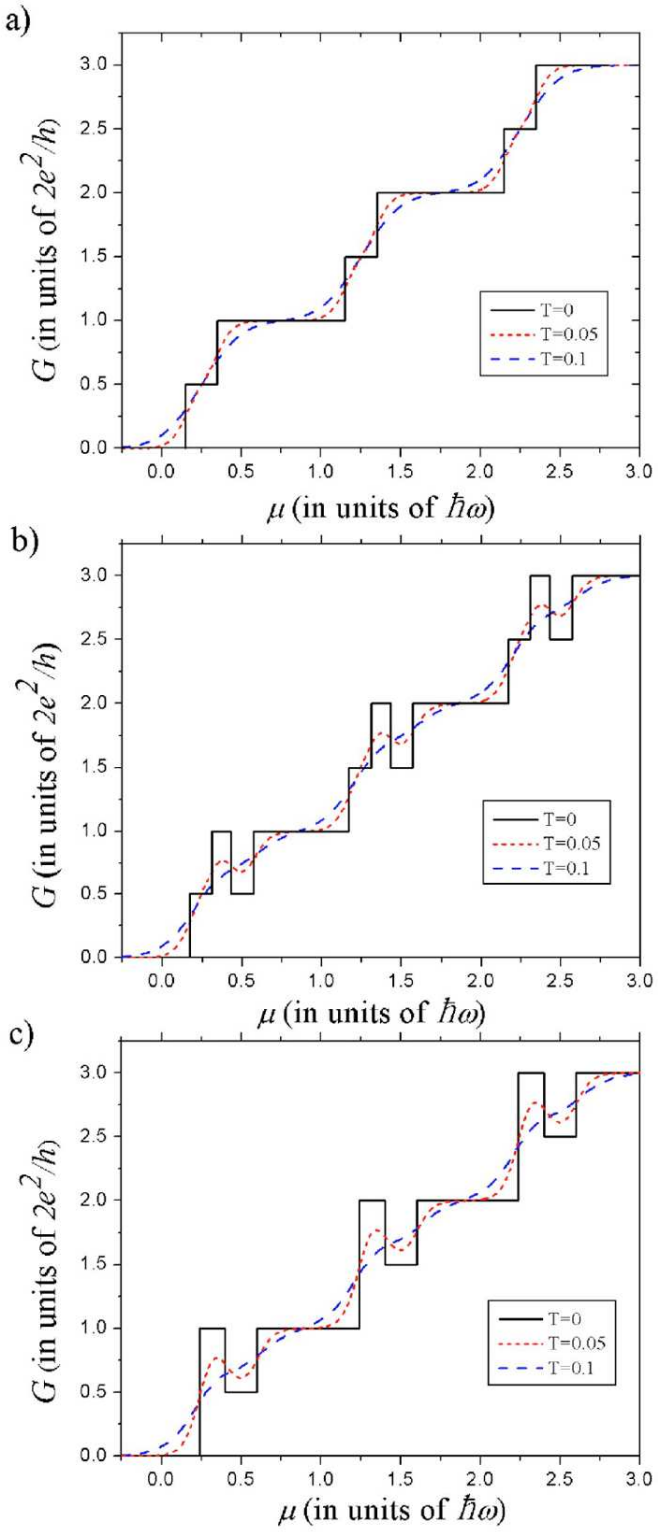


**Figure 6.3**: Conductance of a quantum wire with SO coupling as a function of the Fermi level, $\mu$, calculated in Ref. [11] for different directions of the Zeeman field and different temperatures. Compared to Fig. 6.2 in zero magnetic field, the dependence $G(\mu)$ contains dips, or "spin gaps".

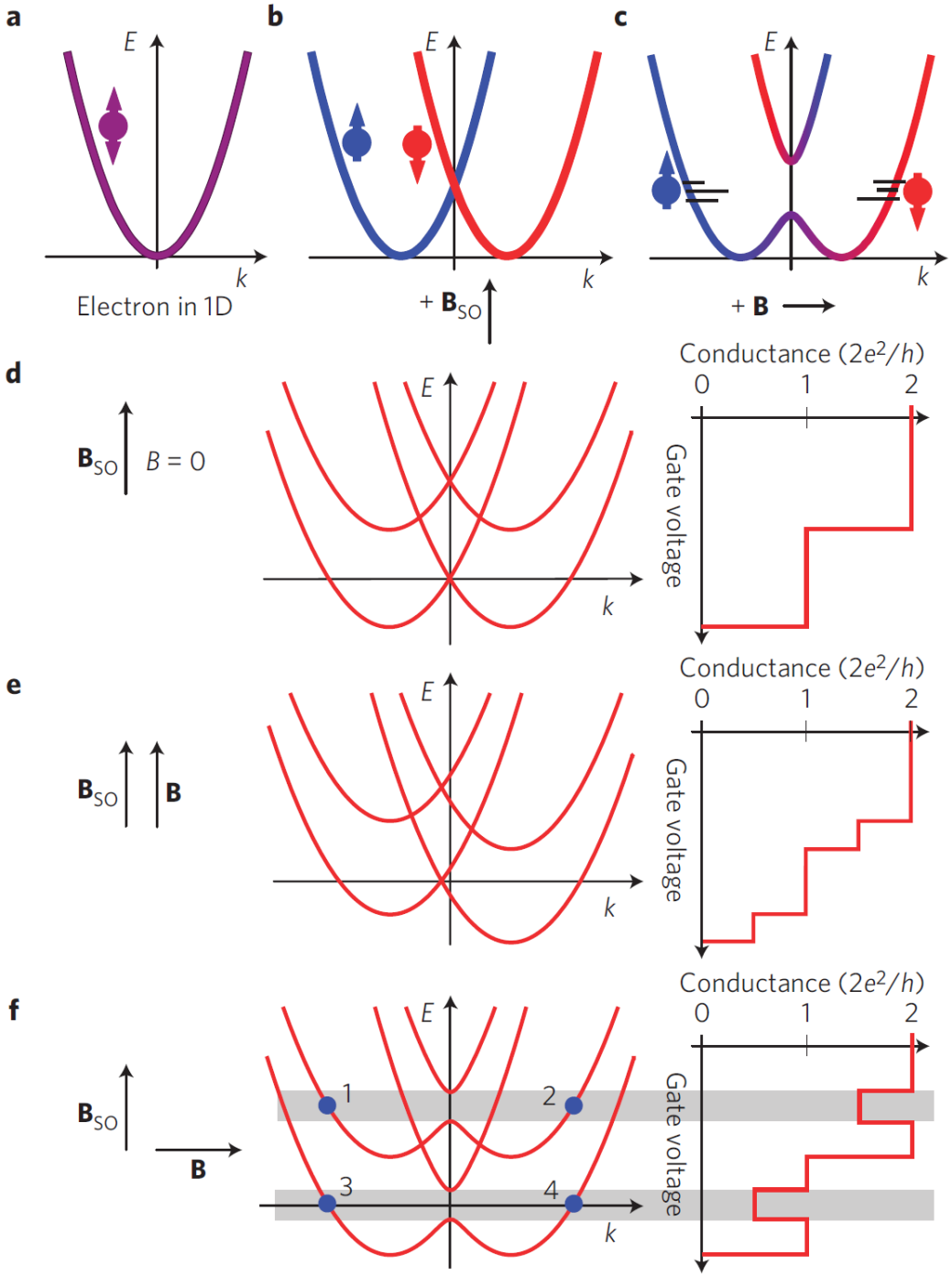


**Figure 6.4**: Dispersion laws of different subbands of a quantum wire in the presence of SO coupling corresponding to different orientations of the Zeeman field (from Ref. [16]). The corresponding $G(\mu)$ curves exhibit "spin gaps" only for one orientation of **B**.

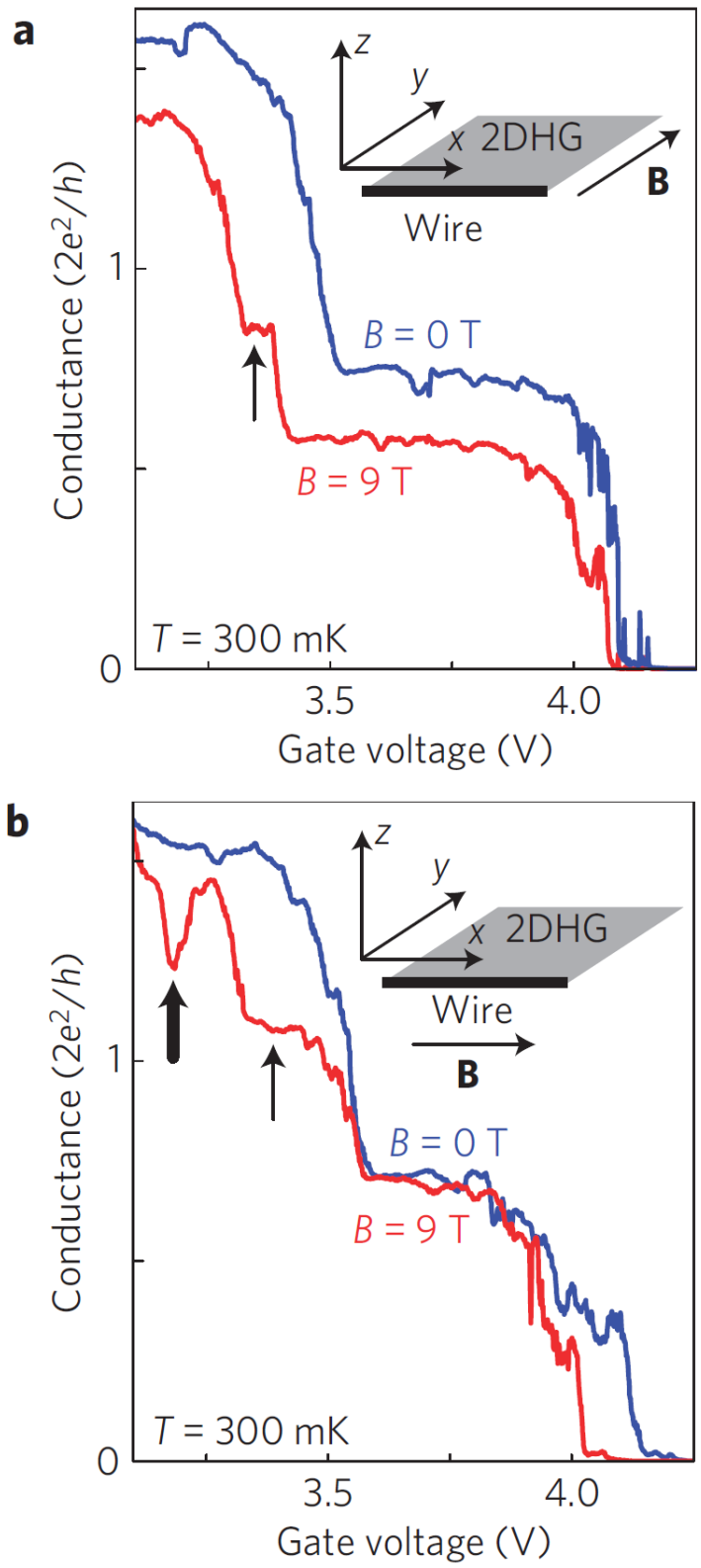


**Figure 6.5**: Experimental dependencies, $G(\mu)$ in a quantum wire reported in Ref. [16]. It is seen that "spin gaps" emerge upon applying a strong in-plane magnetic field.

also a result of interplay of the Zeeman and SO couplings, has been observed. Experiments [16, 17] were carried out on the hole gases in wires and point contacts. Since SO coupling is inherently strong for holes, the corresponding magnetic fields were high, on the order of several Tesla. The most exciting physical effect which takes place in quantum wire with spin-orbit coupling is the so-called Spin Hall effect predicted in Ref. [18] more than 40 years ago. The essence of this effect is that passage of current through a wire results in accumulation of one spin projection, say "up", on the left edge of the wire, while the "down" projection is accumulated on the right edge of the wire. Similarly to a magnetic field, deflecting charges of opposite signs in opposite directions, causing the conventional Hall effect, the SO-field causes the deflection of electrons with different spin orientations to the opposite sides of the wire. First reports of experimental observation of the Spin Hall effect appeared only recently [19, 20]. In Ref. [20], the edge accumulation of spin was registered using the optical technique called the Kerr effect. The observed profile of spin at the edge visualized in Ref. [20] is shown in Fig. 6.6.

Lately, the interest to combined action of Zeeman and SO couplings in quantum wires was fueled by the prediction [21, 22] of quantum phase transitions in this system when it is placed in the proximity to a superconductor.

The only paper on optical absorption in quantum wire with SO coupling, Ref. [23], was published only recently. It is focused on a particular arrangement when $\Delta_{SO}$ is much bigger than $\Delta_Z$.

## 6.2 Hamiltonian and energy spectrum in dimensionless units

To generalize the theory of absorption, discussed in Part II, Chapter 1, to a quantum wire, it is convenient to introduce dimensionless projections of momentum

$$P = \frac{2\alpha k_x}{\Delta_Z}, \qquad Q = \frac{2\alpha k_y}{\Delta_Z}. \tag{6.1}$$

Then the Hamiltonian, Eq. (5.4), takes the form

$$\hat{H}(P,Q) = E_0 \begin{pmatrix} P^2+Q^2 & 2i\nu\big(1-P+iQ\big) \\ -2i\nu\big(1-P-iQ\big) & P^2+Q^2 \end{pmatrix}, \tag{6.2}$$

where $E_0$ is a characteristic energy of the problem

$$E_0 = \frac{\hbar^2\Delta_Z^2}{8m\alpha^2}, \tag{6.3}$$

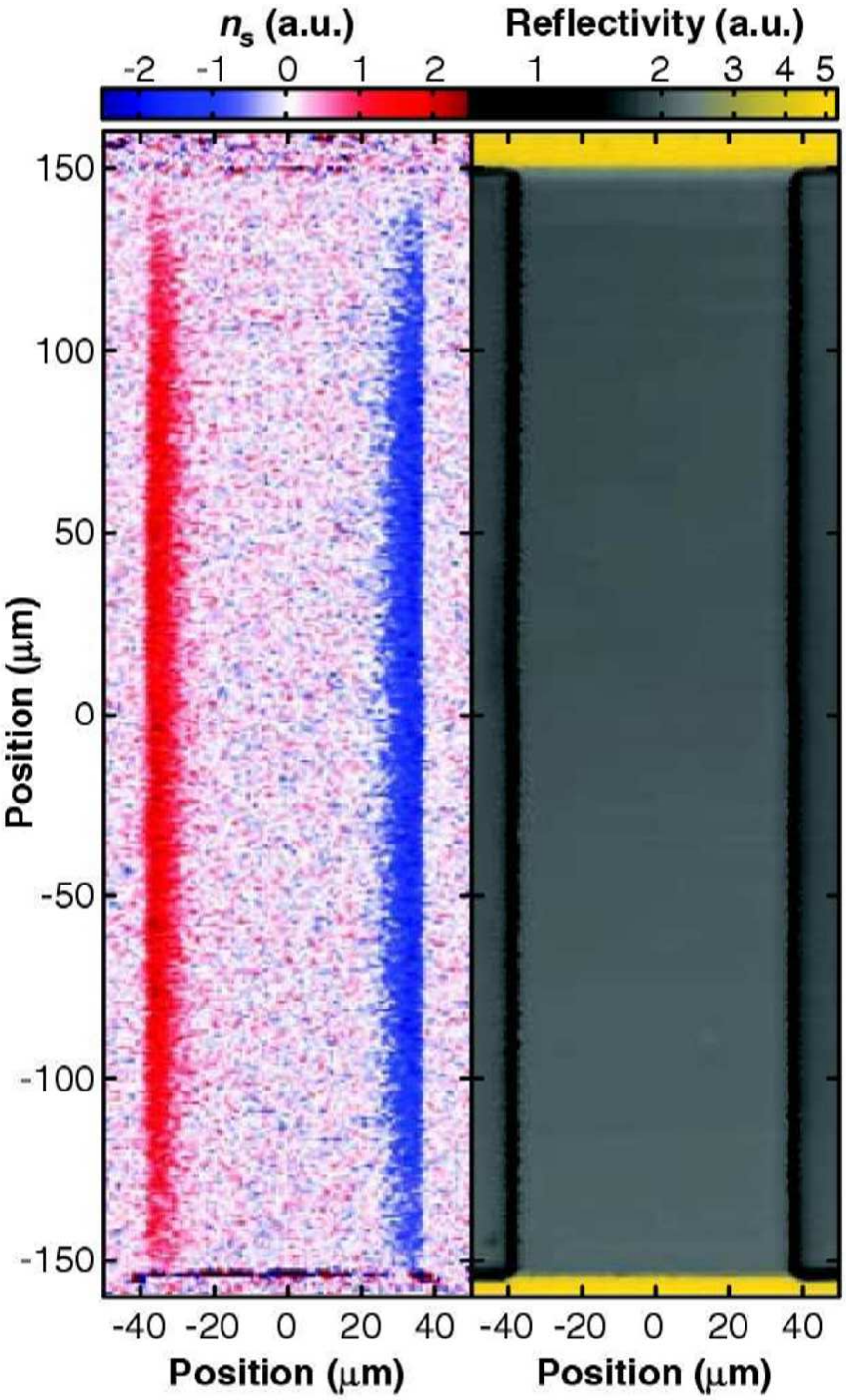


**Figure 6.6**: First experimental demonstration of Spin Hall effect. Distribution of the spin density imaged in Ref. [20] with the help of the Kerr effect.

$m$ is the electron mass, and dimensionless parameter

$$\nu = \frac{2m\alpha^2}{\hbar^2\Delta_Z}, \tag{6.4}$$

measures the relative strength of SO and Zeeman couplings. Without confinement, the two branches of the spectrum and corresponding spinors are given by

$$W_{1,2}(P,Q) = P^2 + Q^2 \pm 2\nu\sqrt{(1-P)^2+Q^2}, \tag{6.5}$$

$$u_{1,2}(P,Q) = \frac{1}{\sqrt{2}} \begin{pmatrix} \frac{2i\nu(1-P+iQ)}{P^2+Q^2-W_{1,2}} \\ \\ 1 \end{pmatrix}, \tag{6.6}$$

where $W$ is the energy in the units of $E_0$. Note that Eqs. (6.5), (6.6) are the dimensionless form of Eqs. (5.5), (5.6). Specifics of size quantization of a matrix Hamiltonian Eq. (6.2) is that for given energy, $W$, and longitudinal momentum, $P$, there are *four* values of the transverse momentum: two positive

$$Q_{1,2} = \sqrt{W + 2\nu^2 - P^2 \pm 2\nu\sqrt{W - 2P + 1 + \nu^2}}, \tag{6.7}$$

and two negative, $-Q_1$, $-Q_2$. Nontriviality of the dispersion, Eq. (6.5), is illustrated in Fig. 5.2, where we plot $Q(P)$ curves (Fermi surfaces) for $\nu = 0.1$ (for weak SO and several values of $W$). Fermi surfaces have a peculiar shape near $W = 1$, as seen from Fig. 5.2. Fermi surfaces corresponding to two branches appear to "meet" near $P = 1$. Then zooming in at this point uncovers a nontrivial evolution of Fermi surfaces, as shown in Fig. 5.3. True "meeting" takes place at $W = 1$, shown in a thick-blue line, while for $W$ slightly greater than one, dashed-red line curves, or slightly less than one, thin-purple curves, the two branches have infinite slope at $Q = 0$. It is not obvious how this effect will manifest in size-quantization in the presence of confinement, to which we now turn.

## 6.3 Arbitrary confinement: general relations

Our objective is to study the size-quantization effect for the spectrum Eq. (6.7). We assume that electrons are confined by the potential $V(y)$ in the $y$-direction, where $V(y)$ is measured in the units $E_0$ and $y$ is measured in the units of $2\alpha/\Delta_Z$, which is the inverse

momentum. Without spin-orbit coupling and Zeeman splitting, the general form of the dispersion is

$$W_n^{(0)}(P) = \mathcal{E}_n + P^2, \tag{6.8}$$

where the $\mathcal{E}_n$ are the eigenvalues corresponding to

$$-\frac{\partial^2 \phi_n}{\partial y^2} + V(y)\phi_n = \mathcal{E}_n \phi_n. \tag{6.9}$$

The second term in Eq. (6.8) describes the kinetic energy of the longitudinal motion. Naturally, without SO coupling, we have $W_n^{(0)}(P) = W_n^{(0)}(-P)$. At finite $SO$ coupling this relation breaks.

It is obvious that for small $\nu \ll 1$, the true dispersion curves $W_n(P)$ are close to $W_n^{(0)}(P)$. For large $\nu$, the separation of transverse and longitudinal motions is impossible, so that the shapes of the size-quantization wave-functions depend strongly on $P$. Our most important finding is that near the "compensation" point $P = 1$, we can find the dispersion law and calculate the absorption matrix element for *arbitrary* SO coupling strength. To achieve this goal, we developed a procedure similar to gauging out of the SO coupling. Previously, this procedure was introduced for homogeneous 2D gas in Ref. [24] and for a quantum dot in Refs. [25, 26]. In application to a quantum wire, this procedure goes as follows. We start with the Schröodinger equation for the components of the spinor

$$-\frac{\partial^2 \Psi_1}{\partial y^2} + \Big[V(y) + P^2 - W\Big]\Psi_1 + 2i\nu(1-P)\Psi_2 + 2i\nu\frac{\partial \Psi_2}{\partial y} = 0, \tag{6.10}$$

$$-\frac{\partial^2 \Psi_2}{\partial y^2} + \Big[V(y) + P^2 - W\Big]\Psi_2 - 2i\nu(1-P)\Psi_1 + 2i\nu\frac{\partial \Psi_1}{\partial y} = 0. \tag{6.11}$$

For symmetric confinement, the functions $\Psi_1$ and $\Psi_2$ do not posses symmetry, but the functions

$$H_1 = \frac{1}{2}\Big[\exp(-i\nu y) + i\exp(i\nu y)\Big]\Psi_1(y) + \frac{1}{2}\Big[\exp(-i\nu y) - i\exp(i\nu y)\Big]\Psi_2(y), \tag{6.12}$$

$$H_2 = -\frac{1}{2}\Big[\exp(-i\nu y) - i\exp(i\nu y)\Big]\Psi_1(y) - \frac{1}{2}\Big[\exp(-i\nu y) + i\exp(i\nu y)\Big]\Psi_2(y), \tag{6.13}$$

do possess symmetry. If $H_1$ is symmetric, then $H_2$ is antisymmetric and vice versa. The meaning of the factors $\exp(i\nu y)$ and $\exp(-i\nu y)$ is the SO phase, similar to Ref. [24]. Taking the inverse transform, we get

$$\Psi_1 = \frac{1}{2}\Big[\exp(i\nu y) - i\exp(-i\nu y)\Big]H_1 - \frac{1}{2}\Big[\exp(i\nu y) + i\exp(-i\nu y)\Big]H_2, \tag{6.14}$$

$$\Psi_2 = \frac{1}{2}\Big[\exp(i\nu y) + i\exp(-i\nu y)\Big]H_1 - \frac{1}{2}\Big[\exp(i\nu y) - i\exp(-i\nu y)\Big]H_2. \qquad (6.15)$$

Upon substitution of Eqs. (6.14), (6.15) into Eqs. (6.10), (6.11), we get the system of two coupled equations

$$-\frac{\partial^2 H_1}{\partial y^2} + \Big[V(y) + P^2 - W - \nu^2 - 2\nu(1-P)\cos 2\nu y\Big]H_1 = -2i\nu(1-P)\sin(2\nu y)H_2, \quad (6.16)$$

$$-\frac{\partial^2 H_2}{\partial y^2} + \Big[V(y) + P^2 - W - \nu^2 + 2\nu(1-P)\cos 2\nu y\Big]H_2 = 2i\nu(1-P)\sin(2\nu y)H_1. \quad (6.17)$$

The advantage of this form over Eqs. (6.10), (6.11) is that the SO phase is gauged out, in the sense that Eqs. (6.16), (6.17) do not contain a first derivative, with respect to $y$. As a price of getting rid of the first derivative the terms $\nu(1-P)\cos 2\nu y$ and $\nu(1-P)\sin 2\nu y$ appear in Eqs. (6.16), (6.17). It is important that, even for large $\nu$, these terms are small in the vicinity of $P = 1$. This suggests that for calculation of the absorption matrix element near $P = 1$, we can treat these terms perturbatively. This is what we do below.

### 6.3.1 Perturbation theory

We start with the observation that precisely at $P = 1$, the two Eqs. (6.16), (6.17) get decoupled, so that

$$W_n(1) = 1 - \nu^2 + \mathcal{E}_n, \qquad (6.18)$$

*exactly*. This means that the size-quantized dispersion curves constitute pairs, $W_n^+(P)$, and $W_n^-(P)$, which cross at $P = 1$.

For finite $(1 - P)$, one should search for solutions of the system Eqs. (6.16), (6.17) in the form of expansion

$$H_1(y) = \sum_n c_n\phi_n(y), \qquad H_2(y) = \sum_n d_n\phi_n(y), \qquad (6.19)$$

so that the coefficients satisfy the following relations

$$c_n\Big(\mathcal{E}_n + P^2 - W - \nu^2\Big) - 2\nu(1-P)\sum_{n'}\kappa_{nn'}c_{n'} = -2i\nu(1-P)\sum_{n'}\gamma_{nn'}d_{n'}, \qquad (6.20)$$

$$d_n\Big(\mathcal{E}_n + P^2 - W - \nu^2\Big) + 2\nu(1-P)\sum_{n'}\kappa_{nn'}c_{n'} = 2i\nu(1-P)\sum_{n'}\gamma_{nn'}d_{n'}, \qquad (6.21)$$

where the matrix elements $\gamma_{nn'}$ and $\kappa_{nn'}$ are defined as

$$\kappa_{nn'} = \int dy\ \phi_n\phi_{n'}\cos 2\nu y, \qquad \gamma_{nn'} = \int dy\ \phi_n\phi_{n'}\sin 2\nu y. \qquad (6.22)$$

For small $(1-P)$ values, we can retain only the terms $n=n'$, which yields

$$W_n^{+,-}(P)=P^2+\mathcal{E}_n-\nu^2\pm 2\nu|1-P|\Big(\kappa_{nn}^2+\gamma_{nn}^2\Big)^{1/2}. \tag{6.23}$$

We see that the splitting, $W_n^+-W_n^-$, is linear in $(1-P)$. Note that when $(1-P)$ is not small but $\nu$ is small, Eq. (6.23) still applies.

The above calculation can be straightforwardly extended to the case when the magnetic field is rotated about $y$-axis by the angle $\Phi$. The result reads

$$W_n^{+,-}(P)=P^2+\mathcal{E}_n-\nu^2\pm 2\nu\Big[(\cos\Phi-P)^2\big(\kappa_{nn}^2+\gamma_{nn}^2\big)+\sin^2\Phi\Big]^{1/2}. \tag{6.24}$$

The above accuracy, i.e., setting $n=n'$, while yielding the dispersion law, is still insufficient to calculate the absorption matrix element. Formally, this follows from the general form of the matrix element

$$M=\frac{1}{2}\int dy\Big(\Psi_1^{*(i)}y\Psi_1^{(f)}+\Psi_2^{*(i)}y\Psi_2^{(f)}\Big), \tag{6.25}$$

where $\Psi_1^{(i)}$, $\Psi_2^{(i)}$ are the components of the spinor of the initial state and $\Psi_1^{(f)}$, $\Psi_2^{(f)}$ are corresponding components of the final state. Within our approximation, all $\Psi$ are proportional to $\phi_n$ and thus, the matrix element is zero. This suggests that one has to go to the next approximation and admix the terms proportional to $\phi_n'$ with $n'\neq n$ to $H_1$ and $H_2$. Note that the matrix element, $M$, can be expressed directly through functions $H_1$ and $H_2$ as follows

$$M=\frac{1}{2}\int dy\Big(H_1^{*(i)}yH_1^{(f)}+H_2^{*(i)}yH_2^{(f)}\Big). \tag{6.26}$$

Assume now that $\Phi=0$, in the zero order, the initial and final states are

$$\begin{pmatrix} H_1^{(i)} \\ \\ H_2^{(i)} \end{pmatrix}=\begin{pmatrix} \phi_n(y) \\ \\ 0 \end{pmatrix},\qquad \begin{pmatrix} H_1^{(f)} \\ \\ H_2^{(f)} \end{pmatrix}=\begin{pmatrix} 0 \\ \\ \phi_n(y) \end{pmatrix}, \tag{6.27}$$

respectively. Obviously, the matrix element is zero and we need to include states with $n\neq n'$. In the first order the initial state and final state read

$$\begin{pmatrix} H_1^{(i)} \\ \\ H_2^{(i)} \end{pmatrix}=\begin{pmatrix} \phi_n(y) \\ \\ \sum_{m\neq n}\left(\frac{2i\nu(1-P)}{\mathcal{E}_m-\mathcal{E}_n}\right)\gamma_{nm}\phi_m(y) \end{pmatrix}, \tag{6.28}$$

$$\begin{pmatrix} H_1^{(f)} \\ \\ H_2^{(f)} \end{pmatrix}=\begin{pmatrix} \sum_{m\neq n}\left(-\frac{2i\nu(1-P)}{\mathcal{E}_m-\mathcal{E}_n}\right)\gamma_{nm}\phi_m(y) \\ \\ \phi_n(y) \end{pmatrix}. \tag{6.29}$$

Then the matrix element reads

$$M = -4i\nu(1-P)\sum_{m\neq n}\frac{\gamma_{nm}y_{nm}}{\mathcal{E}_n-\mathcal{E}_m}, \tag{6.30}$$

where

$$y_{nm} = \int dy\phi_n y\phi_m. \tag{6.31}$$

Equation (6.30) is the main result of the present section. It expresses the absorption matrix element in the vicinity of $P = 1$ via the size-quantization wave functions $\phi_n$ and energies $\mathcal{E}_n$ in the absence of the SO coupling. Note, that, in addition to dimensionless coupling strength, $\nu$, in front of the sum, Eq. (6.30) contains another nontrivial dependence on $\nu$, which is incorporated in the integrand of $\gamma_{nm}$ via SO phase factor $\sin 2\nu y$. In this regard, Eq. (6.30) is more general than the analogous equation obtained in Ref. [26] for a quantum dot with parabolic confinement in the presence of Zeeman field.

For small $\nu$, we have $\gamma_{nm} = 2\nu y_{mn}$. Then the sum in Eq. (6.30) reduces to polarizability of the state $n$, while the $\nu$-dependence of $M$ is $M \propto \nu^2$. In particular, for parabolic confinement, $y_{mn}$ is nonzero only for $m = n \pm 1$. Then the $n$-dependence disappears from Eq. (6.30) since $(y^2_{n+1,n} - y^2_{n,n-1})$ does not contain $n$.

We will use Eq. (6.30) later in calculation of the absorption spectrum.

## 6.4 Absorption

In this section, we examine the absorption of interband transitions by applying an oscillating electric field, which we consider perturbatively. By Fermi's Golden Rule, allowed transitions are determined by the dipole matrix element. Then the transition probability between an initial and final states reads

$$\lambda_{if} = \left(\frac{2\pi}{\hbar}\right)\rho^i_K|M_{if}|^2. \tag{6.32}$$

where $\rho^i_k$ is the energy density of states for the final states and $M_{if}$ is the matrix element between the initial and final states. The absorption can be described by a summing over the allowed transitions

$$A(\omega) = \left(\frac{2\pi}{\hbar^2}\right)\sum_k \lambda_{if}\delta(E^i_k - E^f_k - \hbar\omega)\big(1 - e^{-(\omega/T)}\big), \tag{6.33}$$

where the Dirac Delta function ensures that we have a single final level. Specifics of Eq. (6.33) is that the absorption spectrum will consist of several lines corresponding to different size-quantization subbands. In other words, in addition to absorption between

two split subbands, there is absorption corresponding to *lower* subbands, i.e., higher frequencies.

Near the compensation point, $\Delta_Z \approx \Delta_{SO}$, we expect that the absorption lineshape will have a peculiar shape. As stated in the previous section, near the compensation point, the dispersion, $W(P)$, is linear in $P$. Thus, absorption near the compensation point, between two split subbands, can be considered linear. We now turn to our main objective, to study the peculiar shape of the absorption peak near the compensation point.

### 6.4.1 Analytical approach for absorption

In the case where the matrix element remains constant for the interval, $P$, of absorption, we can approximate the pair of subband dispersion curves to be linear, with slopes $\mu$ and $\lambda$, shown in Fig. 6.7. Then the dispersion of the subbands becomes

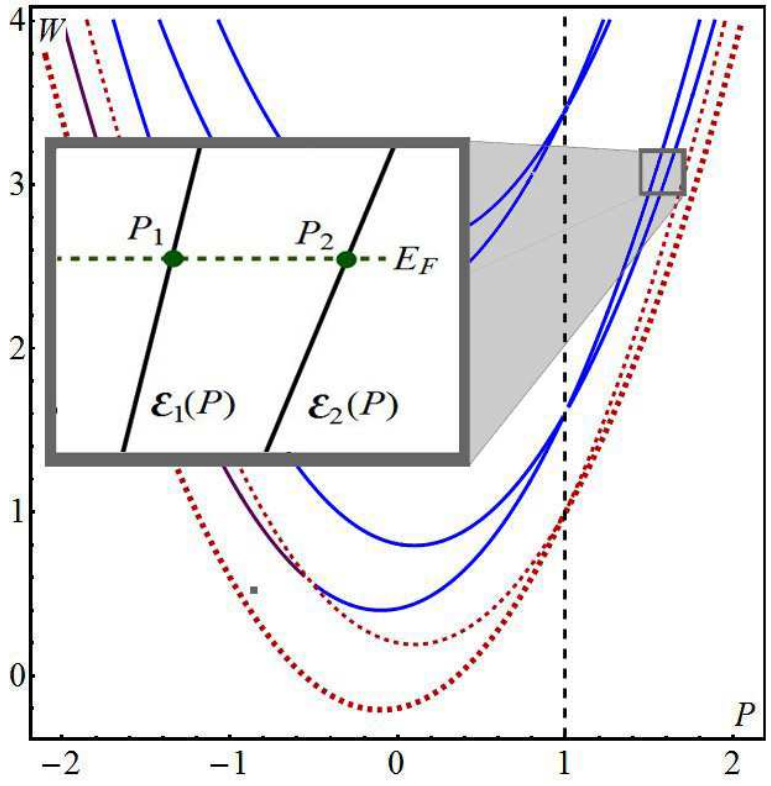


**Figure 6.7**: Energy dispersion plotted from Eq. (6.67) is shown. The inset illustrates how the dispersion behaves linearly with $P$, near the compensation point, $P = 1$, as discussed in Section 2.4.1.

$$\mathcal{E}_1(P) = E_F + \lambda(P - P_1), \tag{6.34}$$

$$\mathcal{E}_2(P) = E_F + \mu(P - P_2). \tag{6.35}$$

For simplification reasons, we first calculate the absorption at zero temperature, $T$. Then the absorption can be written as a peak about $\omega$ with finite width, which reads

$$A(\omega) = \omega|M|^2 \int dp\ \delta\Big(\mathcal{E}_2(P) - \mathcal{E}_1(P) - \omega\Big)\theta(P - P_2)\,\theta(P_1 - P). \tag{6.36}$$

Note that both $T$ and $\omega$ are measured in dimensionless units. Evaluating the integral gives

$$A(\omega) = \frac{\omega|M|^2}{|\mu - \lambda|}\theta\Big(\omega - \lambda(P_1 - P_2)\Big)\,\theta\Big(\mu(P_1 - P_2) - \omega\Big). \tag{6.37}$$

We define the absorption frequency $\omega_0$ as

$$\omega_0 = \frac{\mu + \lambda}{2}\big(P_1 - P_2\big). \tag{6.38}$$

Using the substitution $\omega = \omega_0 + \delta\omega$, we get

$$A(\delta\omega) = \frac{\omega_0|M|^2}{|\mu - \lambda|}\theta\left(1 - \left|\frac{\delta\omega}{\omega_1}\right|\right), \tag{6.39}$$

the final absorption equation for zero temperature, where

$$\omega_1 = \frac{\mu - \lambda}{2}\big(P_1 - P_2\big). \tag{6.40}$$

The absorption spectra consists a peak about $\omega_0$ having width $2\omega_1 \ll \omega_0$. Note that Eq. (6.39) has a similar form to the optical conductance in Part I Chapter 1, Eq. (5.20), and to Ref. [29]. Note the absorption spectra contains at least two peaks with finite width, one for $P > 0$ and the other from $P < 0$. Turning to finite temperature, the population of the lower and upper states are now described using Fermi-statistics. The absorption spectra now reads

$$A(\omega) = \omega|M|^2\Big(1 - e^{-(\omega/T)}\Big)\int dp\ \delta\Big(\mathcal{E}_2(P) - \mathcal{E}_1(P) - \omega\Big)\Big[1 - n\big(\mathcal{E}_2(P)\big)\Big]n\big(\mathcal{E}_1\big(P\big)\big), \tag{6.41}$$

where $n$ is the Fermi-Dirac distribution. Evaluating the integral gives

$$A(\delta\omega) = \frac{\omega_0|M|^2}{4|\mu - \lambda|}\left(\frac{\sinh\left(\frac{\omega_0}{2T}\right)e^{(\delta\omega)/2T}}{\cosh\left[\frac{\lambda\omega_0}{2(\mu+\lambda)T}\left(1 - \frac{\delta\omega}{\omega_1}\right)\right]\cosh\left[\frac{\mu\omega_0}{2(\mu+\lambda)T}\left(1 + \frac{\delta\omega}{\omega_1}\right)\right]}\right). \tag{6.42}$$

It can be seen that as $T \to 0$, Eq. (6.42) reproduces Eq. (6.39). At finite temperature, the shape of the peak depends on the relation between $T$ and $\omega_0$. Defining the constant $t = T/\omega_0$, the dependence of $A(\delta\omega)$ on $t$ can be approximated as

$$A(x) \propto \frac{1}{\cosh\left[\frac{1}{4t}\big(1 - x\big)\right]\cosh\left[\frac{1}{4t}\big(1 + x\big)\right]}, \tag{6.43}$$

where the dimensionless parameter $x$ is defined as $\delta\omega/\omega_1$. We used the relationship that $\omega_1 \ll \omega_0$, then $\exp[1/2t + (\omega_1/\omega_0)(x/2T)]$ becomes simply $\exp(1/2t)$. Equation (6.43) is illustrated in Fig. 6.8 for three characteristic temperatures. In plotting, it is sufficient to set $\mu = \lambda$ in the lowest approximation, which we will show later. For temperatures $T \ll \omega_0$, the peak is only slightly rounded near the edges, $\omega = \pm\omega_1$, namely, with interval $|\delta\omega \pm \omega_1| \sim T\omega_1/\omega_0 \ll \omega_1$. Upon increasing $T$, at $T \gg \omega_0$, the peak is still well defined but its width, $T\omega_1/\omega_0$, remaining smaller than $\omega_0$, exceeds $\omega_1$.

Subsequently, the slopes for $\mu$ and $\lambda$ can be determined in the lowest order. Recall we derived $W_n^{\pm}$, Eq. (6.23), for arbitrary confinement. Then the slopes for $\mu$ and $\lambda$ can be determined by taking the derivate of Eq. (6.23) with respect to $P$, which gives

$$\lambda = 2P - 2\nu(\kappa_{nn}^2 + \gamma_{nn}^2)^{1/2}, \tag{6.44}$$

$$\mu = 2P + 2\nu(\kappa_{nn}^2 + \gamma_{nn}^2)^{1/2}. \tag{6.45}$$

Further, by substituting $\mu$ and $\lambda$, we can estimate $\omega_1$ and $\omega_0$ as

$$\omega_1 = 2\nu(\kappa_{nn}^2 + \gamma_{nn}^2)^{1/2}(P_1 - P_2), \tag{6.46}$$

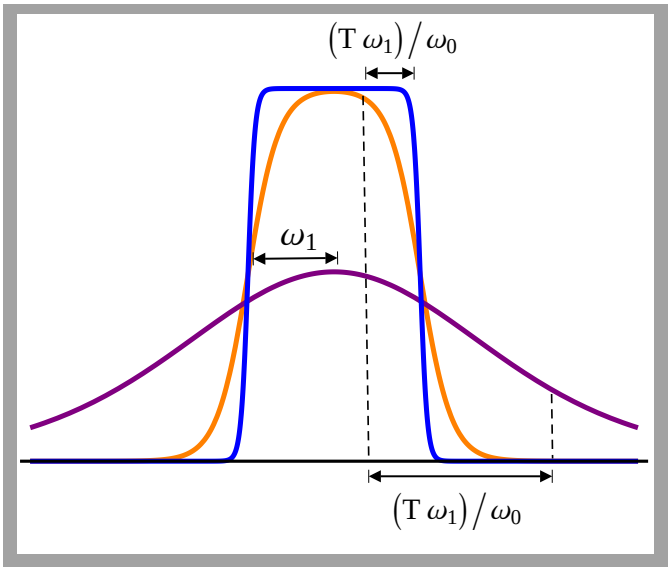


**Figure 6.8**: The absorption lineshape is plotted from Eq. (6.43) for three characteristic temperatures. In the low temperature limit, $T \ll \omega_0$ (blue) the edges are slightly rounded within the interval $\omega \pm \omega_1 = T\omega_1/\omega_0$. Upon increasing $T$ further, (orange) we see that the edges become more rounded with interval approaching the width $\omega_1$ of the peak. In the high $T$ limit (blue), at $T \gg \omega_0$, the peak is still well defined but its width, $T\omega_1/\omega_0$, remaining smaller than $\omega_0$ exceeds $\omega_1$.

$$\omega_0 = 2P(P_1 - P_2), \tag{6.47}$$

respectively.

Equation (6.42) was derived under the assumption that $P_1$ and $P_2$ are different. This assumption is violated when the Fermi-level position corresponds to $P = 1$. At this point, both $\omega_0$ and $\omega_1$ equal zero. In the zero temperature limit, absorption does not occur. As temperature increases, we anticipate the absorption to be non-zero. At $P = 1$, the absorption, Eq. (6.42), reads

$$A(\delta\omega) = \frac{\delta\omega|M|^2}{4T|\mu - \lambda|}\left(\frac{\delta\omega\ e^{\delta\omega/2T}}{\cosh\left[\frac{\lambda\delta\omega}{2(\mu+\lambda)T}\right]\cosh\left[\frac{\mu\delta\omega}{2(\mu+\lambda)T}\right]}\right). \tag{6.48}$$

Note that in taking the integral of the Dirac Delta, Eq. (6.41), $P$ was replaced with $P = 1 + \delta\omega/(\mu + \lambda)$. Thus, $(1 - P)$ in matrix element $M$, Eq. (6.25), should be replaced with $\delta\omega/(\mu + \lambda)$. We assume that the relation $\delta\omega \ll T$. Then Eq. (6.48) can be written as

$$A(\delta\omega) \approx \frac{\nu^2}{16\lambda^2 T|\mu - \lambda|}\left(\sum_{m\neq n}\frac{\gamma_{nm}y_{nm}}{\epsilon_n - \epsilon_m}\right)^2 \frac{\delta\omega^4}{\left[\cosh\left(\delta\omega/4T\right)\right]^2} \tag{6.49}$$

where we have used the the fact that $\mu \approx \lambda$ in the argument of hyperbolic cosine. Remarkably, from Eq. (6.49), we see that as temperature increases, the absorption peak position increases in frequency. Consider the dispersion curves for intermediate $\nu$, Fig. 6.9, with $E_F$ corresponding to $P = 1$. The absorption spectrum consists of two peaks. The first peak results from the region $P < 0$, described by Eq. (6.42), remains stationary as $T$ increases. The second absorption peak, occurring at a smaller frequency than the first, corresponds to $P = 1$, and increases in frequency as temperature increases.

Among the variety of confining potentials, $V(y)$, there is one example when finitie spin-orbit coupling and Zeeman splitting can be incorporated into the size-quantization fully, on a non-perturbative level. This rigid confinement is described hard walls at $\pm a$. Besides being exactly solvable, this confinement is relevant for wide quantum wires.

## 6.5 Rigid walls: derivation of the dispersion equation

The boundaries $y = \pm d/2$, Fig. 6.1, mix each of the two incident waves with both reflected waves. The general form of the wavefunction

$$\Psi(y) = \left\{\begin{array}{c} \lambda_1 e^{iQ_1 y} + \lambda_2 e^{iQ_2 y} + \lambda_3 e^{-iQ_1 y} + \lambda_4 e^{-iQ_2 y} \\ \\ g_1\lambda_1 e^{iQ_1 y} + g_2\lambda_2 e^{iQ_2 y} + g_3\lambda_3 e^{-iQ_1 y} + g_4\lambda_4 e^{-iQ_2 y} \end{array}\right\},$$

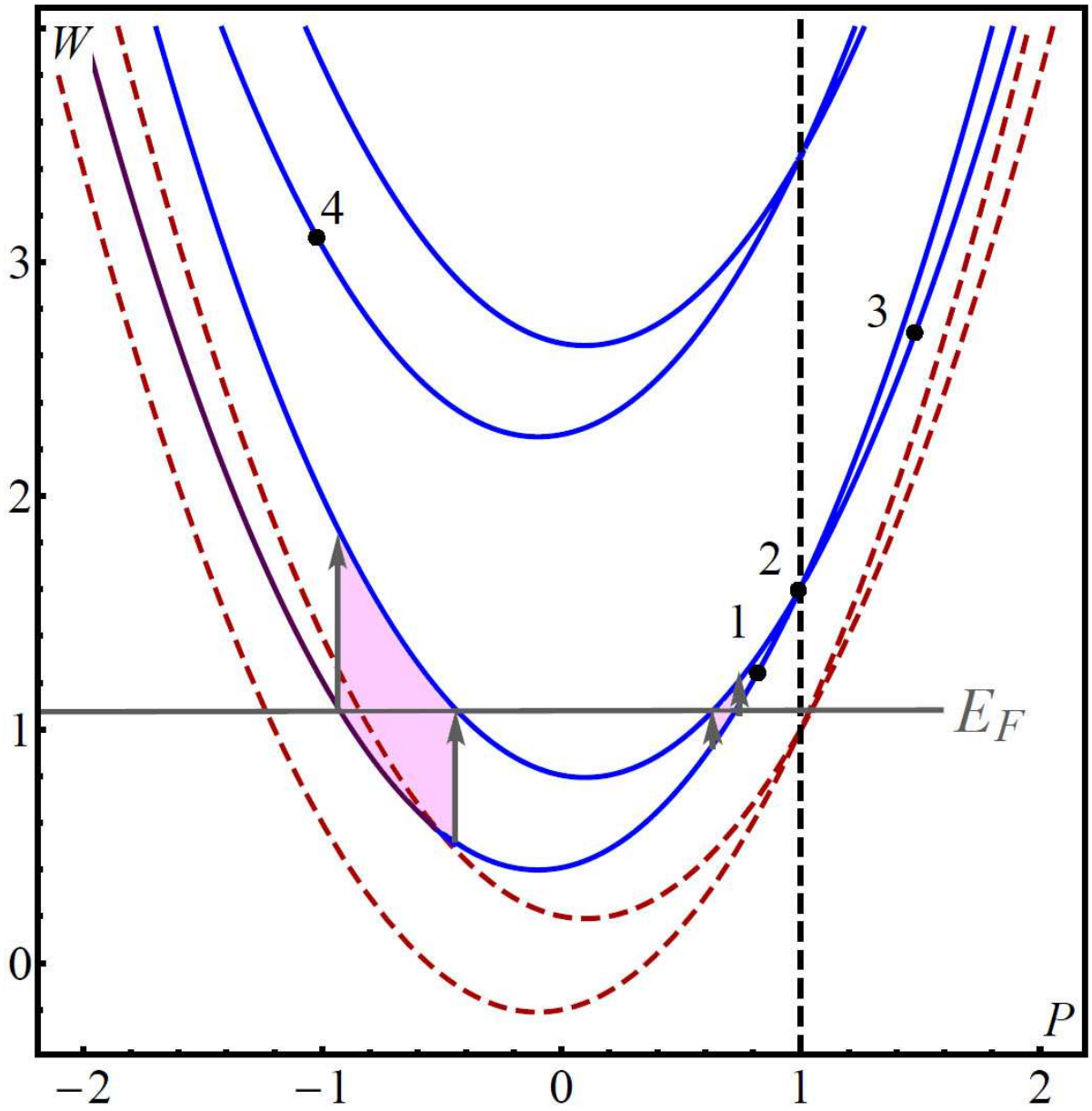


**Figure 6.9**: Energy dispersion defined in Eq. (6.67) is plotted as function $P$ for the intermediate value of $\nu$, $\nu = 0.1$, and for $a = 2$. In addition, we plotted two red dashed curves, Eq. (6.71). The energy dispersion is shown in blue for both $Q_1$ and $Q_2$ real, and in purple when $Q_2$ becomes imaginary.

(6.50)

is a linear combination of two incident and reflected waves, where $g_1$, $g_2$, $g_3$, $g_4$ are defined as

$$g_1 = \frac{P^2 + Q_1^2 - W_1(Q_1)}{2i\nu\Big[(1-P) + iQ_1\Big]}, \qquad g_2 = \frac{P^2 + Q_2^2 - W_1(Q_2)}{2i\nu\Big[(1-P) + iQ_2\Big]}, \tag{6.51}$$

$$g_3 = \frac{P^2 + Q_1^2 - W_1(Q_1)}{2i\nu\Big[(1-P) - iQ_1\Big]}, \qquad g_4 = \frac{P^2 + Q_2^2 - W_1(Q_2)}{2i\nu\Big[(1-P) - iQ_2\Big]}. \tag{6.52}$$

The form of Eq. (6.51), (6.52) follows from Eq. (6.2). The relation between $\lambda_1$, $\lambda_2$, $\lambda_3$ and $\lambda_4$ are determined by the boundary conditions. The derivation can be found in the Appendix. Upon imposing the hard-wall boundary conditions $\Psi(-a) = \Psi(a) = 0$, where

$$a = \frac{\Delta_Z d}{4\alpha} \tag{6.53}$$

is the dimensionless width of the wire, we obtain four coupled equations,

$$\lambda_1 e^{\,iQ_1 a} + \lambda_2 e^{\,iQ_2 a} + \lambda_3 e^{-iQ_1 a} + \lambda_4 e^{-iQ_2 a} = 0, \tag{6.54}$$

$$g_1\lambda_1 e^{\,iQ_1 a} + g_2\lambda_2 e^{\,iQ_2 a} + g_3\lambda_3 e^{-iQ_1 a} + g_4\lambda_4 e^{-iQ_2 a} = 0, \tag{6.55}$$

$$\lambda_1 e^{-iQ_1 a} + \lambda_2 e^{-iQ_2 a} + \lambda_3 e^{\,iQ_1 a} + \lambda_4 e^{\,iQ_2 a} = 0, \tag{6.56}$$

$$g_1\lambda_1 e^{-iQ_1 a} + g_2\lambda_2 e^{-iQ_2 a} + g_3\lambda_3 e^{\,iQ_1 a} + g_4\lambda_4 e^{\,iQ_2 a} = 0. \tag{6.57}$$

If we replace $a$ with $-a$, Eqs. (6.56), (6.57) transform into (6.54), (6.55) and vice versa. Using this fact, we will only show the reduction of Eqs. (6.54), (6.55). To derive the dispersion equation it is convenient to first divide Eq. (6.55) by $g_1$ and subtracting Eqs. (6.54), (6.55), we find

$$\lambda_2 e^{iQ_2 a}\left(1 - \frac{g_2}{g_1}\right) + \lambda_3 e^{-iQ_1 a}\left(1 - \frac{g_3}{g_1}\right) + \lambda_4 e^{-iQ_2 a}\left(1 - \frac{g_4}{g_1}\right) = 0. \tag{6.58}$$

Similarly, upon dividing Eq. (6.55) by $g_3$ then subtracting both equations, we get

$$\lambda_1 e^{iQ_1 a}\left(1 - \frac{g_1}{g_3}\right) + \lambda_2 e^{iQ_2 a}\left(1 - \frac{g_2}{g_3}\right) + \lambda_4 e^{-iQ_2 a}\left(1 - \frac{g_4}{g_3}\right) = 0. \tag{6.59}$$

Solving for $\lambda_1$ from Eq. (6.59), and $\lambda_3$ from Eq. (6.58), we find

$$-\lambda_1 = \left(\frac{g_3 - g_2}{g_3 - g_1}\right)\lambda_2 \exp\big[i(Q_2 - Q_1)a\big] + \left(\frac{g_3 - g_4}{g_3 - g_1}\right)\lambda_4 \exp\big[-i(Q_2 + Q_1)a\big], \tag{6.60}$$

$$-\lambda_3 = \left(\frac{g_1 - g_2}{g_1 - g_3}\right)\lambda_2 \exp\big[-i(Q_2 + Q_1)a\big] + \left(\frac{g_1 - g_4}{g_1 - g_3}\right)\lambda_4 \exp\big[-i(Q_2 - Q_1)a\big]. \tag{6.61}$$

Now recall that Eqs. (6.56) and (6.57) will reduce to Eqs. (6.60), (6.61) upon the substitution $a \to -a$, giving

$$-\lambda_1 = \left(\frac{g_3 - g_2}{g_3 - g_1}\right) \lambda_2 \exp\big[-i(Q_2 - Q_1)a\big] + \left(\frac{g_3 - g_4}{g_3 - g_1}\right) \lambda_4 \exp\big[i(Q_2 + Q_1)a\big], \quad (6.62)$$

$$-\lambda_3 = \left(\frac{g_1 - g_2}{g_1 - g_3}\right) \lambda_2 \exp\big[i(Q_2 + Q_1)a\big] + \left(\frac{g_1 - g_4}{g_1 - g_3}\right) \lambda_4 \exp\big[i(Q_2 - Q_1)a\big]. \quad (6.63)$$

Equating Eqs. (6.60), (6.62) and (6.61), (6.63), we get two coupled equations

$$\lambda_2\Big(g_3 - g_2\Big) \sin(Q_2 - Q_1)a + \lambda_4\Big(g_3 - g_4\Big) \sin(Q_2 + Q_1)a = 0, \quad (6.64)$$

$$\lambda_2\Big(g_1 - g_2\Big) \sin(Q_2 + Q_1)a + \lambda_4\Big(g_1 - g_4\Big) \sin(Q_2 - Q_1)a = 0. \quad (6.65)$$

Multiplying Eqs. (6.64) and (6.65) yields the following transcendental equation

$$\left(\frac{g_3 - g_2}{g_3 - g_4}\right) \sin^2(Q_2 + Q_1)a = \left(\frac{g_1 - g_2}{g_1 - g_4}\right) \sin^2(Q_2 - Q_1)a. \quad (6.66)$$

Upon substituting $g_1$, $g_2$, $g_3$, $g_4$ from Eqs. (6.51), (6.52), we arrive to the final form of the equation for the subband dispersion

$$\frac{\sin^2(Q_1 + Q_2)a}{(Q_1 + Q_2)^2}\Big[(1 - P)^2(Q_1 + Q_2)^2 + (W - P^2 + Q_1Q_2)^2\Big] = \frac{\sin^2(Q_1 - Q_2)a}{(Q_1 - Q_2)^2}\Big[(1 - P)^2(Q_1 - Q_2)^2 + (W - P^2 - Q_1Q_2)^2\Big]. \quad (6.67)$$

Equation (6.67) is our main result. Note that Eq. (6.67) is symmetric with respect to $Q_1$, $-Q_2$. Before proceeding to the analysis of solutions of Eq. (6.67), we would like to point out that dispersion Eq. (6.66) applies for a broader class of matrix Hamiltonians. Consider, for example, bilayer graphene. The Hamiltonian describing the low-energy states reads [27]

$$\hat{H} = \begin{pmatrix} \epsilon - \lambda p^2 & (p_x - ip_y)^2 \\ (p_x + ip_y)^2 & -\epsilon + \lambda p^2 \end{pmatrix}. \tag{6.68}$$

Also consider the Hamiltonian for a superconductor

$$\hat{H} = \begin{pmatrix} \frac{\hbar^2}{2m}(k - k_F) & -\Delta \\ \Delta & -\frac{\hbar^2}{2m}(k - k_F) \end{pmatrix}, \tag{6.69}$$

where $\Delta$ is the external pairing potential.

## 6.6 Analysis of dispersion curves

For characteristic $a = 2$, the subband dispersion curves are shown in Figs. 6.9, 6.10, 6.11, and 6.12 for three values of parameter, $\nu$. They are supposed to illustrate the limits of weak, intermediate, and strong SO coupling. The limit $\nu \ll 1$ is easy to comprehend. The curves shown in Fig. 6.10, for $\nu = 0.02$, are close to parabolas,

$$W = P^2 - \nu^2 \pm 2\nu|1 - P| + \frac{n^2\pi^2}{a^2}. \tag{6.70}$$

This follows from Section 6.3, recall the definitions of $\kappa_{nn'}$ and $\gamma_{nn'}$. In the limit of small $\nu$, only the $\kappa_{nn'}$-terms with $n = n'$ are non-zero and equal to one, while all terms for $\gamma_{nn'}$ are zero. Then Eq. (6.23), in Section 6.3, reduces to the above equation, Eq. (6.70). Eventually for large $P$, the splitting of the energy levels becomes $\pm 2\nu P$, demonstrating that spin-orbit coupling, which is proportional to momentum, dominates at large $P$ over Zeeman splitting. For intermediate $\nu = 0.1$, for $P < -1$, Eq. (6.70) does not work. To amplify this deviation, we plot together the dispersion curves, and two additional curves

$$W(P) = P^2 \pm 2\nu|1 - P|, \tag{6.71}$$

which are defined by setting $Q = 0$ in 2D Eq. (6.5), shown as a red-dashed line. When the point $(P, W)$ is above both curves, then both $Q_1$ and $Q_2$ are real. When the point $(P, W)$ is in between the two additional curves, $Q_1$ is real and $Q_2$ is imaginary. Finally, when the point is below both curves, then both $Q_1$ and $Q_2$ are imaginary. Now we see that, while in Fig. 6.10 dispersion curves are above additional curves, in Fig. 6.9, the part of the lower dispersion curve corresponding to negative $P$ falls in between additional curves Eq. (6.71). This part of the dispersion curve is shown in purple. Then it is no surprise that this part cannot be described by Eq. (6.70), derived for $Q_1 = Q_2 = n\pi/a$.

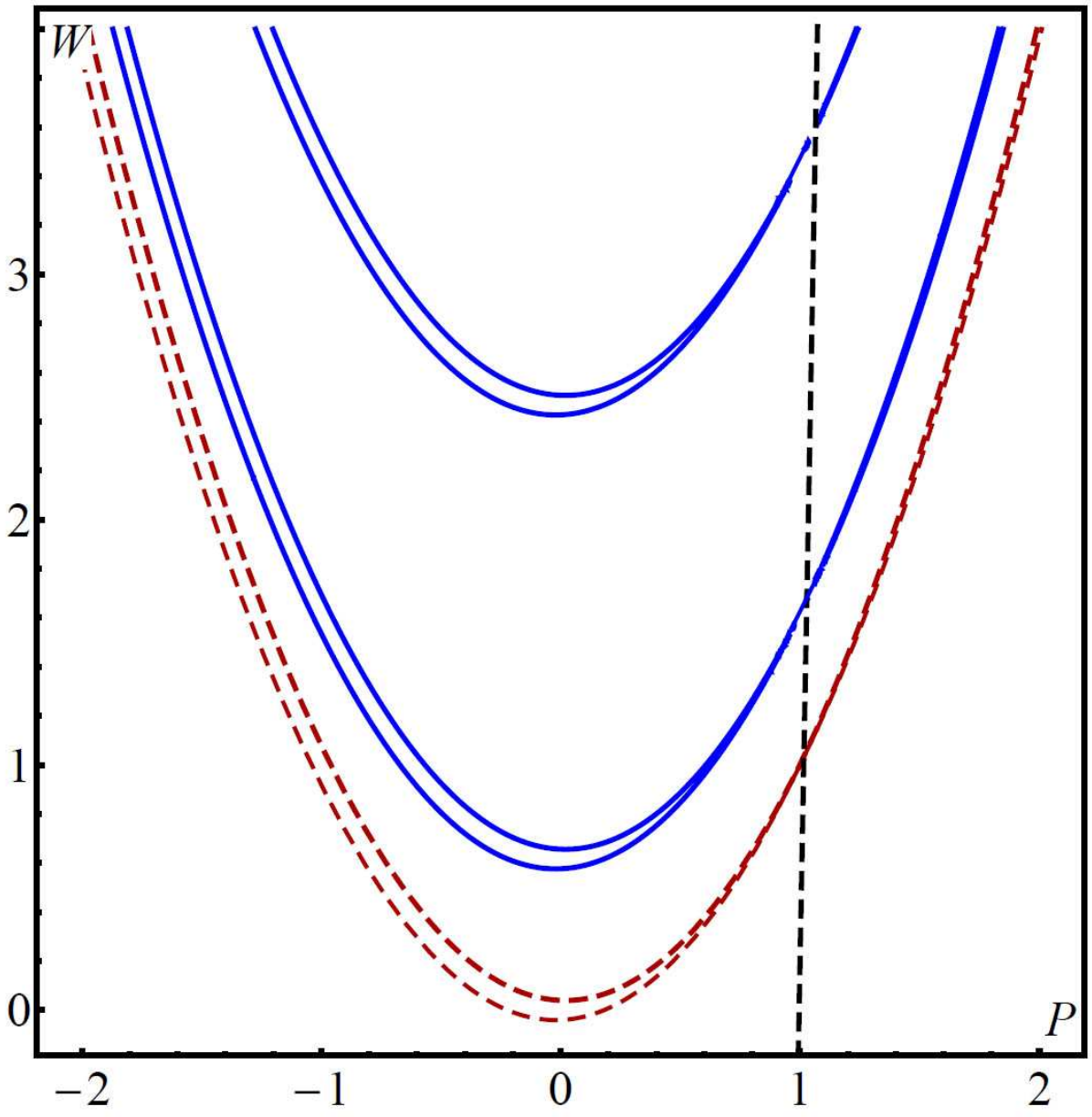


**Figure 6.10**: Energy dispersion defined in Eq. (6.67) is plotted as a function of $P$ for the weak value of $\nu$, $\nu = 0.02$, and for $a = 2$. In addition, we plotted two red dashed curves, Eq. (6.71). The upper red-dashed curve represents the point where $Q_2$ becomes imaginary, while the lower red-dashed curve represents the point where both $Q_1$, $Q_2$ become imaginary. The region where the pair of dispersion curves "meet" at $P = 1$ is noted by the black-dashed line.

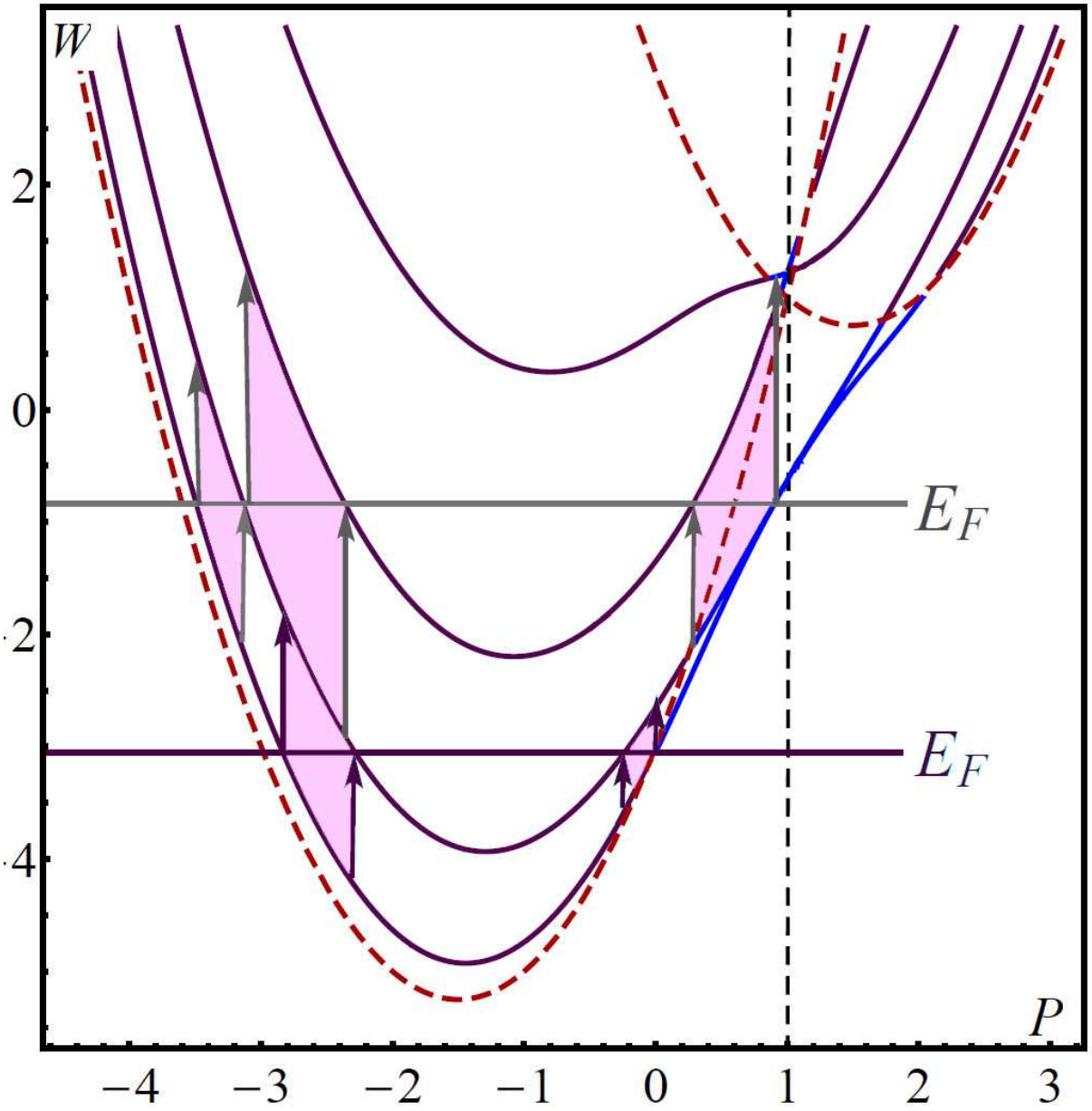


**Figure 6.11**: The same as in 6.10, b, for strong SO coupling, $\nu = 1.5$. The dispersion curves are presented for low energies, $W < 3$. For strong $\nu$, the region of both $Q_1$ and $Q_2$ begin real only exists for the region near $P = 1$. Note that for the lower energies (compare to Fig. 6.12), the neighboring dispersion pairs only intersect at $P = 1$.

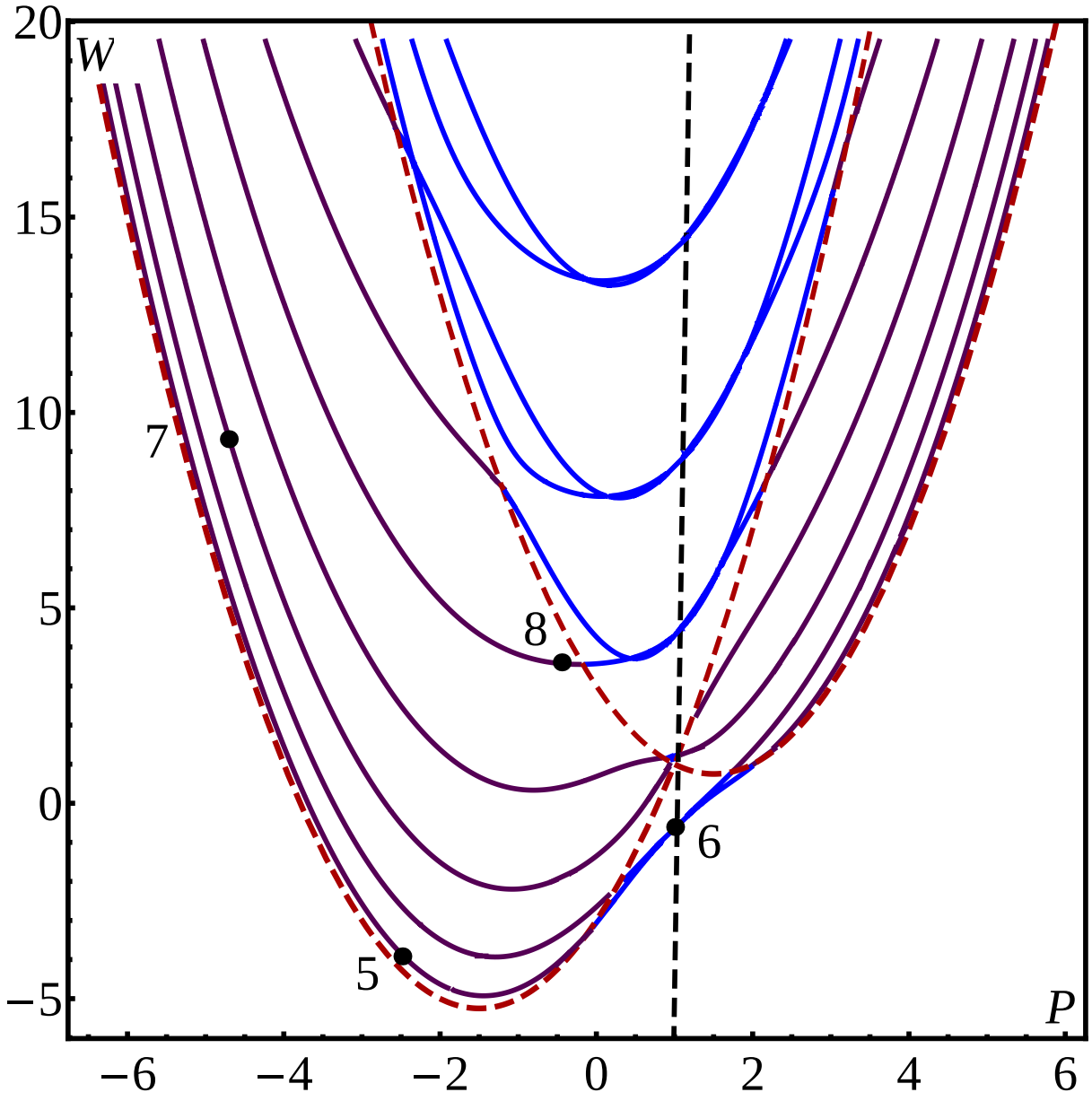


**Figure 6.12**: The same as in Fig. 6.11, for strong SO coupling, $\nu = 1.5$. Dispersion curves are presented for the larger energy scales, $W < 20$. The plot illustrates that in addition to $P = 1$, neighboring dispersion curves also intersect at other values of $P$.

As $P$ becomes more negative, the second lowest dispersion curve, shown in blue, will eventually get in between additional curves, and so on. Finally, as $P$ becomes even more negative, all the curves approach the outermost additional curve, $Q_1 = 0$.

For strong SO coupling, $\nu = 1.5$, the situation changes drastically. Looking at Fig. 6.11, b, one can see that the dispersion curves no longer represent pairs of well-defined branches. Not only do the dispersion curves cross at $P = 1$, but they also cross at other values of $P$. The approximation for $W_n^{\pm}$, Eq (6.23), derived for $n = n'$, applies only in the immediate vicinity of $P = 1$. This is because the function $\cos 2\nu y$ in the integrand of Eq. (6.22) causes strong mixing of subbands at $\nu = 1.5$. For the lowest subband, instead of $\kappa_{11} = 1$, we have $\kappa_{11} = -0.12$ and for the next subband we have $\kappa_{22} = .87$ instead of $\kappa_{22} = 1$. The fact that $\kappa_{22}$ is much bigger than $\kappa_{11}$ explains the difference in slopes between the first and second dispersion neighbors at $P = 1$.

### 6.6.1 Vicinity of $Q_2 = 0$

As the dispersion curve enters the region between two additional curves, $Q_2$ changes from real to purely imaginary. There is a question how to find the position of the entry point, $P = P_c(a, \nu)$, analytically. Turning to Eq. (6.67), we see that at $Q_2 = 0$, it is satisfied identically. Then the condition for the position of the entry point can be found by equating the derivatives of both sides with respect to $Q_2$, and subsequently taking the limit $Q_2 \to 0$. This yields

$$\left(\frac{a}{\tan Q_1 a} - \frac{1}{Q_1}\right)\left[(1-P)^2 Q_1^2 - (W - P^2)^2\right] + (1-P)^2 + Q_1(W - P^2) = 0. \quad (6.72)$$

In derivation of Eq. (6.72), we used the fact that derivatives from both sides of Eq. (6.67) at small $Q_2$ are equal in absolute values and have opposite signs. Thus, Eq. (6.72) expresses the fact that these derivatives are zero at $Q_2 = 0$. This equation should be complemented with two conditions

$$W = P^2 + 2\nu|1 - P|, \quad (6.73)$$

$$Q_1^2 = 4\nu\big(\nu + |1 - P|\big). \quad (6.74)$$

The first condition fixes $P$ on the upper additional curve, while the second condition is the expression for $Q_1$ when the first condition is met. Inserting Eqs. (6.73), (6.74) into

Eq. (6.72), we get a closed equation for $P_c(a,\nu)$. Note that the corresponding values $W_c$ and $Q_{1c}$ can be expressed via $P_c$ using Eqs. (6.73), (6.74). Now from the general relation

$$Q_1^2 Q_2^2 = \big(W - P^2\big)^2 - 4\nu^2(1-P)^2, \tag{6.75}$$

one can conclude that, in vicinity of $Q_2 = 0$, the behavior of $Q_2$ before the entry point is $Q_2 \propto \big(W - W_c(a,\nu)\big)^{1/2}$, while after the entry point, it is $Q_2 \propto i\big(W - W_c(a,\nu)\big)^{1/2}$.

## 6.7 Wavefunction

Since the wavefunctions are spinors, in addition to the probability density, $\mathcal{P}(y) = |\Psi_1(y)|^2 + |\Psi_2(y)|^2$, they are characterized by the distribution of spin projections. We will present numerical results of out of plane

$$\sigma_z(y) = |\Psi_1(y)|^2 - |\Psi_2(y)|^2, \tag{6.76}$$

and the $y$-component projection of spin

$$\sigma_y(y) = -i\Psi_1^*(y)\Psi_2(y) + i\Psi_1(y)\Psi_2^*(y). \tag{6.77}$$

Our numerical results are presented in Fig. 6.13a-d, for $\nu = 0.1$, and in Fig. 6.14a-d, for $\nu = 1.5$. For small $\nu$, the Zeeman coupling dominates over SO coupling. Then only $\sigma_y$ is nonzero and follows the probability distribution $\mathcal{P}(y)$, which follows $\Psi_n^2(y)$. The same trend persists for intermediate $\nu$ away from $P = 1$, point 1 in Fig. 6.9, plotted in Fig. 6.13a. We also see that $\sigma_z(y)$, although small, is an odd function of $y$. Note that, even though $\mathcal{P}(y)$ is an even function of $y$, the components of spinor, $\Psi_1$, $\Psi_2$ are neither symmetric nor antisymmetric. The asymmetry of the wave functions is naturally explained by Eqs. (6.14), (6.15). Functions $H_1$ and $H_2$ are either even or odd, but factors $\exp[i\nu y]$ break the symmetry of $\Psi_1$, $\Psi_2$. Following the first or second dispersion curve from negative to positive $P$ in Fig. 6.9, we see that $\sigma_y(y)$ follows $\mathcal{P}(y)$ in the positive direction for the first dispersion curve and in the negative direction for the second dispersion curve. As soon as we exceed $P = 1$ for the first dispersion curve, $\sigma_y(y)$ flips and follows $\mathcal{P}(y)$ in the negative direction. Similarly, the second dispersion curve flips and follows the positive direction of $\mathcal{P}(y)$. See point 3, Fig. 6.13c. In the close proximity of $P = 1$, both $\sigma_z(y)$ and $\sigma_y(y)$ are small, suggesting that spin is directed along the $x$-axis. See Fig. 6.13a and Fig. 6.14a. Figure 6.13a-d gives us an idea about $\mathcal{P}(y)$, $\sigma_z(y)$, $\sigma_x(y)$ for higher subbands. While $\mathcal{P}(y)$ acquires additional maxima, $\sigma_y(y)$ follows $\mathcal{P}(y)$, and $\sigma_z(y)$ has the same number of zeros as the number of maxima of $\mathcal{P}(y)$, away from $P = 1$. We also see that the amplitude

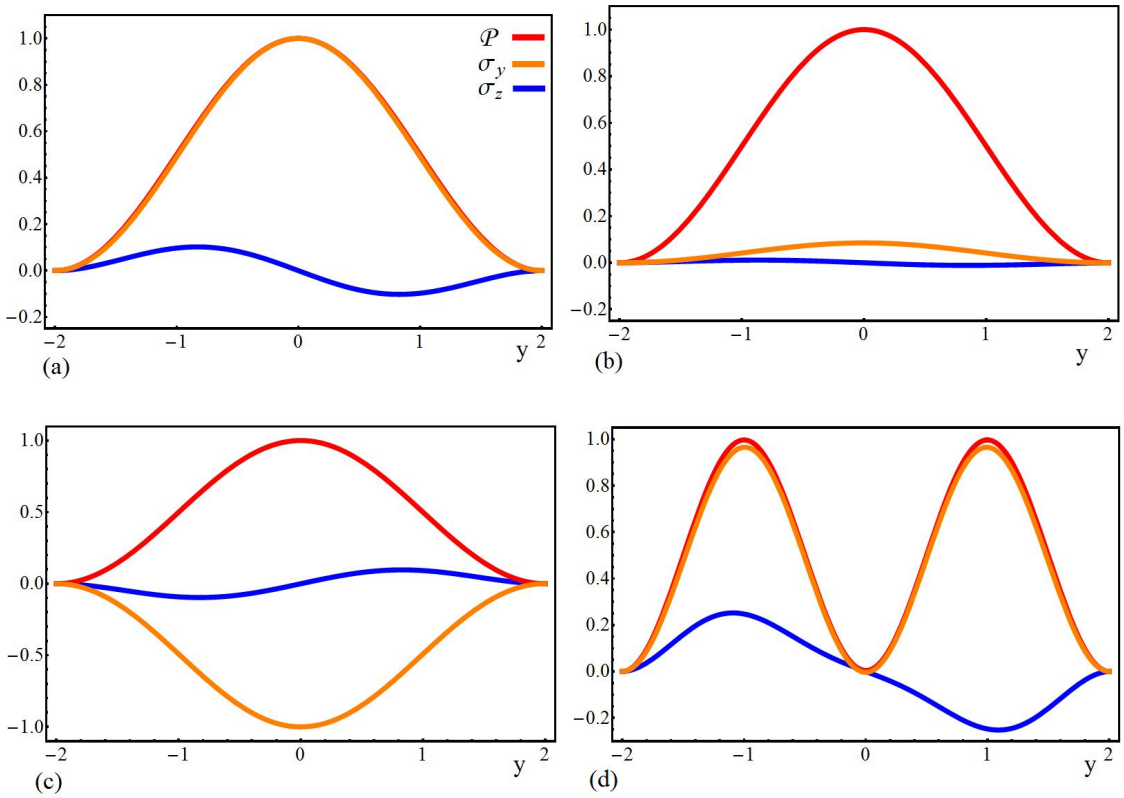


**Figure 6.13**: The probability density, $\mathcal{P}(y)$, and spin projections, $\sigma_y$ and $\sigma_z$, are plotted for intermediate $\nu = 0.1$, shown in red, orange, and blue, respectively. The plots (a, b, c, d) shown above, correspond to the selected points (1, 2, 3, 4) marked in Fig. 6.9, respectively. (a) Shows the spin projection is along the $y$-axis immediately away from $P = 1$. (b) The region in close proximity of $P = 1$, where spin projection is predominantly along the $x$-axis. (c) After exceeding $P = 1$, the spin projection flips to be along the negative $y$-axis. (d) Higher values of $W$ showing the deviation of $\sigma_y(y)$ from $\mathcal{P}(y)$ and the increase in amplitude for $\sigma_z(y)$.

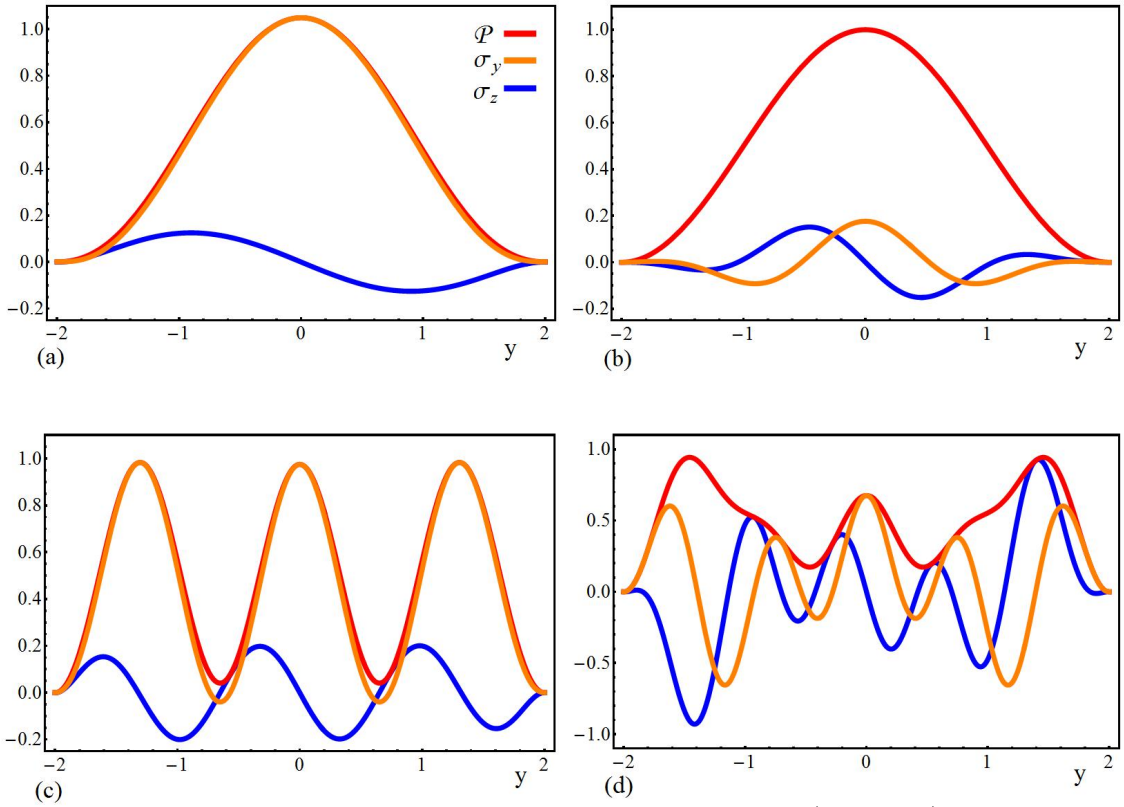


**Figure 6.14**: Similar to Fig. 6.13 for strong $\nu$, where the plots (a, b, c, d) correspond to the points (5, 6, 7, 8) marked in Fig. 6.12, respectively. (a) Shows the region immediately away from $P = 1$. (b) Shows the region in the immediate vicinity of $P = 1$. (c) Higher values of $W$, showing points along the $y$-axis where the total spin projection is along the $z$-axis. (d) In the region near $P = 1$, we see strong deviation from intermediate $\nu$ for $\mathcal{P}(y)$, $\sigma_z(y)$ and $\sigma_y(y)$.

of $\sigma_y(y)$ slightly decreases while the amplitude of $\sigma_z(y)$ slightly increases. See point 4, Fig. 6.13d. Both $\sigma_z(y)$ and $\sigma_y(y)$ are suppressed in the close vicinity of $P = 1$. In the limit of strong SO coupling, $\nu = 1.5$, in the region away from $P = 1$, the numerical plots of $\mathcal{P}(y)$, $\sigma_z(y)$, $\sigma_x(y)$, have similar behavior to intermediate $\nu$. Compare point 5 in Fig. 6.12, plotted in Fig. 6.14a, to point 1, Fig. 6.13a. If we go to higher subbands, away from $P = 1$, we see that there are always several positions along $y$-axis where the spin is predominantly along the $z$-axis. See point 7, Fig. 6.14c. As $P$ approaches the region $P = 1$ from left or right, we see some interesting differences. The probability density, $\mathcal{P}(y)$, does not follow the $\cos^2$-like shape and $\sigma_y(y)$ does not truly follow $\mathcal{P}(y)$, but both remain even-functions. The expectation value $\sigma_z(y)$ is still an odd-function and also departs from its $\sin^2$-like behavior. This can be see at point 8, Fig. 6.14d. In the region $P = 1$, we see the behavior similar to intermediate $\nu$ that $\sigma_y$ and $\sigma_z$ amplitude is always small, suggesting that spin is along the $x$-axis, illustrated for point 6, Fig. 6.14b.

## 6.8 Discussion

The results of the present chapter are illustrated in Figs. 6.10,b and 6.11,b. They show how the dispersion curves for electron states in a quantum wire with rigid walls placed in magnetic field normal to the walls evolves with increasing the spin-orbit strength quantified by the dimensionless parameter, $\nu$. From these figures, we can draw qualitative conclusions about the shape of the absorption spectrum in a wire. This spectrum should be contrasted to the spectrum in the absence of magnetic field and SO coupling.

First, note that, in the wire geometry, absorption takes place only for an ac electric field polarized *normally* to the boundaries. This is because the momentum, $P$, along the wire is conserved, so that, for an electric field along the wire, the absorption matrix element is zero due to orthogonality of the size-quantization wave functions. In the absence of magnetic field and SO coupling, the absorption spectrum of the wire represents a system of *discrete* peaks (with zero width). This is because all dispersion curves of subbands are parallel to each other. Moreover, in the presence of a Zeeman field, this structure will not change, since all subbands will split by the same amount and remain parallel. Concerning the relative oscillator strengths of different peaks, for two subbands, $m$ and $n$, it is determined by $|\int dy \Psi_n(y) y \Psi_m(y)|^2$. This quantity is nonzero for $|m-n| = 1$ in the case of parabolic confinement, suggesting that there is only a *single* absorption line. For the case of rigid walls, when $\Psi_n(y) \propto \cos\left[\frac{(2n-1)\pi y}{a}\right]$ and $\Psi_n(y) \propto \sin\left[\frac{2m\pi y}{a}\right]$, the intensity of the corresponding line is given by

$$I_{n,m} \propto \frac{m^2(2n+1)^2}{[4m^2-(2n+1)^2]^4}. \tag{6.78}$$

Although there is no strict selection rule, the denominator contains a factor $[2(m-n)+1]^4$, suggesting that still only the lines corresponding to neighboring subbands will contribute to the spectrum.

Let us now gradually switch on the SO coupling. Weak SO-coupling limit is illustrated in Fig. 6.10. We see that Zeeman-split subbands are still essentially parallel to each other except for the vicinities of the "compensation" points where the dispersion curves cross each other. These crossings, which occur at dimensionless longitudinal momentum $P = 1$, will manifest themselves in the absorption spectrum near certain electron densities or, equivalently, near certain positions of the Fermi level, $E_F$. For general values of $E_F$, the new feature in the absorption spectrum is appearance of an additional peak at frequency $\omega = \Delta_Z$, which corresponds to EDSR. Finite SO coupling enables the absorption between the Zeeman-split branches. The important question is how the magnitude of the EDSR peak scales with $\nu$. In Section 2.3.1 (see Eq. (6.30)), we derived the expression for matrix element $M$, which at small $\nu$ behaves as $\nu^2$. Consequently, the peak intensity is proportional to $\nu^4$. This should be contrasted to the EDSR intensity in 2D, which was shown to be quadratic in SO-coupling strength. The origin of the difference is that, while $\nu^2$ is the degree of *spin* mixing of the Zeeman-split branches, the *coordinate* parts do not change in the lowest order; it takes another $\nu^2$ to make the dipole matrix element nonzero.

The fact that size-quantization wavefunctions in Fig. 6.10 are essentially the same as in a zero magnetic field can be understood if we recall the definitions of parameter, $\nu$, and dimensionless width, $a$. As follows from Eqs. (6.4), (6.53), the product $\nu a^2$ can be rewritten as

$$\nu a^2 = \frac{\Delta_Z}{(\hbar^2/md^2)}, \tag{6.79}$$

i.e., it does not contain the SO-coupling strength and represents the ratio of Zeeman and size-quantization energies. For curves in Fig. 6.10, the product $\nu a^2$ does not exceed 0.1.

Strictly speaking, the low-frequency absorption takes place when the Fermi momentum is at $P = 1$. However, as it is seen in Fig. 6.10, the dispersion curves practically touch each other in a broad range of momenta around $P = 1$. Within this range, the theory Eq. (6.39) and (6.42) applies.

In Fig. 6.9, the strength of SO coupling is five times bigger than in Fig. 6.10. While the dispersion curves do not change qualitatively between these two cases, the wavefunctions

do. For the lowest subband, the part of the dispersion curve $P < 0.5$ falls between two dashed lines. This suggests that the corresponding wavefunction is a combination of two cosines and two exponents. Vertical arrows in Fig. 6.9 indicate the domains of the momenta responsible for absorption. We expect that, for domain of negative $P$, the difference in wavefunctions between lower and upper states will result in enhancement of the absorption magnitude.

Figs. 6.11, 6.12 represent the regime of strong SO coupling. They both correspond to $\nu = 1.5$ but to different energy domains. It can be seen that the dispersion curves can no longer be grouped in pairs separated by Zeeman splitting. In fact, under the condition $\nu > 1$, the Zeeman energy is less important than the SO coupling. We also see that most of the curves in Fig. 6.11 fall between the two dashed lines, so that both the initial and final states between which the absorption takes place are represented by the wavefunctions consisting of two cosines and two exponents. The width of each absorption line can be determined as a difference in heights of the vertical lines corresponding to the boundaries of domains where initial state is occupied, while the final state is empty. We see from Fig. 6.11 that the lines corresponding to negative $P$ remain narrow. However, the magnitude of absorption within the corresponding lines is expected to be much larger than in Figs. 6.10, 6.9. Qualitatively, this is because Figs. 6.10, 6.9, correspond to EDSR in presence of size quantization, while Figs. 6.11, 6.12 correspond to the chiral resonance in the presence of size quantization. We have seen in the previous chapter that absorption under the conditions of chiral resonance does not contain small factors.

Higher subbands presented in Fig. 6.12 are shown in blue and lie entirely outside the domains defined by two dashed lines. They are weakly split and almost parabolic, suggesting that their dispersion is not sensitive to the SO coupling, except for the domain near $P = 1$. This could be expected on general grounds for this high-energy subbands. Indeed, the kinetic energy grows with momentum quadratically, while the SO coupling only linearly.

As a final remark, the spin projection operators show sensitivity near the compensation point. First note that away from the point $P = 1$, the spin projection is mostly along $\sigma_y$ and closely follows the probability density $\mathcal{P}$. See Fig. 6.13. This effect was seen by Ref. [12], where the dispersion curves and spin textures were calculated by solving the Schrödinger equation numerically and for parabolic confinement. For parabolic confinement, the two dispersion curves "meet" near $kl_0 = 0$, where $k$ is the wave vector and $l_0$ is the characteristic confinement length, instead of $P = 1$. The Ref. [12] focuses on

spin projection operators and conductance, and offers an analysis of absorption with no emphasis on the "meeting" point between the two curves. In our analysis, we found that near the "meeting" point, the spin projection is mostly along the direction of transport, $\sigma_x$. It can be viewed that the spin projection operators can be viewed as a signature of the SO coupling strength, since without SO coupling, the spin projection operators would not show anything.

## 6.9 Appendix

### 6.9.1 Derivation of the constants $\lambda_1$, $\lambda_2$, $\lambda_3$, $\lambda_4$

Recall that energy dispersion, Eq. (6.67), introduced in Section 6.5, was derived using the boundary conditions. We will derive the constants $\lambda_1$, $\lambda_2$, $\lambda_3$ in terms of $\lambda_4$ from the equations described in Section 6.5. Then $\lambda_4$ can be found by normalization of the wavefunction. Immediately from Eq. (6.64) we find $\lambda_2$, which reads

$$\lambda_2 = -\lambda_4 \left(\frac{g_3 - g_4}{g_2 - g_3}\right) \frac{\sin(Q_2 + Q_1)a}{\sin(Q_2 - Q_1)a}. \tag{6.80}$$

Using the definition of $\lambda_2$, Eq. (6.80) and the energy dispersion, Eq. (6.66), we add Eqs. (6.60), (6.62). Solving for $\lambda_1$ gives

$$\lambda_1 = \lambda_4 \left(\frac{g_3 - g_4}{g_1 - g_3}\right) \frac{\sin(2Q_2 a)}{\sin(Q_2 - Q_1)a}. \tag{6.81}$$

Similarly, we add Eqs. (6.61), (6.63), and solve for $\lambda_3$ using Eqs. (6.80), (6.66). Then the resulting $\lambda_3$ is

$$\lambda_3 = -\lambda_4 \left(\frac{g_1 - g_4}{g_1 - g_3}\right) \frac{\sin(2Q_2 a)}{\sin(Q_2 + Q_1)a}. \tag{6.82}$$

The final constant $\lambda_4$ is simply,

$$\lambda_4 = \Big( \int_{-a}^{+a} dy \Psi^* \Psi \Big)^{-1/2}. \tag{6.83}$$

## 6.10 References


[1] A. V. Moroz and C. H. W. Barnes, Phys. Rev. B **60**, 14272 (1999).

[2] F. Mireles and G. Kirczenow, Phys. Rev. B **64**, 024426 (2001).

[3] M. Governale and U. Zülicke, Phys. Rev. B **66**, 073311 (2002).

[4] S. Debald and B. Kramer, Phys. Rev. B **71**, 115322 (2005).

[5] M. Lee and C. Bruder, Phys. Rev. B **72**, 045353 (2005).

[6] S. Zhang, R. Liang, E. Zhang, L. Zhang, and Y. Liu, Phys. Rev. B **73**, 155316 (2006).

[7] Ll. Serra, D. Sánchez, and R. López, Phys. Rev. B **76**, 045339 (2007).

[8] G. Gumbs, A. Balassis, and D. Huang, J. Appl. Phys. **108**, 093704 (2010).

[9] S. I. Erlingsson, J. C. Egues, and D. Loss, Phys. Rev. B **82**, 155456 (2010).

[10] E. Nakhmedov, O. Alekperov, and R. Oppermann, Phys. Rev. B **83**, 153416 (2011).

[11] Y. V. Pershin, J. A. Nesteroff, and V. Privman, Phys. Rev. B **69**, 121306(R) (2004).

[12] Ll. Serra, D. Sánchez, and R. López, Phys. Rev. B **72**, 235309 (2005).

[13] A. Fedorov, Y. V. Pershin, and C. Piermarocchi, Phys. Rev. B **72**, 245327 (2005).

[14] F. Malet, M. Pi, M. Barranco, L. Serra, and E. Lipparini, Phys. Rev. B **76**, 115306 (2007).

[15] T.-Y. Zhang , W. Zhao, and X.-M. Liu, Journal of Physics Condensed Matter **21**, 335501 (2009).

[16] C. Quay, T. Hughes, J. Sulpizio, L. Pfeiffer, K. Baldwin, K. West, D. Goldhaber-Gordon, and R. de Picciotto, Nat. Phys. **6**, 336 (2010).

[17] S. Chesi, G. F. Giuliani, L. P. Rokhinson, L. N. Pfeiffer, and K. W. West, Phys. Rev. Lett. **106**, 236601 (2011).

[18] M. I. Dyakonov and V. I. Perel, Sov. Phys. JETP Lett. **13**, 467 (1971).

[19] J. Wunderlich, B. Kaestner, J. Sinova, and T. Jungwirth, Phys. Rev. Lett. **94**, 047204 (2005).

[20] Y. K. Kato, R. C. Myers, A. C. Gossard, and D. D. Awschalom, Science **306**, 1910 (2004).

[21] R. M. Lutchyn, J. D. Sau, and S. Das Sarma, Phys. Rev. Lett. **105**, 077001 (2010).

[22] Y. Oreg, G. Refael, and F. von Oppen, Phys. Rev. Lett. **105**, 177002 (2010).

[23] Ar. Abanov, V. L. Pokrovsky, W. M. Saslow, P. Zhou, Phys. Rev. B **85**, 085311 (2012).

[24] T. V. Shahbazyan and M. E. Raikh, Phys. Rev. Lett. **73**, 1408 (1994).

[25] I. L. Aleiner and V. I. Fal'ko, Phys. Rev. Lett. **87**, 256801 (2001).

[26] E. I. Rashba and Al. L. Efros, Phys. Rev. Lett. **91**, 126405 (2003).

[27] E. McCann and V. I. Fal'ko, Phys. Rev. Lett. **96**, 086805 (2006).
Appl. Phys. A: Mater. Sci. Process. **87**, 577 (2007).

[28] Yu. A. Bychkov and E. I. Rashba, J. Phys. C **17**, 6039 (1984).

[29] A. K. Farid and E. G. Mishchenko, Phys. Rev. Lett. **97**, 096604 (2006).